GROWTH AND PATTERNING OF NANOSTRUCTURES THROUGH IRREVERSIBLE LIQUID DRYING, SELF-ASSEMBLY, AND CRYSTALLIZATION

WU JIHONG

(M. Sc., Xiamen University, China)

A THESIS SUBMITTED

FOR THE DEGREE OF DOCTOR OF PHILOSOPHY IN SCIENCE

DEPARTMENT OF CHEMISTRY

NATIONAL UNIVERSITY OF SINGAPORE

2010

GROWTH AND PATTERNING OF NANOSTRUCTURES THROUGH IRREVERSIBLE LIQUID DRYING, SELF-ASSEMBLY, AND CRYSTALLIZATION

WU JIHONG

NATIONAL UNIVERSITY OF SINGAPORE

2010

ACKNOWLEDGEMENTS

I would like to express my sincere gratitude to my supervisor, Professor Xu Guo Qin. His understanding, encouragement and guidance are of great value for my research.

I would like to thank my co-supervisor, Professor Ang Siau Gek. She provided invaluable support and important advices throughout this work. I am also grateful to Dr Xu Qing Hua for his support and help.

I'd like to thank the many research staff and students I worked with in both Xu Guo Qin's and Ang Siau Gek's groups for their continued help in daily laboratory life.

My forever appreciation goes to my family members for their support and encouragement.

Last but not least, I must acknowledge the National University of Singapore for the graduate research scholarship.

TABLE OF CONTENTS

ABSTRACT

Fast-drying has been developed as a method for the fabrication of large-scale nanopatterns on various solid surfaces from thin solution layers. This method has been applied to the surface patterning of four different materials, ranging from inorganic salts (i.e., NaCl and $Zn(NO_3)_2.6H_2O$) to organic compounds (i.e., organosilane and anthracene). Emphases were focused on exploring the mechanisms involved in the surface patterning, including heterogeneous epitaxial crystallization, self-epitaxial nucleation (SEN), diffusion-limited aggregation (DLA), and water-adsorption induced morphology transition, self-assembly, fingering instability, repeating slipping-and-sticking motions of the contact line during irreversible drying of thin solution layer. Specifically, the major research projects presented in this thesis include (1) oriented NaCl nanocrystals grown on mica from thin solution layers: morphology transition and self-assembly; (2) interconnected networks of $Zn(NO_3)_2.6(H_2O)$ nanotubes and its solid-phase transformation into porous zinc oxide architectures; (3) macroscopic concentric ring arrays of radially-oriented anthracene wires based on irreversible liquid drying and molecular self-assembly; and (4) macroscopic surface architectures of self-assembled (3-aminopropyl)triethoxysilane (APTES) and non-equilibrium crystalline patterns of APTES oligomers.

NaCl nanocrystals with uniform orientation, including triangular pyramids, cubes and long nanowires, were epitaxially grown on mica from thin solution

layers under a wide variety of ambient humidity. The morphology transition of the NaCl epitaxial nanocrystals can be attributed to the water adsorption at the surface of the growing NaCl nanocrystals. The oriented NaCl nanocrystals can spontaneously organize into highly ordered arrays with exceptionally large spatial scales (up to ~10 mm^2).

We investigated the one-step synthesis of highly oriented, interconnected $Zn(NO_3)_2.6H_2O$ nanotubes on mica and subsequent solid-phase thermal decomposition into porous ZnO architectures. The uniform orientation of the $Zn(NO_3)_2.6H_2O$ nanotubes was governed by an epitaxial growth mechanism. The formation of rectangular nanotubes was originated from the folding-up of large nanotubes. Porous ZnO nanostructures were obtained through the thermal decomposition of $Zn(NO_3)_2.6H_2O$ nanotubes. The porous ZnO prepared at different temperatures exhibited different photoluminescence (PL) properties.

Macroscopic concentric ring arrays of radially-oriented anthracene wires were successfully grown on various substrates on the basis of drying-assisted self-assembly. The formation of concentric ring arrays is possibly due to the repeating slipping-and-sticking motions of the contact line. The growth of one-dimensional (1D) anthracene wires can be attributed to both π-π interaction between anthracene molecules and fingering instability during the irreversible drying of the thin solution layer. The radial orientation of anthracene wires was directly driven by the outward capillary flow involved in the evaporating thin solution layer. The growth of anthracene wires can be attributed to both the

capillary flow and the Marangoni convectional flow.

We studied the self-assembly behavior of APTES on mica from thin and/or thin aqueous solution layers. Under fast-drying conditions, the APTES self-assembled molecular layers were decorated with macroscopic concentric ring arrays, which can be attributed to the repeating slipping-and-sticking motion of the contact line during the irreversible drying of thin solution layers. The structures of the self-assembled molecular layers were directly related to the molecular form of APTES in the aqueous solution at different concentrations.

We also explored the crystallization behaviors of APTES oligomers under non-equilibrium conditions from thin aqueous solution layers through a similar fast-drying method. Various crystalline patterns, including zigzag fractal crystals, parallel aggregations and tree-like dendritic aggregations, were obtained under different driving forces and supersaturations. The mechanisms involved in the non-equilibrium pattern formation were discussed based on the crystallization theories of self-epitaxial nucleation (SEN) and diffusion-limited aggregation (DLA).

LIST OF PUBLICATIONS

- Interconnected Networks of $Zn(NO_3)_2$ 6(H_2O) Nanotubes and Its Solid-Phase Transformation into Porous Zinc Oxide Architectures
  Ji Hong Wu, Binni Varghese, Xue Dong Zhou, Si Ying Teo, Chorng Haur Sow, Siau Gek Ang, and Guo Qin Xu
  Chemistry of Materials **2010**, *22*, 1533.

- Atomic Force Microscopy Study of Self-Assembled Sodium Chloride Nanocrystallites and Their Morphology Transitions
  Ji Hong Wu, Siau Gek Ang, and Guo Qin Xu
  J. Chem. Phys. C **2008**, *112*, 7605.

- Macroscopic Concentric Ring Arrays of Radially-Oriented Anthracene Wires Based on Irreversible Liquid Drying and Molecular Self-Assembly
  Manuscript in preparation

- Macroscopic Concentric Ring Arrays of Radially-Oriented Neocuproine Wires Based on Irreversible Liquid Drying and Molecular Self-Assembly
  Manuscript in preparation

- Nanoscopic Surface Architectures Based on Irreversible Drying and Molecular Self-Assembly of (3-Aminopropyl)triethoxysilane (APTES)
  Manuscript in preparation

- Non-equilibrium Crystalline Patterns of (3-Aminopropyl)triethoxysilane (APTES) Oligomers
  Manuscript in preparation

- Zinc Oxide Microscopic Flowers: Growth Mechanism Discussion
  Manuscript in preparation

- Oriented Alkali Halide Nanocrystals Grown from Ultrathin Solution Layers
  Manuscript in preparation

LIST OF TABLES

LIST OF FIGURES

Chapter 1

Introduction to Construction of Oriented Nanostructures

1.1 Introduction

New phenomena and properties associated with nanostructures have received steadily growing attention. The best established examples include size-dependent excitation and/or emission [1-4], quantized (or ballistic) conductance [5-6], and metal-insulator transition [7]. In general, nanostructures can be realized simply by size reduction of the larger-sized substances into the 1-100 nm regimes through 'top-down' approaches. However, most of the 'top-down' approaches involve complicated processes and require rigorous manufacturing conditions. An alternative, yet versatile, strategy towards nanostructures is to organize smaller elements (molecules, atoms, and/or ions) in a well-controlled manner through 'bottom-up' approaches. Significant progresses have been made in the synthesis of nanostructures over a wide range of materials with excellent control over the sizes and shapes by adopting various "bottom-up" approaches [8-13]. Taking ZnO as an example, so far, a variety of ZnO nanostructures have been reported, including but not limited to nanoparticles [14], tetrapods [15-17], nanorods [18-20], nanowires [21, 22], nanobelts [23, 24], nanotubes [25-28], core-shell structures [29, 30], and other complex hierarchical structures [31, 32].

Assemblies of ordered nanostructures open up fundamental scientific opportunities to explore the organization behaviors at molecular level (self- and/or

imposed molecular organization) and the influence of size and dimensionality with respect to their collective optical, magnetic, and electronic properties. The properties possessed by the elementary structural units can be largely enhanced in the assembled regimes. Besides, it is also possible to expand their properties by organizing large number of one-dimensional (1D) nanostructures into complex hierarchical architectures, which otherwise do not exist in the elementary structural units [34, 35]. For example, assemblies of oriented 1D nanowires and nanorods may produce unusual light scattering and polarization effects, especially for II-VI compound semiconductors with a large polarity and band gap energy in the visible range. Besides, it is much easier to deal with their assemblies because of the relatively larger dimensions, as compared to the extremely small single nanostructures.

In the following, theories involved in the synthesis of nanostructures are briefly introduced. Emphasis is laid on the introduction of crystallization theories as well as the theories of irreversible liquid evaporation on solid surfaces. An overview of the research activities on synthesis of two-dimensional (2D) or three-dimensional (3D) assemblies of oriented nanostructures is also presented. Various established synthesis methods are described. The comparative advantages and drawbacks of each synthetic approach are briefly discussed. This is followed by the outline of the scope and objectives of the works presented in this thesis.

1.2 Theories

1.2.1 Crystallization

The essence of nanostructure formation through the bottom-up approaches is crystallization [36]. Crystallization involves two major steps: primary nucleation and subsequent crystal growth. Nucleation is the very initial step for the formation of a 'new' phase within a homogeneous 'old' phase. In general, the emergence of gaseous bubbles, glassy and/or crystalline regimes in a liquid phase (solutions or melts), and the formation of liquid droplets in a vapor phase are characterized by nucleation. The research in this thesis mainly involves the creation of crystalline solids from a solution phase, where the newly formed phase is termed as nucleus. The driving force for crystallization is supersaturation, which refers to the fact that the amount of solute in a solution exceeds its solubility under equilibrium condition. In a supersaturated solution, nucleation can begin spontaneously (homogeneous nucleation), or be triggered by an existing foreign material such as a dust particle (heterogeneous nucleation).

I. Free Energy Change of Nucleation

Assuming that the nuclei are spheres with a radius of r, the overall free energy change (ΔG) involved in the nucleation can be expressed as follows [37]

$$\Delta G = \frac{4}{3}\pi r^3 \Delta G_v + 4\pi r^2 \sigma$$

Here the first term refers to the energy gain in the creation of the new phase (i.e., nucleus) and the second term indicates the energy cost in the formation of the new

nucleus-solution interface. ΔG_v is the change of free energy per unit volume (erg/cm^3), σ is the surface tension of the newly generated interface per unit area (erg/cm^2). Nucleation is favored only when ΔG is negative. Figure 1.1 gives the free energy change (ΔG) in nucleation as a function of the nucleus radius. An extremely small nucleus is not stable because of the large fraction of their active surface atoms. It costs free energy to add structural monomers (molecules, ions, or atoms) into this small nucleus until its radius reaches the critical value (r = r*). The critical radius r* is given where $\Delta G = \frac{dG}{dt} = 0$, i.e., the maximum point in the total free energy

$$r^* = -\frac{2\sigma}{G_v} \quad \text{and} \quad \Delta G^* = \frac{16\pi\sigma^3}{3\,(G_v)^2}$$

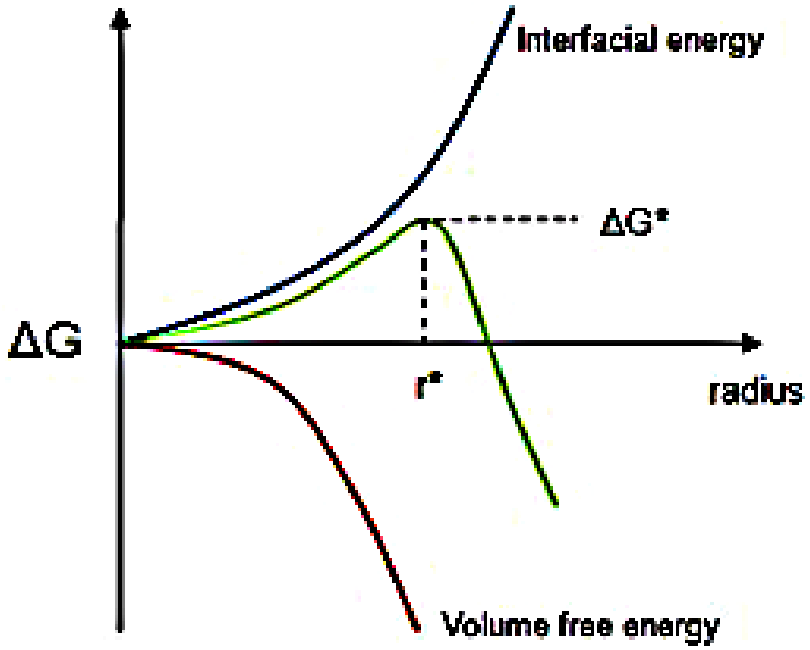

Figure 1.1 Schematic illustration of free energy change (ΔG) involved in nucleation as a function of the nuclear radius.

In practice, heterogeneous nucleation occurs more often than homogeneous nucleation. The existence of foreign materials provides preferential sites for nucleation, thus decreasing the free energy barrier for heterogeneous nucleation.

The heterogeneous nucleation theory creates an extra parameter, f(θ), to make the theoretical calculation fit with the experimental data [38] :

$$\Delta G_{heterogeneous} = \Delta G_{homogeneous} * f(\theta)$$

$$f(\theta) = \frac{1}{2} - \frac{3}{4}\cos\theta + \frac{1}{4}\cos^3\theta$$

Where θ is the contact angle of the liquid phase against the foreign material surface.

II. Nucleation Rate

The nucleation rate I, defined as the number of nuclei formed per unit volume and unit time, in a homogeneous nucleation can be expressed as follows [39]

$$I = A \exp\left[\frac{-16\pi\sigma^3 V_s^2}{3k_B{}^3T^3} (\ln S)^2\right]$$

Where A is a constant which has been estimated to be in the order of 10^{23} to $10^{32.5}$ [40, 41], V_s is the molecular volume of the crystal (cm^3/molecule; molar volume/Avogadro's number), k_B is the Boltzmann constant, T is the absolute temperature (K), and S is the supersaturation ratio which is defined as

$$S = \frac{\text{actual concentration}}{\text{equilibrium concentration}} = \frac{c}{c_s} \quad (c > c_s)$$

III. Dynamic Mass Balance of Nucleation

Figure 1.2 shows the supersaturation ratio (S) and the crystal number (Z) during crystallization as a function of time [42]. Initially, the system is at equilibrium. At the starting point of the crystallization, S increases rapidly and exceeds the critical value S_c for spontaneous nucleation at the time t_l. As soon as

nuclei are formed, their growth will compete with nucleation and S will increase at a lower rate until the maximum point is reached. Then, S will begin to decrease and drop below S_c at the time t_2. The time span (t_2-t_l), where S is greater than S_c, is usually referred to as the 'nucleation region'.

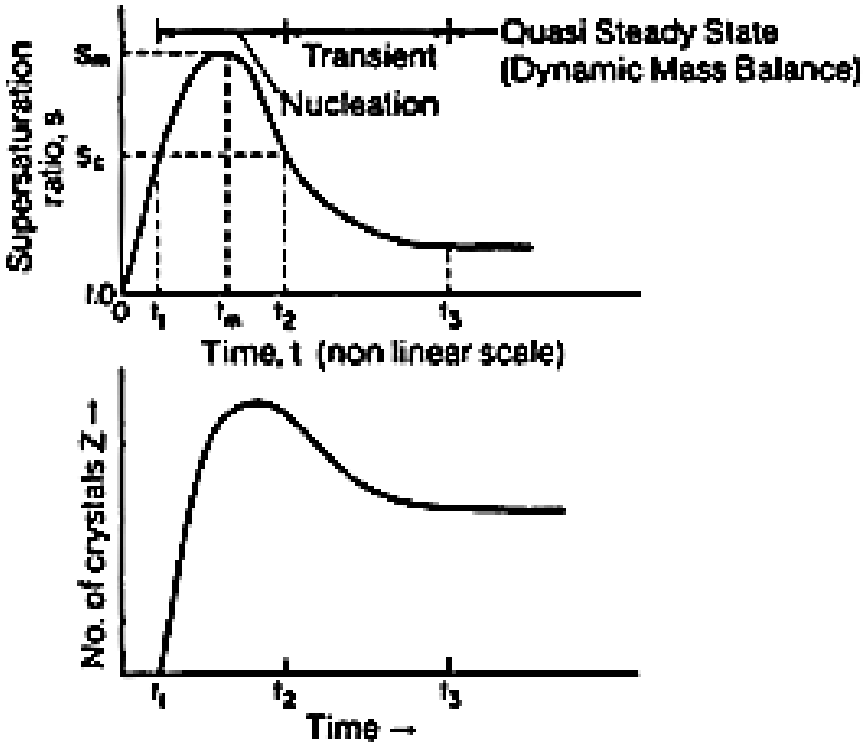

Figure 1.2 Supersaturation profile and crystal number as a function of crystallization time. Both axes are relative and nonlinear. Reproduced from [42].

IV. Classic Theory of Crystal Growth

The elementary geometric objects on a 2D crystal surface include terraces (T), steps (S), and kinks (K). Shown in Figure 1.3 is the TSK model of a 2D crystal surface. The foundation of crystal growth theory was laid out in the paper of Burton, Cabrera and Frank (BCF) [43]. According to the BCF model, the crystal grows as the consequence of the 2D extension of the steps. At the atomic scale, the growth of a crystal can be described as adding structural monomers (molecules,

atoms, and/or ions) into the surface lattice of the growing crystals [44]. Specifically, the monomers in solution diffuse toward the growing crystal surfaces (the step of bulk diffusion) and are adsorbed onto the crystal surface at random locations (the step of surface adsorption). The adsorbed monomers are mobile and can diffuse along the crystal surface until they are incorporated into the underlying surface lattice (the step of surface incorporation).

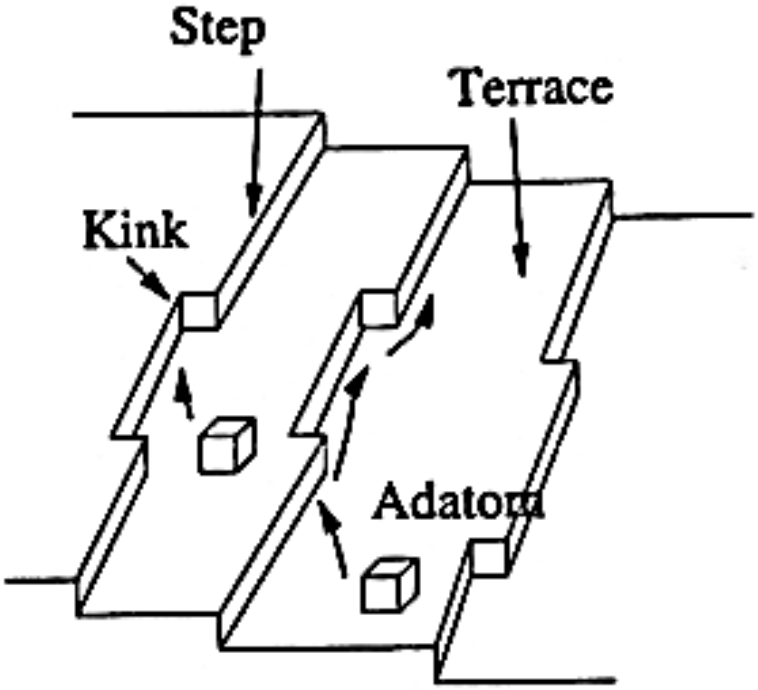

Figure 1.3 TSK model of a 2D crystal surface.

Bauer predicted [45] that depending on surface energies of the substrate (γ_s) and the epitaxial film (γ_f), and the interfacial energy (γ_{in}), the epitaxial growth of crystalline film on a crystalline substrate follows one of the three modes (Figure 1.4), i.e., Frank-van der Merwe (FM) mode (monolayer-by-monolayer growth), Vomer-Weber (VW) mode (3D island growth), and Stranski-Krastanov (SK) mode (monolayer-by-monolayer plus 3D island growth). The overall surface energy

change in the epitaxial crystallization can be expressed as:

$$\Delta\gamma_n = \gamma_{fn} + \gamma_{in} - \gamma_s \quad \text{(n is the thickness of the epitaxial film)}$$

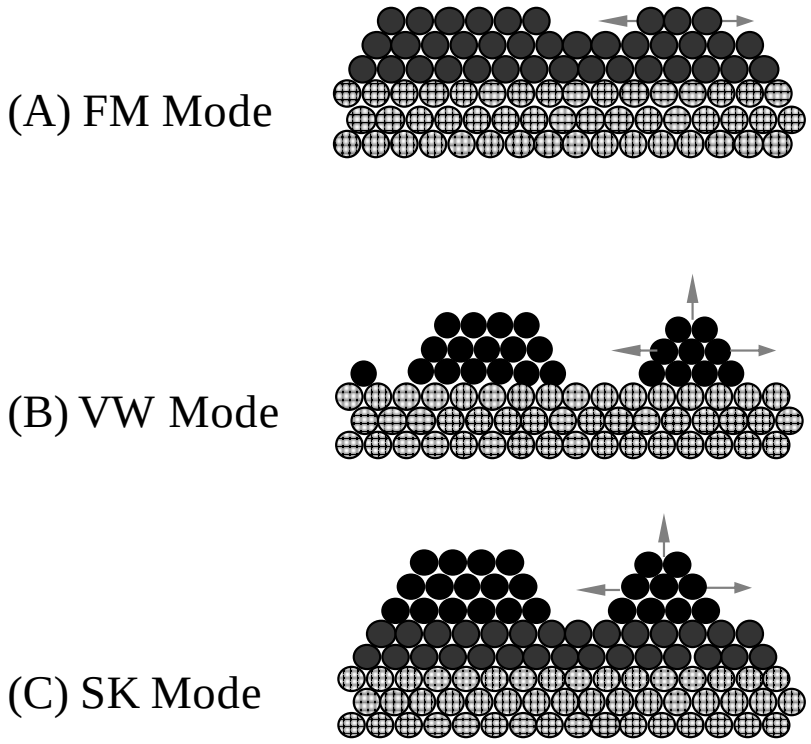

Figure 1.4 Schematic models illustrating different growth modes for the epitaxial deposition. (A) FM mode (monolayer-by-monolayer growth), (B) VW mode (3D island growth), and SK mode (monolayer-by-monolayer plus 3D island growth). The arrows indicate the growth directions.

The interfacial energy (γ_{in}) is a reflection of the strain energy in the epitaxial film that is induced by the lattice mismatch between the epitaxial film and the substrate. The strain energy depends on the thickness of epitaxial film as well as the atomic bonding at the interface. γ_{fn} deviates somewhat from the γ_f due to the n-dependent stain energy. Monolayer-by-monolayer growth (FM mode) occurs only when $\Delta\gamma_n < 0$. Such situation is rigorously fulfilled only in the homoepitaxy (i.e., A grows on A) where $\gamma_f = \gamma_s$, and $\gamma_{in} = 0$. In some heteroepitaxy (i.e., B grows on A) with zero lattice mismatch, FM mode is also possible within the first

few monolayers if the interface energy γ_{in} rapidly approaches to zero because of the specific chemical interaction between the epitaxial film and the substrate. After the film thickness reaches a critical value n*, the FM mode will not be fulfilled anymore because of the increase of γ_{in} along with the film thickness. The monolayer-by-monolayer growth (FM mode) then switches to the 3D-island growth (SW mode). If the FM condition is not fulfilled from the very beginning (n = 1), 3D islands form immediately on the substrate (VW mode).

V. Kinetic Size Control

Classic crystallization theories deal with the crystallization processes occurring at equilibrium conditions. Crystallization involved in the nanostructure synthesis, however, is more often a non-equilibrium process. Although impressive progresses have been made towards the nanostructure synthesis over a wide range of materials with well-defined sizes and shapes, little is quantitatively known about this process from a microscope view. There are no general means to achieve precise control over the nanostructure growth.

In order to obtain nanostructures with uniform size distribution, it is desirable to separate the nucleation from the crystal growth. Ideally, the rapid and intense nucleation only occurs within a very short time span. The monomer concentration in the solution drops below the nucleation threshold immediately after the nucleation; the subsequent crystal growth proceeds with no further nucleation occurring. Such a rapid nucleation is termed as the instantaneous nucleation [46, 47]

and favors for a uniform size distribution in the final product. However, the progressive nucleation is more often observed in practice, in which there is some overlap in the time scale of nucleation and crystal growth. After the primary nucleation, the subsequent crystal growth associated with a low monomer concentration is accompanied by the secondary nucleation, not favorable for a uniform size distribution of the final product. In order to obtain a narrow size distribution, Alivisatos [48] proposed a smart 'size-distribution focusing' strategy, based on Reiss's prediction [49]. Reiss anticipated that small crystals grow more rapidly than the large ones as long as the monomer concentration is sufficiently high. Figure 1.5 schematically illustrates the growth rate of nanocrystals as a function of their sizes at low and high monomer concentrations. Each monomer concentration gives a corresponding critical size (r*). At high monomer concentration, the critical size r* is small enough that almost all of the nanocrystals fall in the growing region (the right-hand side of that curve). A narrow size distribution is thus achieved as the small nanocrystals grow faster than the large ones. When the monomer concentration is below the critical threshold, a large amount of nanocrystals falls in the depleting region (the left-hand side of that curve). Typical Ostwald ripening occurs, in which the larger crystals grow at the sacrifice of the smaller ones [50], resulting in a broad size distribution. A high monomer concentration can be achieved by arresting the crystallization while it is still in the focusing regime with a secondary injection of precursor [51]. Immediately after injection, the critical size r* shifts to the smaller regime due to

the increase of monomer concentration. Most of the nanocrystals can fall in the growing region as long as this shift is large enough. In the growing region, the smaller nanocrystals grow more rapidly than the larger ones. As a result, the size distribution will spontaneously be narrowed down or be 'focused'.

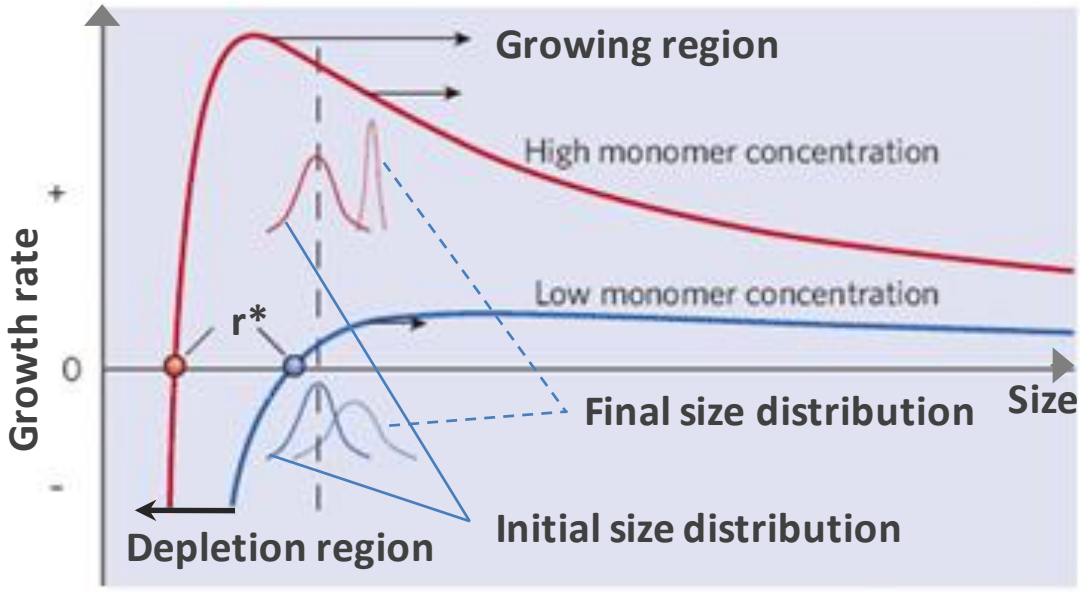

Figure 1.5 Schematic illustration of size-distribution focusing during nanocrystal growth. The size distribution of nanocrystals can either become narrower (be focused) or wider (be defocused) during the growth, depending on the monomer concentration. A critical size exists at any given monomer concentration. At a high monomer concentration, the critical size is at a small level so that all the nanocrystals are in the growing regime. Consequently, the size distribution can be focused down to the nearly mono-disperse level as the smaller nanocrystals grow faster than the larger ones. If the monomer concentration is below a critical threshold, the critical size is at a large level so that most of the nanocrystals are in the depletion regime. As a result, the size distribution is broadened (or defocused) because the smaller nanocrystals are depleted as the larger ones grow. The preparation of nearly mono-dispersed nanocrystals can be achieved by arresting the reaction while it is still in the focusing regime, with a large concentration of monomer still present. Reproduced from [48].

VI. Kinetic Control of Crystal Morphology

The crystal structure (microscopic conception) is defined at the nucleation stage when the atoms are arranged in a defined and periodic manner in the nuclei. The crystal morphology (macroscopic conception), however, largely depends on the kinetic of crystal growth.

The growth rate of a crystal surface depends exponentially on the surface energy. The high-energy surfaces grow more quickly than the low-energy ones and will eventually disappear during crystal growth. It is well-known that the equilibrium shape of a crystal is determined by Wulff theorem [52], namely, the crystal is bound with low-energy facets so that the total surface energy is minimized. Many inorganic materials with highly anisotropic crystal structures, such as selenium [53] and tellurium [54], can naturally grow into 1D nanostrucutres. For isotropic inorganic crystals, their low-energy surfaces are relatively close in energy [48]. Under thermodynamic equilibrium conditions, they tend to grow into nearly 'round' shapes to minimizes the total surface energy. In order to synthesize high-aspect-ratio nanomaterials with isotropic crystal structure, one has to seek help from other strategies. So far, the template-assisted synthesis has presented many good examples [55-58]. Besides, a large number of approaches have also been developed for the kinetic control over the nanomaterial growth towards 1D morphology at non-equilibrium conditions. Some excellent examples can be found in the vapor-liquid-solid (VLS) synthesis [59-62] and its analogy, solution-liquid-solid (SLS) synthesis [63-65]. It is generally accepted that the

morphology of nanomaterials can be tuned by controlling the degree of supersaturation. There is strong evidence, as have been documented extensively in the literature [66, 67], that a low supersaturation favors for the growth of 1D structures whereas a high supersaturation supports the formation of low-aspect-ratio structures such as nanoparticles. In principle, it is possible to synthesize 1D nanostructures of any kind of solid material by controlling the supersaturation at a relatively low level. The kinetic morphology control can also be achieved by employing various organic capping reagents. The selective adsorption of organic molecules onto a particular crystal facet can effectively lower its free surface energy and thus slow down its growth rate. The capping-reagent strategy has been widely employed in the synthesis of 1D colloidal nanostructures [13, 68-70]. It was also reported that linear nanostructures can be created through an oriented attachment of 'short' isotropic monomers [71-76], in which a possible coalescence of the isotropic monomers may be involved to eliminate the high-energy facets [48].

1.2.2 Liquid Evaporation on Solid Surfaces

I. Contact Line Pinning and Depinning

When a pure liquid droplet placed on a smooth solid surface, the equilibrium shape of the liquid droplet is dominated by the wettability of the solid surface. The wettability is defined as the ability of a solid surface to maintain contact with a liquid droplet, which is determined by a balance between the adhesive and cohesive

forces. The liquid droplet tends to spread across the solid surface under action of the adhesive force and to ball up under the action of the cohesive force. The wettability is characterized by the contact angle, i.e., the angle between the planes tangent to the solid-liquid and liquid-vapor interfaces where these two interfaces intersect (Figure 1.6). This intersection is the contact line. For idealized situations, thermodynamic analyses [78] predicted that each material system should exhibit a unique contact angle given by Young's equation [77]

$$\gamma_{SG} = \gamma_{SL} + \gamma_{LG} \cos\theta_c$$

Where γ_{SG}, γ_{SL}, and γ_{LG} refer to the solid-gas, solid-liquid, and liquid-gas interfacial energies, respectively. θ_c is the contact angle. The liquid-vapor interface meets a liquid-philic surface with a contact angle less than 90 º(Figure 1.6A); on the contrary, the contact angle is larger than 90 ºon a liquid-phobic surface (Figure 1.6B).

(A) Liquid-philic Surface ($\theta_c < 90$ ºˆ)

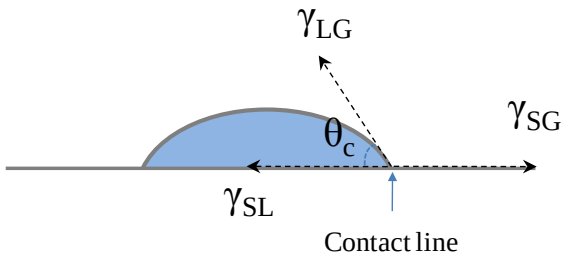

(B) Liquid-phobic Surface ($\theta_c > 90$ ºˆ)

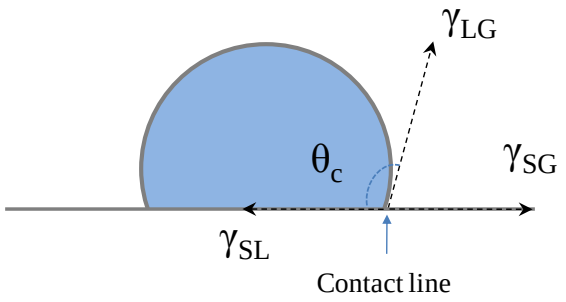

Figure 1.6 Contact angle of a liquid droplet on a rigid solid surface: (A) on the liquid-philic surface, $\theta_c < 90$ º; and (B) on the liquid-phobic surface, $\theta_c > 90$ º.

When a pure droplet was placed on the smooth mica surface [79], the water droplet initially grew until reaching a maximum radius because of the hydroplilicity of the mica surface and the gravitational force, and thereafter it shrank continuously to zero size upon evaporation. When the pure water droplet was replaced by a water droplet with a colloidal suspension of polystyrene (PS) microspheres, the droplet grew quickly to its largest size, much like the pure water droplet. Unlike the pure water droplet, however, it remained at its maximum size for a short duration. In other words, the contact line was pinned against the mica surface and prevented from backward retracting. Nadkarni and Garoff [80] examined carefully the microscopic pinning of the contact line with a single

microsphere on the solid surface. As the evaporation proceeded, the initially undistorted contact line was pinned at the site of the microsphere; subsequently, it increasingly distorted, slipped across the microsphere, and eventually jumped to a new undistorted position. The pinning force depends on the microstructure of the microsphere; the depinning force, i.e., the elastic force restoring the distorted contact line, is determined by the properties of the liquid itself and the contact angle. Similar contact-line pinning can also occur when a pure liquid droplet is placed on a coarse surface. The imperfections on the surface themselves, such as protuberances, may act in a similar way to the microsphere. Figure 1.7 schematically illustrates the evaporation of a pure water droplet and of a water droplet with colloidal suspension. Upon evaporation, the initial liquid-gas interface (the solid line) at time t_1 shrinks to the dashed line at time t_2 and the contact line moves smoothly from A to B. In the case of water droplet with colloidal suspension, the contact line is pinned at A by the colloid spheres and its retreating from A to B is suppressed. The liquid loss at the contact line during the time span of (t_2-t_1) is replenished by the liquid from the interior as the free surface of the liquid droplet will squeeze the fluid outward to the contact line [81]. The resulting outward capillary flow can carry not only the interior fluid but also the colloidal spheres to the contact line. After the evaporating liquid slipped across the colloidal spheres, the colloidal spheres are deposited on the solid surface, leaving a ring-like deposit along the perimeter. The higher the initial concentration is, the more the colloidal spheres are deposited at the perimeter and the larger the ring width would

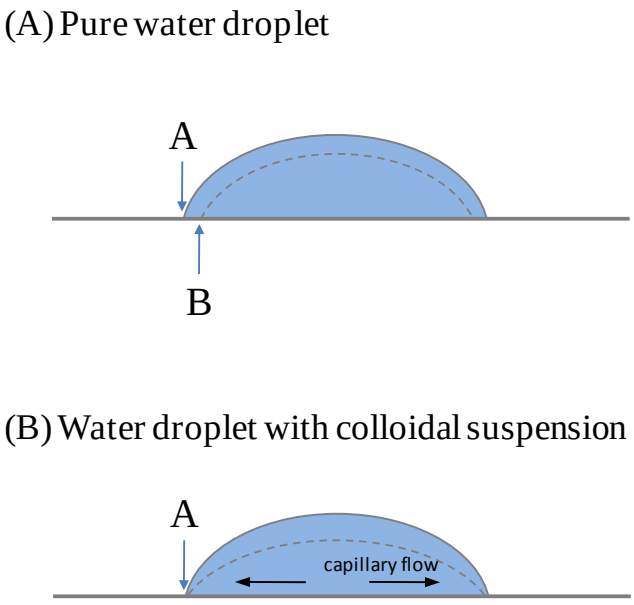

Figure 1.7 Schematic models illustrating (A) the evaporation of a pure water droplet and (B) the evaporation of a water droplet with colloidal suspension. If the contact line is not pinned, like the case shown in (A), the evaporating liquid droplet would shrink from the solid line to the dashed line, and the contact line would move from A to B. If the contact line is pinned, like the case shown in (B), the retreating of the contact line from A to B is forbidden. In this situation, a resulting capillary flow (denoted by the arrows) carries the interior fluid outward to compensate the lost fluid at the contact line.

be. While the pinning force is relaxed due to the deposition of the colloidal spheres on the solid surface, the surface tension is continuously increased due to the evaporation. Once the pinning stress is overcome by the surface tension, the contact line is free to slipping until the next pinning. The repeating slipping-and-sticking motion of the contact line renders a promising opportunity to write fine periodic patterns on solid surfaces. Deegan et al. [81] predicted that the ring patterns can be deposited on different substrates from a wide variety of dispersed materials (solutes) and carrier liquids (solvents) as long as (1) the solvent meets the surface at a non-zero contact angle, (2) the contact line can be pinned

during evaporation, and (3) the solvent is evaporated. It was reported that linear contact line other than circular contact line can also be prepared through a dip-coating [82] or mechanical dragging methods [83]. Different periodic patterns other than homocentric rings can be prepared, such as regular dotted arrays [83, 84] and parallel straight stripes [82, 83].

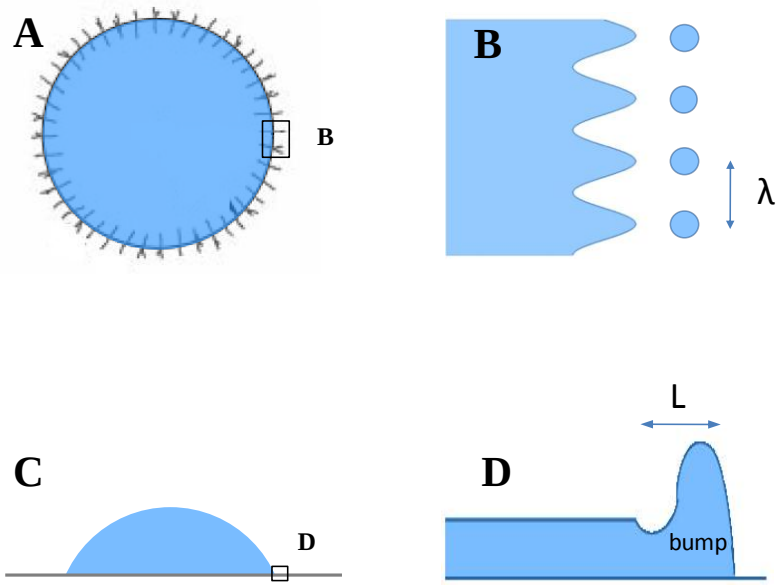

Figure 1.8 Schematic illustration of solutal Marangoni effect and Rayleigh instability of a drying liquid placed on rigid solid surface. For details, see the text.

The evaporation process outlined above is a simplified one. Many other processes may occur simultaneously and modify the evaporation process, resulting in the formation of more complex patterns. The deposition of the solute materials on the substrate decreases the local surface tension of the liquid surface. The surface-tension gradient in turn can trigger a convection flow, known as the 'solutal Marangoni effect' [85, 86] and commonly referred as "fingering instablility" [87]. The as-resulted continuous stripes, i.e., the 'fringers', can further decay into

smaller drops to minimize the free surface energy due to the Rayleigh instability [88, 89]. A well-known example of the fingering instability is ‘tears of wine’ [90]. As illustrated in Figure 1.8, the liquid placed on rigid surface rises up a bit to form bumps at the edge. The instability wavelength λ is determined by this interface profile, i.e., λ is proportional to the transverse size L of the bump. Cazabat found that the λ/L ratio is always close to 4, as reported in the static Rayleigh instability of a liquid cylinder [85, 91].

Deegan [79] examined the depinning of the contact line carefully and found that the depinning process starts from the nucleation of dry holes along the inner edge of the ring-like deposit. The dry holes grow up gradually and merge with the neighboring ones. Depinning occurs when the contact between the liquid and the ring-like deposit is completely cut off by the dry holes. Instead of jumping to the next pinning, the liquid layer retreats backward smoothly until the next pinning, leaving an extremely thin liquid film (< 100 nm) behind the contact line. Such a thin liquid film is then subjected to a quick dewetting.

II. Dewetting

Dewetting is the rupture of a thin liquid film (<100 nm) on a liquid-phobic surface into small droplets. Under evaporating condition, one can also observe the rupture of a thin solution layer on a liquid-philic surface. While a thick liquid film on a solid surface is stable at the action of its gravity [92], the intermolecular interactions get more dominant than the gravity for the thin liquid film [93]. In the

case of a nonvolatile liquid when van der Waals forces are the relevant intermolecular forces, the stability of the thin liquid film is determined by the balance between the disjoining and Laplace pressures [94-96]. Surface tension, expressed by Laplace pressure, tries to keep the thin film flat [97] whereas the disjoining pressure tries to adjust the thickness of the thin film in order to minimize the total free energy [98]. Such a modulation of the free surface of the thin liquid film induced by thermal fluctuation is called spinodal decomposition [94, 99, 100]. Besides thermal fluctuation, spinodal fluctuation can also be induced by mechanical vibrations (in the case of thin pure liquid film), or by concentration gradient (in the case of thin solution layer). The fluctuation of the free surface of the thin liquid film may increase in amplitude, eventually reaches the underneath solid surface, and thus intimates the nucleation of dry holes. It is generally accepted that the dewetting of the thin liquid film begins with the nucleation of dry holes that proceed to grow by pushing the liquid away from the nucleation sites to the retreating rims. Eventually, the growing holes meet and coalescence with their neighbors, forming polygon patterns. The instable ribbons of the polygons will further decay into small droplets in a way similar to Rayleigh instability [88, 89]. These isolated droplets are stable as no material exchange occurs between them. Thus, the dewetting process reaches its end. The whole process described above is schematically illustrated in Figure 1.9. Various patterns can be obtained if one precisely freezes the dewetting process at the desired stage. For the dewetting of pure thin liquid film, the nucleation of dry holes can be triggered either by spinodal

decomposition [94, 99, 100], or by the existing defects, such as tiny particles in the liquid film [101, 102]. In the case of thin solution layer, the solid condensation of the nonvolatile solutes on the solid surface, which can be regards as a kind of defects, also renders preferential sites for the nucleation of dry holes. Upon the appearance of defects in the thin liquid film, liquid around the defects is pushed away and transported to the growing rims around the defects. Eventually, holes are nucleated and grow continuously with the defects remained at the center of holes [103].

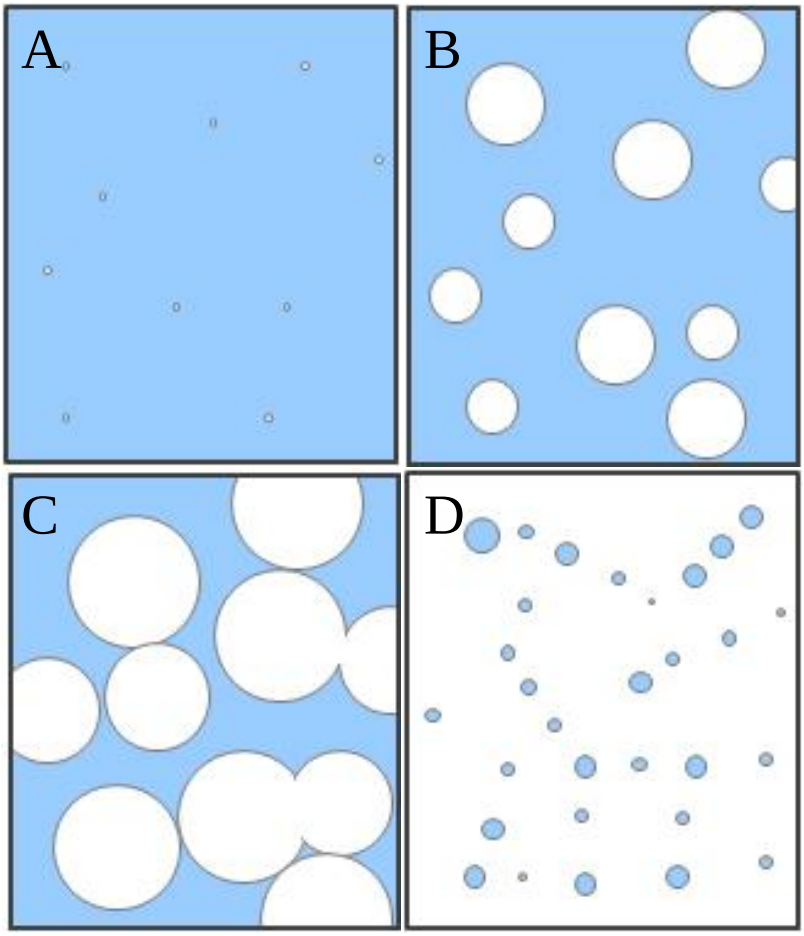

Figure 1.9 Schematic models illustrating the dewetting of a thin liquid film. (A) Nucleation of dry holes; (B) growth of dry holes; (C) coalescence of dry holes to form polygon patterns; and (D) rupture of the instable polygon patterns into small droplets in a way similar to Rayleigh instability.

1.3 Fabrication of Networks of One-Dimensional Nanostructures

1D nanostructures, including nanorods, nanowires, nanobelts, nanotubes and molecule wires, have great implications on various integrated nanodevices because of their unique electronic, optical, and mechanical properties. As a prerequisite for their functional applications, it is essential to prepare oriented 1D nanostructures at desired locations either through direct growth or through post-synthesized assembly. A literature review is presented in the following which summarizes the research activities in the synthesis of complex hierarchical assemblies of 1D nanostructures in the form of 2D or 3D networks or arrays.

1.3.1 Epitaxy Growth

One of the well-known examples is the epitaxy of III-V semiconductors, which is strongly supported by the plenty of available III-V substrates. Tang et al. [104] ascribed the homoepitaxy of horizontally aligned GaN nanowire network on the crystalline GaN substrate by employing a vapor-liquid-solid (VSL) mechanism. The homoepitaxial GaN nanowires were oriented in directions at 60 or 120 ºto each other, commensurate with the crystalline orientation of the GaN substrate. More recently, Menon et al. [105] reported that the networks of hexagonally-aligned GaN nanowires were prepared by heteroepitaxy on the c-face sapphire (Al_2O_3) through a chemical vapor deposition (CVD). Quasi-horizontal GaN nanowire networks can also be prepared on Au-coated MgO substrate via a sublimation sandwich technique, as reported by Chen et al [106]. These GaN nanowire arrays principally

grew along two perpendicular directions and nearly parallel to the substrate.

Due to the lack of II-VI substrates, the epitaxy of II-VI semiconductors is traditionally carried out on the III-V substrates. In the epitaxial growth of ZnSe nanowires and nanorods, Hark et al. [107] found that the epitaxial growth of ZnSe nanowires and nanorods could be vigorously promoted if a high-quality, ZnSe epilayer was first deposited on the GaAs substrate. Note that in all the epitaxial growths mentioned above, the orientation of the products is unchangeable in each specific system. Significantly, Hark et al. obtained the epitaxial ZnSe nanowires and nanorods with tunable orientations by employing the GaAs substrates with different surface lattices. It was reported that epitaxial ZnSe can also be prepared on GaP (111) substrate through a Au-catalyzed VLS deposition [108], where the epitaxial ZnSe nanowires are not parallel to the substrate. Networks of In-SnO_2 nanowires with either three or four-fold growth symmetry have also been epitaxially grown on a- and m-sapphire, respectively [109].

Besides the semiconductors, epitaxial growth of other materials has also been extensively studied. Lucas et al. [110] reported the preparation of CaF_2 nanowires on Si (001) by molecular beam epitaxy (MBE). Both CaF_2 and Si have a FCC crystal structure and the lattice mismatch between them is only 0.6% at room temperature. The epitaxial growth of CaF_2 is attributed to a low density of nucleation sites, the small lattice mismatch, and the anisotropic surface energy of CaF_2 crystals. Chen et al. [111], Badea et al. [112], and Mao et al. [113] ascribed the epitaxial growth of 2D arrays of hexagonally oriented $Pd(NH_3)_4Cl_2 \cdot H_2O$

nanowires, NH_4Cl nanowires, and $CdCl_2.H_2O$ nanorods on mica, respectively. Lamelas et al. [114] reported the epitaxial growth of few alkali halides (KI, RbBr, and CaBr) on mica. They found that a larger lattice mismatch between the alkali halides and mica substrate leads to a lower nucleation density as well as a smaller span of conditions for the epitaxial growth.

1.3.2 Hyperbranch Growth

Alternatively, network architectures could also be prepared by hyperbranch growth as reported in literature [115-117]. One well-known example of hyperbranched structure is the diversely shaped snowflakes [118]. The 3D nature of many hyperbranched crystals, however, leads to even more complex structures than the 2D branched ice.

Alivisatos et al. [116] reported the synthesis of hyperbranched CdTe and CdSe nanocrystals. Such hyperbranched CdTe and CdSe nanocrystals comprise two kinds of crystal structures: cubic zinc blende at the pyramidally shaped branch points and hexagonal wurtzite at their arms. The hyperbranch growth of CdTe and CdSe is possible because these two crystal structures are close in energy and can occur at the same temperature and pressure (polytypism) [119, 120].

Wang et al. [121] reported the growth of aligned cross networks of hyperbranched SnO nanoribbons. It was found that a higher temperature and/or pressure inside the reaction tube favors for a higher yield of the network products. The growth of SnO nanoribbons is possibly associated with the formation of Sn

nanoparticles which is a consequence of the thermal decomposition of SnO. The Sn nanoparticles are liquid droplets at the operating temperature due to their low melting point and serve as the catalyst for the growth of SnO nanoribbons through a VSL mechanism. During growth, more Sn liquid drops may be formed on the surface of the SnO main branches and catalyze the growth of SnO side branches. Instead of employing the metal nanoparticles as the catalyst, Jin et al. [122] obtained hyperbranched PbS an PbSe nanowires by carefully controlling the hydrogen co-flow during the CVD reactions.

Wang et al. [123] also demonstrated the growth of 3D networks of WO_{3-x} nanowires through a thermal evaporation approach. Different from the catalyst-promoted branch mechanism for the growth of hyperbranched SnO, the ordered planar oxygen vacancies existing in the (100) and (001) planes of WO_{3-x} central nanowires promote the growth of the side branches. Besides the oxygen vacancies, screw dislocation defects can also induce the growth of branches as reported by Jin et al. [124] and Cui et al. [125]. Significantly, the axial screw dislocation defect on a central nanowire produces a corresponding Eshelby Twist [126] and promotes the chiral branching of the central nanowire in a VLS growth.

1.3.3 Template-Guided Controlled Growth

Device fabrication often requires nanomaterials to be positioned in well-defined geometries and orientations at specific locations. Whiteside et al. [127] invented a smart method towards a direct growth of oriented inorganic nanocrystals

at desired locations using the predesigned self-assembled monolayers (SAMs) as templates. A typical template comprises of two kinds of alternatively arranged SAMs. One SAM is hydrophobic, the other is hydrophilic. The pitch, i.e., the distance between two neighboring hydrophilic or hydrophobic areas, can be easily adjusted by altering the dimension of the hydrophobic or hydrophilic area between them. The mother phase for crystal growth, either a solution or a vapor phase, can only contact with either the hydrophilic or the hydrophobic areas. As a result, crystals are grown selectively at pre-defined locations. Such a method was first employed to grow calcite nanocrystal arrays [127, 128], and then extended quickly to the synthesis of other nanocrystal patterns [129-131].

Wang et al. [19] ascribed the selective vapor deposition of gold catalyst on a single crystal alumina substrate using the SAMs of PS spheres as the shadow mask. The as-prepared catalyst patterns were then used to guide the growth the hexagonally-aligned ZnO nanorod arrays. Similar catalyst patterns have also been employed for the synthesis of ordered arrays of ZnO pillars [132]. Self-assembled PS spheres also demonstrated themselves as a versatile template in the synthesis of large-scale Si nanowire arrays, as reported by Zhu et al. [133].

1.3.4 Post-Synthesis Assemblies

Besides the spontaneous formation of ordered nanostructures as discussed above, a parallel yet promising approach is the controlled post-synthesis assembly of the colloidal nanostructures prepared by wet chemical methods. The controlled

assemblies can be driven either by a self-motivation process or by applying external force fields.

Lieber et al. [134] developed a Langmuir-Blodgett (LB) technique for the controlled organization of nanowires into parallel or crossed architectures in a layer-by-layer fashion. The as-prepared patterns are in fine regularity over centimeter length scale. The space between the aligned nanowires can be adjusted from micrometer to nanometer scale by compressing carefully the nanowire film floating in the LB trough just before transferring it onto a planar surface. The authors claimed that their method can be used to assemble virtually any kind of nanowire materials into highly ordered arrays. Yang et al. [135] reported the assembly of $BaCrO_4$ nanorods using the similar LB technique. Along with the increase in the pressure at the water-air interface, they observed a pressure-induced isotropic-nematic-smectic phase transitions as well as the transformation from monolayered to multilayered assembly. Yang et al. [136] also demonstrated the alignment of conductive $[Mo_3Se_3^-]_\infty$ nanowires using prefabricated microchannel networks as template. By repeating the patterning steps, multilevel cross-bar junctions and nano-to-macroscale connections have also been successfully achieved.

Starting from a droplet of carbon single-wall nanotubes (SWNTs) suspension, Woolley et al. [137] aligned the carbon SWNTs with controlled orientation on planar surfaces by applying a directional gas flow. Orthogonally aligned arrays were fabricated in a two-step process – the gas flow in the second step was

switched to a direction perpendicular to that in the first step. Similar gas flow method has also been used for the alignment of DNA as reported by Mao et al. [138]. Yarin et al. [139] reported the hierarchical assembly of polymer nanofibers by controlling the electrostatic field as well as the polymer rheology. Parallel arrays were obtained in a one-step assembly and cross-bar arrays in a two-step assembly.

1.3.5 Solvent Evaporation-Mediated Patterning

Yang et al. [140] obtained the radially oriented spokes of gold nanoparticle through a simple solvent evaporation process. Specifically, polymer-coated gold nanoparticles were first floated on a water surface. The dilute film of gold nanoparticles was then transferred to a silicon surface in a dip-coating fashion and was subsequently dried. At the initial stage of drying, the nanoparticles condensed along the contact line in the form of aggregated domains served as the nucleation sites to collect the remaining nanopaticles from the drying film. These domains thus elongated along the retreating contact line to form the radially oriented spokes, similar to the fingers observed in the fingering instability. In another dip-coating experiment, they were successful in achieving a thin wet film of the nanoparticles with straight front edge. Straight parallel stripes of nanoparticles other than the radially oriented spokes were obtained upon drying the thin wet film with straight front edge. Besides the patterning of zero-dimensional (0D) nanoparticles, Yang et al. [140] have also successfully aligned 1D nanowires into parallel stripes by employing a similar drying procedure. Notice that the straight stripes of 0D

nanoparticles are perpendicular to the retreating contact line whereas the straight stripes of the 1D nanowires are parallel to the contact line, indicating different mechanisms were involved. As stated above, the stripes of 0D nanoparticles are a consequence of the fingering instability; however, the stripes of the 1D nanowires are formed because of the repeated stick-slip motion of the contact line.

Besides the patterning of pre-synthesized nanostructures, the solvent evaporation method is also promising in direct patterning of soluble polymers [83, 141]. Xu et al. [142, 143] and Lin et al. [144] reported the gradient concentric ring patterns of the linear conjugated polymer through a repeated stick-slip motion of the receding contact line of the polymer solution. Shimomura et al. [83, 84] demonstrated the formation of regular polymer patterns from a receding meniscus. Through a smart manipulation of the evaporation process, they obtained different structures through different mechanisms: (1) Regularly oriented dots are a consequence of the fingering instability associated the Rayleigh instability; (2) parallel stripes are caused by the repeating stick-slip motion of the receding meniscus of the polymer solution film; (3) ladder structures are a result of the repeating stick-slip motion of the receding meniscus together with the fingering instability. They found that different mechanisms can be switched by adjusting the polymer concentration and the evaporation rate.

1.3.6 Summary – Advantages and Drawbacks of Each Method

The performance of a specific synthetic method can be characterized by the

uniformity in the size and shape as well as in the orientation of the product, the flexibility in materials that can be synthesized, the simplicity of the synthetic procedures, etc.

Guided by the lattice symmetry of the crystalline substrate, the epitaxially grown structures are highly uniform in their orientation. However, the merit on the one hand could possibly be a demerit on the other hand. While the epitaxial features get high uniformity in their orientation, their arrangement on a specific substrate cannot be arbitrarily tuned. This apparently cannot meet the multifarious requirement in practical applications. A feasible manner to adjust the orientation of the epitaxial structures is to employ other substrates (either with the same or with different kind of material) with different lattice symmetries. Thanking for the single crystal growth technique, a large quantity of single crystal substrates is now commercially available, opening up new possibility to tune the epitaxial orientation. When another substrate is used, the lattice match between the epitaxial material and the substrate must be taken into consideration. The uniformity in the size and shape of the epitaxial features may be sacrificed if a larger lattice mismatch is involved. In principle, an atomically uniform epitaxial thin film is possible when the epitaxial material matches well to the surface lattice of the substrate, for example, both the epitaxial material and the substrate belong to the same crystal system and the lattice mismatch is close to zero. The strain energy caused by the lattice mismatch can be relaxed by the creation of 3D islands in the epitaxial film [145], failing the growth of perfect 2D film. The epitaxial growth of anisotropic 1D nanostructures, however,

can endure a relatively larger lattice mismatch. Due to the relatively small dimension, the strain energy accumulated within the linear epitaxial features is small and can be readily relaxed along the sides of the linear features [146]. In principle, it is possible to grow 1D epitaxial nanostructures of a certain kind of material if it has anisotropic lattice mismatches to the substrate along different directions. Generally, the 1D epitaxial nanostructures have a high uniformity in their width whereas no restricted limit in their length. An increase in the lattice mismatch will lead to a wider distribution in their width [147]. Besides, the interaction between the epitaxial material and the substrate is also a crucial parameter of the epitaxial growth. A system with stronger interaction can endure a larger lattice mismatch, as having been demonstrated in many epitaxial growths of ionic crystals [114, 148, 149]. For example, in the epitaxial growth of NaCl on mica, the lattice mismatch is as large as 23%, probably owing to the strong interaction between the ionic NaCl and the polar mica surface. The fact that epitaxial growth can be carried out at both wet solution and dry vapor conditions also largely extends its applicability in practice. The functional applications often require a reasonably large spatial scale of the 1D nanostructure assemblies. The assemblies of 1D epitaxial nanostructures have exceptionally large scales, which is only limited by the size of the substrate. However, these epitaxial assemblies are intrinsically limited in the 2D format. On the country, the hyperbranched networks are originally in the complex 3D format. Compared to the wafer-scale networks prepared by the epitaxial growth, the hyperbranched networks are relatively small

in size. For example, Cui et al. [125] reported that the regular and chiral hyperbranced PbSe networks are usually 10 um x 10 um and 10 um x 50 um, respecitvely. Other structural parameters of the hyperbranched structures, such as the uniformity in the size and shape of the branches, the orientation of their branches, are generally poorer than those in the epitaxial growth. When there is no intrinsic tendency to grow along a particular direction, such as for the cubic crystals, it is more difficult to obtain oriented growth by hyperbranched mechanism [107]. However, this can be easily overcome by epitaxial growth. For example, epitaxial zinc-blende-structured (cubic) nanowires have been achieved by molecular-beam-epitaxy on GaAs (100) and GaP (111) substrates [108, 150]. On the other hand, the hyperbranch growth is not limited by the lattice mismatch compared to the epitaxial growth. For example, Wang et al. [121] found that the growth of the side branches can be induced by the catalyst nanoparticles deposited on the surface of the central branches. Alivisatos et al. [116] also found that the hyperbranched structure can be tuned by varying the amount and kind of organic surfactants. The main issues related to the hyperbranced structures, such as the broad size distribution and the limitation in the material type, may be resolved in future studies. It was demonstrated that 3D networks of 1D features with perfect structural parameters (such as large-scale dimension, uniform size and shape, and uniform orientation) can be obtained by joining the epitaxial growth together with the hyperbranch growth. Jin et al. [151] obtained the wafer-scale, extensively aligned PbS hyperbranched networks on various single substrates through a smart

epitaxy-and-hyperbranch mechanism. With a similar approach, Blamire et al. [152] reported the perfectly aligned and three-dimensionally branched ITO nanowire arrays with a well-controlled growth direction.

The template-guided crystal growth renders a versatile manner to fabricate complex architecture of oriented 1D nanostructures at desirable sites. It takes the advantage of the intrinsic material properties as well as the advantage of the predesigned template. Therefore, an accurate control over the characteristic parameters, such as the density and the spatial arrangement of nucleation events, the uniform size and orientation of the crystals, and the scale of the crystal assemblies, can be simultaneously achieved [127]. One of its intrinsic limitations, however, is that it involves the complicated template-defining processes.

Various assembly techniques offer an economic and simple strategy to fabricate complex architectures from pre-synthesized 1D nanostructures. Generally, it has no limitation in the material type as the starting monomers. However, the assembly processes themselves are unlikely to be perfect. Large-scale ordered assembly strictly requires the starting monomers with high uniformity in their size and shape, which is usually difficult to achieve in the chemically prepared colloidal nanocrystals. With the predefined template, the assembly process may provide accurate control over various structural parameters that are necessary for the functional applications, such as the orientation, the sites, and the pitch (distance between two neighboring monomers).

The evaporation-mediated assembly is attractive due to its simplicity and

versatility in terms of nanomaterials and substrates. The solvent evaporation is a pure physical process, which is only affected by the property of the employed solvent, the interaction between the solvent and the solid surfaces, and the smoothness of the solid surfaces. By carefully programming the evaporation process, it is possible to achieve highly ordered structures with different morphologies and large scales comparable to that in epitaxial growth and template-guided crystal growth. However, complicated processes involved in solvent evaporation make it difficult to predict or design the pattern morphologies. Few excellent examples can be found in literature [83, 84, 144, 145], demonstrating that large-scale periodic patterns can be achieved through the self-assembly processes coupled with irreversible liquid evaporation processes.

1.4 Scopes and Objectives of the Present Work

The above literature survey suggests that epitaxial growth renders an excellent versatility in the preparation of 2D assemblies of linear nanostructures. It is shown that the epitaxial growth largely depends on the interaction between the deposited material and the substrate. An epitaxial system with stronger deposit-substrate interaction allows for a larger lattice mismatch. Therefore, it is advisable to choose intentionally the substrates having strong interaction with the epitaxial material when there is a narrow option for a substrate with zero or small lattice mismatch to the epitaxial material. The first project of this thesis is the epitaxial growth of NaCl on the mica (001) surface. Although the lattice mismatch between NaCl and mica

is as large as 23%, the strong interaction between the ionic NaCl and the polar mica (001) surface is expected to enable the epitaxial growth of oriented NaCl nanostructures.

Previous studies revealed that the epitaxial growth of 1D nanostructures is favorable in the system with anisotropic lattice mismatch, i.e., the epitaxial material and the substrate have different lattice mismatches in different directions. It was noted that materials with highly anisotropic crystal structures can grow into 1D nanostructures. Taking all the above-mentioned information into consideration, the second study in this thesis is the epitaxial growth of $Zn(NO_3)_2.6H_2O$ on mica. $Zn(NO_3)_2.6H_2O$ has a highly anisotropic orthorhombic structure whereas the monoclinic mica substrate has an isotropic (001) surface. An anisotropic lattice mismatch between the orthorhombic $Zn(NO_3)_2.6H_2O$ and the mica substrate is therefore expected. Besides, the interaction between the ionic $Zn(NO_3)_2.6H_2O$ and the polar mica (001) surface could be reasonably high, suggesting the possible epitaxy system allowing for a larger lattice mismatch. Most importantly, the epitaxial $Zn(NO_3)_2.6H_2O$ nanocrystals can be easily converted to ZnO through a thermal treatment due to its low thermal decomposition temperature. The nature of thermal decomposition renders a potential way to fabricate porous ZnO nanostructures.

The solvent evaporation can also be used to write or deposit fine patterns of both pre-synthesized nanostructures and soluble materials on various substrates using different solvents. The third project of this thesis is the evaporation-guided

patterning of anthracene wires on various substrates. The linear polycyclic acenes have recently attracted considerable attention because of their potential for fabrication of organic field-effect transistors (OFETs) [153-157], light emitting diodes (LEDs) [158-161], and sensors [162, 163]. The solution-based growth of tetracene and pentacene nanostructures is less practicable due to their low solubilities in most of organic solvents. Anthracene, on the other hand, exhibits a better solubility in most of organic solvents and chemical stability. Since solution-based process offers a low-cost yet high-efficiency way to fabricate electric and optical nanodevices, it is worthy devoting more systematical studies on the solution-based growth of ordered anthracene nanostructures.

Hydroxylated surfaces of SiO_2, metal oxides, ceramics, and mica modified with physically robust silane coupling agents (SCAs) are of interests with respect to applications in electronics [164, 165] and biosensors [166, 167]. (3-aminopropyl)triethoxysilane (APTES), $H_2N(CH_2)_3Si(OC_2H_5)_3$, is one of the most investigated SCAs. The reactive amino heads of APTES can be further linked to biomacromolecules [168-170], liquid crystals [171], polymers [172, 173], and nanoparticles [174]. In order to obtain homogeneous APTES self-assembled monolayers, various investigations were carried out, including the adsorption from vapor phase [175, 176], the post-adsorption annealing [177], and the employment of anhydrate solvent [178]. Considering the applicability, the self-assembly of APTES from aqueous solution is highly desirable for the surface modification. In this thesis, the self-assembly of APTES on mica from thin aqueous solution layers

was explored. The work was extended to the macroscopic pattern formation of APTES oligomers under non-equilibrium crystallization conditions.

1.5 Organization of the Thesis

After the literature review in Introduction (Chapter 1), the synthetic approaches and various characterization techniques are detailed in Chapter 2. Chapter 3 describes the growth and characterizations of the oriented NaCl nanocrystals on mica. The synthesis of interconnected networks of $Zn(NO_3)_2.6(H_2O)$ nanotubes and its solid-phase transformation into porous zinc oxide architectures are presented in Chapter 4. This is followed by the studies on the synthesis and characterizations of macroscopic concentric ring arrays of radially-oriented anthracene wires (Chapter 5). Chapter 6 presents both the macroscopic surface architectures of self-assembled (3-aminopropyl)triethoxysilane (APTES) and the non-equilibrium crystalline patterns of APTES oligomers. The main results of this thesis together with further studies are summarized in Chapter 7.

References

1. Murray, C. B.; Kagan, C. R.; Bawendi, M. G. *Annu. Rev. Mater. Sci.* **2000,** *30*, 545.

2. Alivisatos, A. P. *Science* **1996**, *271*, 933.

3. Brus, L. *J. Phys. Chem.* **1994**, *98*, 3575.

4. Bawendi, M. G.; Steigerwald, M. L.; Brus, L. E. *Annu. Rev. Phys. Chem.* **1990**,

41, 477.

5. Krans, J. M.; van Rutenbeek, J. M.; Fisun, V. V.; Yanson, I. K.; de Jongh, L. J. *Nature* **1995**, *375*, 767.

6 Al'tshuler, B. L.; Lee, P. A. *Phys. Today* **1988**, *41*, 36.

7. Markovich, G.; Collier, C.P.; Henrichs, S. E.; Remacle, F.; Levine, R. D.; Heath, J. R. *Acc. Chem. Res.* **1999**, *32*, 415.

8. Ahmadi, T.; Wang, Z.; Green, T.; Henglein, A.; ElSayed, M. *Science* **1996**, *272*, 1924.

9. Jin, R.; Cao, Y. W.; Mirkin, C. A.; Kelly, K. L.; Schatz, G. C.; Zheng, J. G. *Science* **2001**, *294*, 1901.

10. Sun, Y.; Xia, Y. ***Science*** **2002**, *298*, 2176.

11. Kim, F.; Connor, S.; Song, H.; Kuykendall, T.; Yang, P. *Angew. Chem. Int. Ed.* **2004**, *43*, 3673.

12. Burda, C.; Chen, X.; Narayanan, R.; El-Sayed, M. A. *Chem. Rev.* **2005**, *105*, 1025.

13. Peng, X.; Manna, L.; Yang W.; Wickham, J.; Scher, E.; Kadavanich, A.; Alivisatos, A. P. *Nature* **2000**, *404*, 59.

14. Meulenkamp, E. A. *J. Phys. Chem. B* **1998**, *102*, 5566.

15. Ding, Y.; Wang, Z. L.; Sun, T. J.; Qiu, J. S. *Appl. Phys. Lett.* **2007**, *90*, 153510.

16. Roy, V. A. L.; Djurisic, A. B.; Liu, H.; Zhang, X. X.; Leung, Y. H.; Xie, M. H.; Gao, J.; Lui, H. F.; Surya, C. *Appl. Phys. Lett.* **2004**, *84*, 756.

17. Zheng, R. K.; Liu, H.; Zhang, X. X.; Roy, V. A. L.; Djurisic, A. B. *Appl. Phys.*

Lett. **2004**, *85*, 2589.

18. Vayssieres, L. *Adv. Mater.* **2003**, *15*, 464.

19. Wang, X. D.; Summers, C. J.; Wang, Z. L. *Nano Lett.* **2004**, *4*, 423.

20. Tian, Z. R. R.; Voigt, J. A.; Liu, J.; McKenzie, B.; McDermott, M. J.; Rodriguez, M. A.; Konishi, H.; Xu, H. F. *Nature Mater.* **2003**, *2*, 821.

21. Huang, M. H.; Wu, Y. Y.; Feick, H.; Tran, N.; Weber, E.; Yang, P. D. *Adv. Mater.* **2001**, *13*, 113.

22. Li, Y.; Meng, G. W.; Zhang, L. D.; Phillipp, F. *Appl. Phys. Lett.* **2000**, *76*, 2011.

23. Arnold, M. S.; Avouris, P.; Pan, Z. W.; Wang, Z. L. *J. Phys. Chem. B* **2003**, *107*, 659.

24. Kong, X. Y.; Wang, Z. L. *Nano Lett.* **2003**, *3*, 1625.

25. Xing, Y. J.; Xi, Z. H.; Xue, Z. Q.; Zhang, X. D.; Song, J. H.; Wang, R. M.; Xu, J.; Song, Y.; Zhang, S. L.; Yu, D. P. *Appl. Phys. Lett.* **2003**, *83*, 1689.

26. Wu, J. J.; Liu, S. C.; Wu, C. T.; Chen, K. H.; Chen, L. C. *Appl. Phys. Lett.* **2002**, *81*, 1312.

27. Hu, J. Q.; Li, Q.; Meng, X. M.; Lee, C. S.; Lee, S. T. *Chem. Mater.* **2003**, *15*, 305.

28. Kong, X. Y.; Ding, Y.; Wang, Z. L. *J. Phys. Chem. B* **2004**, *108*, 570.

29. Law, M.; Greene, L. E.; Radenovic, A.; Kuykendall, T.; Liphardt, J.; Yang, P. D. *J. Phys. Chem. B* **2006**, *110*, 22652.

30. Haldar, K. K.; Sen, T.; Patra, A. *J. Phys. Chem. C* **2008**, *112*, 11650.

31. Zhang, Y.; Jiaqiang Xu, J. Q.; Xiang, Q.; Li, H.; Pan, Q. Y.; Xu, P. C. *J. Phys. Chem. C* **2009**, *113*, 3430.

32. Lao, J. Y.; Wen, J. G.; Ren, Z. F. *Nano Lett.* **2002**, *2*, 1287.

33. Ponzoni, A.; Comini, E.; Sberveglieri, G.; Zhou, J.; Deng, S. Z.; Xu, N. S.; Ding, Y.; Wang, Z. L. *Appl. Phys. Lett.* **2006**, *88*, 203101.

34. Du, Y.; Han, S.; Jin, W.; Zhou, C.; Levi, A. F. *Appl. Phys. Lett.* **2003**, *83*, 996.

35. Xia Y. *Adv. Mater.* **2001**, *13*, 369.

36. Givargizov, E. I. *Highly anisotropic crystals* Reidel, Dordrecht (Netherlands), **1987**.

37. Abraham F. F. *Homogeneous nucleation theory* Academic Press: New York, **1974**.

38. Kenneth A. J. *Kinetic Processes: Crystal Growth, Diffusion, and Phase Transitions in Materials* WILEY-VCH: Weinheim, **2004**.

39. Mullin, W. J. *Crystallization (2nd ed.)* Butterworths: London, **1972**, p142.

40. Walton, A. G. *Mikrochim. Acta* **1963**, *3*, 422.

41. Nielsen, A. E. *J. Phys. Chem. Solids, Suppl. 1: Crystal Growth* **1967**, 419.

42. Leubner, I. H. *J. Phys. Chem.* **1987**, *91*, 6069.

43. Burton, W. K.; Cabrera, N.; Frank, F. C. *Phil. Trans. Roy. Soc. London Ser. A* **1951**, *243*, 299.

44. Šmilauer, P.; Vvedensky, D. D. *Phys. Rev. B* **1995**, *52*, 14263.

45. Bauer, E. G.; van der Merwe, J. H. *Phys. Rev. B* **1986**, *33*, 3657.

46. Fransaer, J. L.; Penner, R. M. *J. Phys. Chem. B*, **1999**, *103*, 7643.

47. Robb, D. T.; Privman V. *Langmuir*, **2008**, *24*, 26.

48. Alivisatos A. P. *Nature* **2005**, *437*, 664.

49. Reiss, H. *J. Chem. Phys.* **1951**, *19*, 482.

50. Ostwald, W. *Lehrbuch der Allgemeinen Chemie* Vol. 2, Leipzig, Germany, **1896**.

51. Peng, X.; Wickham, J.; Alivisatos, A. P. *J. Am. Chem. Soc.* **1998**, *120*, 5343.

52. Herring, C. *Phys. Rev.* **1951**, *82*, 87.

53. Gates, B.; Yin, Y.; Xia, Y. *J. Am. Chem. Soc.* **2000**, *122*, 12582.

54. Mayers, B.; Xia, Y. *Adv. Mater.* **2002**, *14*, 279.

55. Jones, E. T. T.; Chyan, O. M.; Wrighton, M. S. *J. Am. Chem. Soc.* **1987**, *109*, 5526.

56. Martin, C. R. *Science* **1994**, *266*, 1961.

57. Li, M.; Schnablegger, H.; Mann, S. *Nature* **1999**, *402*, 393.

58. Yin, Y.; Lu, Y.; Sun, Y.; Xia, Y. *Nano Lett.* **2002**, *2*, 427.

59. Duan, X. F.; Lieber, C. M. *Adv. Mater.* **2000**, *12*, 298.

60. Duan, X. F.; Lieber, C. M. *J. Am. Chem. Soc.* **2000**, *122*, 188.

61. Morales, A. M.; Lieber, C. M. *Science* **1998**, *279*, 208.

62. Wu, Y.; Yang, P. *Chem. Mater.* **2000**, *12*, 605.

63. Trentler, T. J.; Hickman, K. M.; Geol, S. C.; Viano, A. M.; Gibbons, P. C.; Buhro, W. E. **Science** *1995*, *270*, 1791.

64. Dingman, S. D.; Rath, N. P.; Markowitz, P. D.; Gibbons, P. C.; Buhro, W. E. *Angew. Chem. Int. Ed.* **2000**, *39*, 1470.

65. Trentler, T. J.; Goel, S. C. Hickman, K. M.; Viano, A. M.; Chiang, M. Y.; Beatty, A. M.; Gibbons, P. C.; Buhro, W. E. *J. Am. Chem. Soc.* **1997**, *119*, 2172.

66. Sears, G. W. *Acta Metall.* **1955**, *3*, 367.

67. Zhang, Y.; Wang, N.; Gao, S.; He, R. Miao, S.; Liu, J.; Zhu, J.; Zhang X. *Chem. Mater.* **2002**, *14*, 3564.

68. Manna, L.; Scher, E. C.; Alivisatos, A. P. *J. Am. Chem. Soc.* **2000**, *122*, 12700.

69. Sun, Y.; Gates, B.; Mayers, B.; Xia, Y. *Nano Lett.* **2002**, *2*, 165.

70. Sun, Y.; Xia, Y. *Adv. Mater.* **2002**, *14*, 833.

71. Alivisatos, A. P. *Science* **2000**, *289*, 736.

72. Penn, R. L.; Banfield, J. F. *Geochim. Cosmochim. Acta* **1999**, *63*, 1549.

73. Pacholski, C.; Kornowski, A.; Weller, H. *Angew. Chem. Int. Ed.* **2002**, *41*, 1188.

74. Yu, J. H. Joo, J.; Park, H. M.; Baik, S.; Kim, Y. W.; Kim, S. C.; Hyeon, T. *J. Am. Chem. Soc.* **2005**, *127*, 5662.

75. Adachi, M.; Murata, Y.; Takao, J.; Jiu, J.; Sakamoto, M.; Wang F. *J. Am. Chem. Soc.* **2004**, *126*, 14943.

76. Banfield, J. F.; Penn, R. L. *Science* **1998**, *281*, 969.

77. Young T. *Philos. Trans. R. Soc. London* **1805**, *95*, 65.

78. Adamsoan W. *Physical Chemistry of Surjiaces (4th edition)* Wiley and Sons: New York, **1982**.

79. Deegan R. D. *Phys. Rew. E* **2000**, *61*, 475.

80. Nadkarni, G. D.; Garoff, S. *Europhys. Lett.* **1992**, *20*, 523.

81. Deegan, R. D.; Bakajin, O.; Dupont, T. F.; Huber, G.; Nagel, S. R.; Witten, T. A. *Nature* **1997**, *389*, 827.

82. Huang, J.; Kim, F.; Tao, A.; Connor, S.; Yang, P. *Nature Mater.* **2005**, *4*, 896.

83. Yabu, H.; Shimomura, M. *Adv. Func. Mater.* **2005**, *15*, 575.

84. Karthaus, O.; Gråsjö, L.; Maruyama, N.; Shimomura, M. *Chaos* **1999**, *9*, 308-314.

85. Vuilleumier, R.; Ego, V.; Neltner, L.; Cazabat, A. M. *Langmuir* **1995**, *11*, 4117.

86. Cachile, M.; Cazabat, A. M. *Langmuir 1999, 15*, 1515.

87. Maruyama, N.; Karthaus, O.; Ijiro, K.; Shimomura, M.; Koito, T.; Nishimura, S.; Sawadaishi, T.; Nishi, N.; Tokura, S. *Supramol. Sci.* **1998**, *5*, 331.

88. Eggers J. *Rev. Modern Phys.* **1997**, *69*, 865.

89. Rayleigh, Lord Hoc. *London Math. Soc.* **1878**, *10*, 4.

90. Thomson, J. *Philosophical Magazine*, **1855**, *10*, 330.

91. Cazabat, A. M.; Fournier, J. B.; Carles, P. *Lecture Notes in Fluid Physics* World Scientific: London, **1994**.

92. de Gennes, P. G. *Rev. Mod. Phys.* **1985**, *57*, 827.

93. Israelachvili, J. N. *Intermolecular and Surface Forces* Academic Press: London, **1985**.

94. Vrij, A. *Discuss. Faraday Soc.* **1966**, *42*, 23.

95. Williams, M. B.; Davis, S. H. *J. Colloid Interface Sci.* **1982**, *90*, 220.

96. Reiter, G. *Phys. Rev. Lett.* **1992**, *68*, 75.

97. Adamson, A. W. *Physical Chemistry of Surfaces (5th Ed.)* Wiley and Sons: New York, **1990**.

98. Derjaguin,B. V., Churaev, N. V.; Muller, V. M. *Surface Forces* Consultants Bureau: New York, **1987**.

99. Scheludko, A. Adv. *Colloid Interface Sci. Proc. Int. Conf.* **1977**, *1*, 391.

100. Brochart-Wyart, F.; Daillant, J. *Can. J. Phys.* **1990**, *68*, 1084.

101. Sharma, A.; Ruckenstein, E. *J. Colloid Interface Sci.* **1989**, *133*, 358.

102. Taylor, G. I.; Michael, D. H. *J. Fluid Mech.* **1973**, *58*, 625.

103. Stange T. G.; Evans, D. F.; Hendrickson, W. A. *Langmuir* **1997**, *13*, 4459.

104. Kim, K.; Henry, T.; Cui, G.; Han, J.; Song, Y.-K.; Nurmikko, A. V.; Tang H. *Phys. Stat. Sol. B* **2007**, *244*, 1810.

105. Wu, Z.; Hahm, M. G.; Jung, Y. J.; Menon, L. *J. Mater. Chem.* **2009**, *19*, 463.

106. Jian, J. K.; Wang, C.; Lei, M.; Zhang, Z. H.; Wang, T. M.; Chen, X. L. *Appl. Surf. Sci.* **2008**, *254*, 6637.

107. Zhang, X.; Liu Z.; Li. Q. Leung, Y.; Ip, K.; Hark, S. K. **Adv. Mater.** *2005*, *17*, 1405.

108. Chan, Y. F.; Duan, X. F.; Chan, S. K.; Sou, I. K.; Zhang, X. X.; Wang, N. *Appl. Phys. Lett.* **2003**, *83*, 2665.

109. Nguyen, P.; Ng, H. T.; Kong, J.; Cassell, A. M.; Quinn, R.; Li, J.; Han, J.; McNeil, M.; Meyyappan, M. *Nano Lett.* **2003**, *3*, 925.

110. Loretto, D.; Ross, F. M.; Lucas, C. A. *Appl. Phys. Lett.* **1996**, *68*, 2363.

111. Wang, Z.; Kong, T.; Zhang, K.; Hu, H.; Wang, X.; Hou, J.; Chen, J. *Mater.*

Lett. **2007**, *61*, 251.

112. Motoc, C.; Badea, M. *J. Cryst. Grow.* **1972**, *17*, 337.

113. Deng, Z.; Mao, C. *Langmuir* **2004**, *20*, 8078.

114. Lamelas, F. J.; Seader, S.; Zunic, M. *Phys. Rev. B* **2003**, *67*, 045414.

115. Zhu, J.; Peng, H.; Chan, C. K.; Jarausch, K.; Zhang, X. F.; Cui, Y. *Nano Lett.* **2007**, *7*, 1095.

116. Kanaras, A. G.; So1nnichsen, G.; Liu, H. T.; Alivisatos, A. P. *Nano Lett.* **2005**, *5*, 2164.

117. Yang, R.; Chueh, Y. L.; Morber, J. R.; Snyder, R.; Chou, L. J.; Wang, Z. L. *Nano Lett.* **2007**, *7*, 269.

118. Libbrecht, K.; Rasmussen, P. *The snowflake (1st Ed.)* Voyageur Press: Stillwater, MN, **2003**.

119. Yeh, C. Y.; Lu, Z. W.; Froyen, S.; Zunger, A. *Phys. Rev. B* **1992**, *46*, 10086.

120. Ito, T. *Jpn. J. Appl. Phys.* **1998**, *37*, L1217.

121. Wang, Z. L.; Pan, Z. *Adv. Mater.* **2002**, *14*, 1029.

122. Bierman, M. J.; Lau, Y. K. A.; Jin, S. *Nano Lett.* **2007**, *7*, 2907.

123. Zhou, J.; Ding, Y.; Deng, S. Z.; Gong L.; Xu, N. S.; Wang Z. L. *Adv. Mater.* **2005**, *17*, 2107.

124. Bierman, M. J.; Lau, Y. K. A.; Kvit, A. V.; Schmitt, A. L.; Jin S. *Science* **2008**, *320*, 1060.

125 Zhu, J.; Peng, H.; Marshall, A. F.; Barnett, D. M.; Nix, W. D.; Cui, Y. *Nature Nanotech.* **2008**, *3*, 477.

126. Eshelby, J. D. *J. Appl. Phys.* **1953**, *24*, 176.

127. Aizenberg, J.; Andrew J. Black, A. J.; Whitesides, G. M. *Nature 1999, 398*, 495.

128. Joanna Aizenberg, Andrew J. Black, and George M. Whitesides, *J. Am. Chem. Soc.* **1999**, *121*, 4500.

129. Briseno, A. L.; Mannsfeld, S. C. B.; Ling, M. M.; Liu, S.; Tseng, R. J.; Reese1, C.; Roberts, M. E.; Yang, Y.; Wudl, F.; Bao, Z. *Nature* **2006**, *444*, 913.

130. Hsu, J. W. P.; Tian, Z. R.; Simmons, N. C.; Matzke, C. M.; Voigt, J. A.; Liu, J. *Nano Lett.* **2005**, *5*, 83.

131. Hoeppener, S.; Maoz, R.; Cohen, S. R.; Chi, L. F.; Fuchs, H.; Sagiv, J. *Adv. Mater.* **2002**, *14*, 1036.

132. Fan, H. J.; Lee, W.; Hauschild, R.; Alexe, M.; Rhun, G. L.; Scholz, R.; Dadgar, A.; Nielsch, K.; Kalt, H.; Krost, A.; Zacharias, M.; Göele, U. *Small* **2006**, *2*, 561.

133. Huang Z.; Fang, H.; Zhu J. *Adv. Mater.* **2007**, *19*, 7448.

134. Whang, D.; Jin, S.; Wu, Y.; Lieber, C. M. *Nano Lett.* **2003**, *3*, 1255.

135. Kim, F.; Kwan, S.; Akana, J.; Yang, P. *J. Am. Chem. Soc. 2001*, *123*, 4360.

136. Messer, B.; Jae Hee Song, J. H.Yang, P. *J. Am. Chem. Soc.* **2000**, *122*, 10232.

137. Xin, H.; Woolley, A. T. *Nano Lett.* **2004**, *4*, 1481.

138. Deng, Z.; Mao C. *Nano Lett.* **2003**, *3*, 1545.

139. Zussman, E.; Theron, A.; Yarin, A. L. *Appl. Phys. Lett.* **2003**, *82*, 973.

140. Huang, J.; Fan, R.; Connor, S.; Yang, P. *Angew. Chem. Int. Ed.* **2007**, *46*,

2414.

141. van Hameren, R.; Schön, P.; van Buul, A. M.; Nolte, R. J. M. *Science* **2006**, *314*, 1433.

142. Hong, S. W.; Xu, J.; Xia, J.; Lin, Z.; Qiu, F.; Yang, Y. *Chem. Mater.* **2005**, *17*, 6223.

143. Xu, J.; Xia, J.; Hong, S. W.; Lin, Z.; Qiu, F.; Yang, Y. *Phys. Rev. Lett.* **2006**, *96*, 066104.

144. Hong, S. W.; Xu, J.; Lin, Z. *Nano Lett.* **2006**, *6*, 2949.

145. Petroff, P. M.; DenBaars, S. P. *Superlattices Microstruct.* **1995**, *15*, 15.

146. Jacob, K. T.; Attaluri, M. *J. Mater. Chem.* **2003**, *13*, 934.

147. Kavanagh, K. L.; Reuter, M. C.; Tromp, R. M. *J. Cryst. Growth* **1997**, *173*, 393.

148. Wu, J. H.; Ang S. G.; Xu G. Q. *J. Phys. Chem. C* **2008,** *112*, 7605.

149. Lamelas, F. J.; Schmidt, J. D.; Xiong, M. *Phys. Rev. B* **1998**, *58*, 14270.

150. Wu, Z. H.; Mei, X.; Kim, D.; Blumin, M.; Ruda, H. E.; Liu, J. Q.; Kavanagh, K. L. *Appl. Phys. Lett.* **2003**, *83*, 3368.

151. Lau, Y. K. A.; Chernak, D. J.; Bierman, M. J.; Jin, S. *J. Mater. Chem.* **2009**, *19*, 934.

152. Wan, Q.; Wei, M.; Zhi, D.; MacManus-Driscoll, J. L.; Blamire, M. G. *Adv. Mater.* **2006**, *18*, 234.

153. Dimitrakopoulos, C. D.; Mascaro, D. J. *Adv. Mater.* **2002**, *14*, 99.

154. Katz, H.; Bao, Z.; Gilat, S. *Acc. Chem. Res.***2001**, *34*, 359.

155. Dimitrakopoulos, C. D.; Brown, A. R.; Pomp, A. *J. Appl. Phys.* **1996**, *80*, 2501.

156. Lin, Y. Y.; Gundlach, D. J.; Nelson, S.; Jackson, T. N. *IEEE Trans. Electron Devices* **1997**, *44*, 1325.

157. Kelly, T. W.; Boardman, L. D.; Dunbar, T. D.; Muyres, D. V.; Pellerite, M. J.; Smith, T. P. *J. Phys. Chem. B* **2003**, *107*, 5877.

158. Kan, Y.; Wang, L. D.; Gao, Y. D.; Duan, L.; Wu, G. S.; Qiu, Y. *Syn. Met. 2004*, *141*, 245.

159. Kitamura, M.; Imada, T.; Arakawa, Y. *Appl. Phys. Lett.* **2003**, *83*, 3410.

160. Lee, Y. S.; Park, J. H.; Choi, J. S. *Opt. Mater. 2003*, *21*, 433.

161. Jiang, X. Y.; Zhang, Z. L.; Zheng, X. Y.; Wu, Y. Z.; Xu, S. H. *Thin Solid Films* **2001**, *401*, 251.

162. Kaur, G.; Fang, H.; Gao, X. M.; Li, H. B.; Wang, B. H. *Tetrahedron* **2006**, *62*, 2583.

163. Wang, Z.; Zhang, D. Q.; Zhu, D. B. *J. Org. Chem.* **2005**, *70*, 5729.

164. Lehn, J.-M. *Angew. Chem. Int. Ed. Engl.* **1990**, *29*, 1304.

165. Haddon, R. C.; Lamola, A. A. *Proc. Natl. Acad. Sci. USA* **1985**, *82*, 1874.

166. Endo, T.; Kerman, K.; Nagatani, N.; Takamura, Y.; Tamiya, E. *Anal. Chem.* **2005**, *77*, 6976.

167. Perrin, A.; Lanet, V.; Theretz, A. *Langmuir* **1997**, *13*, 2557.

168. Hu, J.; Wang, M.; Weier, H.-U. G.; Frantz, P.; Kolbe, W.; Ogletree, D. F.; Salmeron, M. *Langmuir* **1996,** *12*, 1697.

169. Doh, J.; Irvine, D. J. *Proc. Natl. Acad. Sci.* **2006**, *103*, 5700.

170. Shin, M.; Kwon, C.; Kim, S. -K.; Kim, H. -J.; Roh, Y.; Hong, B.; Park, J. B.; Lee. H. *Nano Lett.* **2006**, *6*, 1334.

171. Heiney, P. A.; Grüneberg, K.; Fang, J.; Dulcey, C.; Shashidhar, R. *Langmuir* **2000,** *16*, 2651.

172. Tsukruk, V. V.; Bliznyuk, V. N.; Visser, D.; Campbell, A. L.; Bunning, T. J.; Adams, W. W. *Macromolecules* **1997**, *30*, 6615.

173. Chang, Y.-C.; Frank, C. W. *Langmuir* **1998**, *14*, 326.

174. Zheng, J. W.; Zhu, Z. H.; Chen, H. F.; Liu, Z. F. *Langmuir* **2000**, *16*, 4409.

175. Kurth, D. G.; Bein, T. *Langmuir* **1995**, *11*, 3061.

176. Haller, I. *J. Am. Chem. Soc.* **1978**, *100*, 8050.

177. Pasternack, R. M.; Amy, S. R.; Chabal, Y. J. *Langmuir* **2008,** *24*, 12963.

178. Kallury, K. M. R.; Macdonald, P. M.; Thompson, M. *Langmuir* **1994,** *10*, 492.

Chapter 2

Synthesis and Characterizations of Ordered Nanostructures

2.1 Introduction

In this chapter, the fabrication and characterizations of ordered nanostructures through fast drying of thin solution layers are described. The details for the preparation of thin solution layers on various solid surfaces are provided. Strategies toward the irreversible fast drying of thin solution layers are presented together with the schematic illustration of experimental setup. A description of the thermal decomposition towards porous structures and the routes for patterning thin gold films are also included. The as-prepared nanostructures were characterized using various analytical techniques. Morphological characterization was conducted using a wide range of microscopic techniques, including atomic force microscopy (AFM), scanning electron microscopy (SEM), field-emission SEM (FESEM), transmission electron microscopy (TEM), bright-field and polarized optical microscopy (OM). Crystallographic and compositional information was obtained with powder X-ray diffraction (XRD), selected area electron diffraction (SAED), and energy dispersive X-ray spectroscopy (EDS). Conductivity measurement was carried out using two-probe electrical measurement inside the vacuum chamber of a FESEM (detailed in Chapter 4). Optical properties were studied by employing photoluminescence (PL) spectroscopy and fluorescence microscopy (FM). A brief introduction on the working principle of each technique is presented.

2.2 Fabrication of Ordered Nanostructures on Various Substrates

2.2.1 Substrate Selection and Cleaning

Clean and smooth surfaces are required for the fabrication of ordered nanostructures. Substrates employed in our experiments include Si (with native SiO_2 layer), glass, HOPG, and mica ($KAl_2(Si_3AlO_{10})(OH)_2$). Besides the hydrophobic HOPG; the other substrates are hydrophilic. Clean HOPG and mica surfaces were prepared by cleavage in ambient air. Clean Si and glass substrates are prepared by successive ultrasonication procedures: (1) in washing detergent, 5 min; (2) in Milli-Q water (Millipore, ≥18 $M.cm^{-1}$) for 3 times, 5 min for each; (3) in piranha solution (H_2SO_4:H_2O_2 = 7:3), 30 min; (4) in Milli-Q water for 3 times, 5 min for each.

2.2.2 Preparation of Thin Solution Layers on Solid Surfaces

To prepare the thin solution layer, a solvent-philic substrate was chosen. As schematically illustrated in Figure 2.1A, a solution droplet (~20 μL) was pipetted onto the freshly cleaned substrate and then quickly removed by N_2 flow. Such a process resulted in the formation of a thin solution layer on the solvent-philic substrate.

Thin solution layers can be prepared simply by pipetting a solution droplet onto the freshly cleaned substrate. Under the action of gravity, the solution droplet will spread out to form thin solution layer as long as the substrate is not highly solvent-phobic. Another approach towards the thin solution layer with uneven

thickness is schematically illustrated in Figure 2.1B. A hump was placed at the downstream of N_2 flow to block the solution droplet from leaving the substrate. As a result, a thin solution layer with uneven thickness was formed on the substrate, which is thick at the end close to the hump but thin at the other end far from the hump.

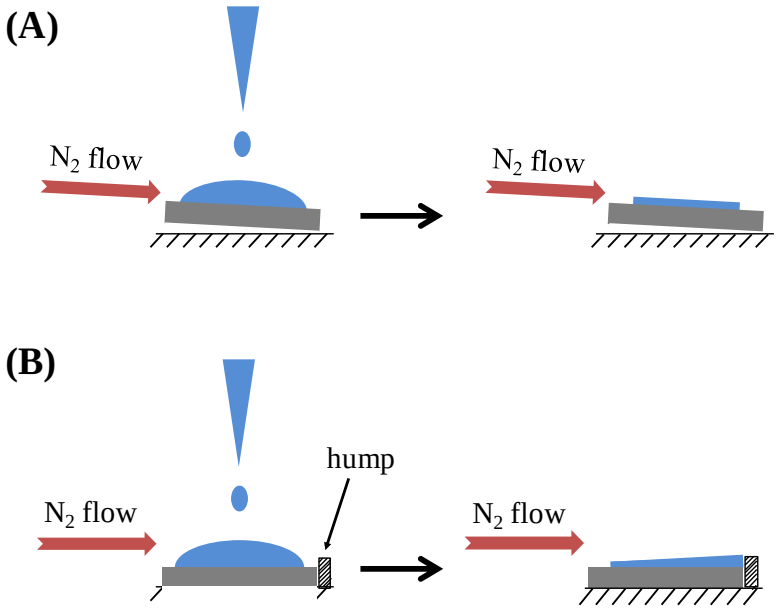

Figure 2.1 Experimental setup for preparing (A) thin solution layer on a solvent-philic substrate, and (B) thin solution layer with uneven thickness.

2.2.3 Fast Drying of Thin Solution Layers

Fast drying of the thin solution layers was achieved by: (1) fast evaporation in N_2 atmosphere and/or in desiccators containing blue porous silica gel; (2) employing volatile solvents with relatively low boiling points (b.p.), such as toluene (b.p. 110 ℃) and acetone (b.p. 56 ℃). More detailed description is provided in the experimental parts of Chapters 3-6.

2.2.4 Patterning of Thin Gold Films

Long-range ordered NaCl nanocrystal arrays were used as templates for patterning thin gold films. The growth of ordered NaCl nanocrystal arrays is presented in Chapter 3. As schematically illustrated in Figure 2.2, two methods were employed for patterning thin gold films, namely peeling-off (Figure 2.2A) and direct-dissolution method (Figure 2.2B). Steps involved in the peeling-off patterning include: (i) Thin gold film (10 nm thickness) was sputter-coated on the NaCl-covered mica slice. (ii) A drop of epoxy adhesive was applied onto the top of gold film. (iii) The gold film was peeled off after the epoxy adhesive had been solidified.

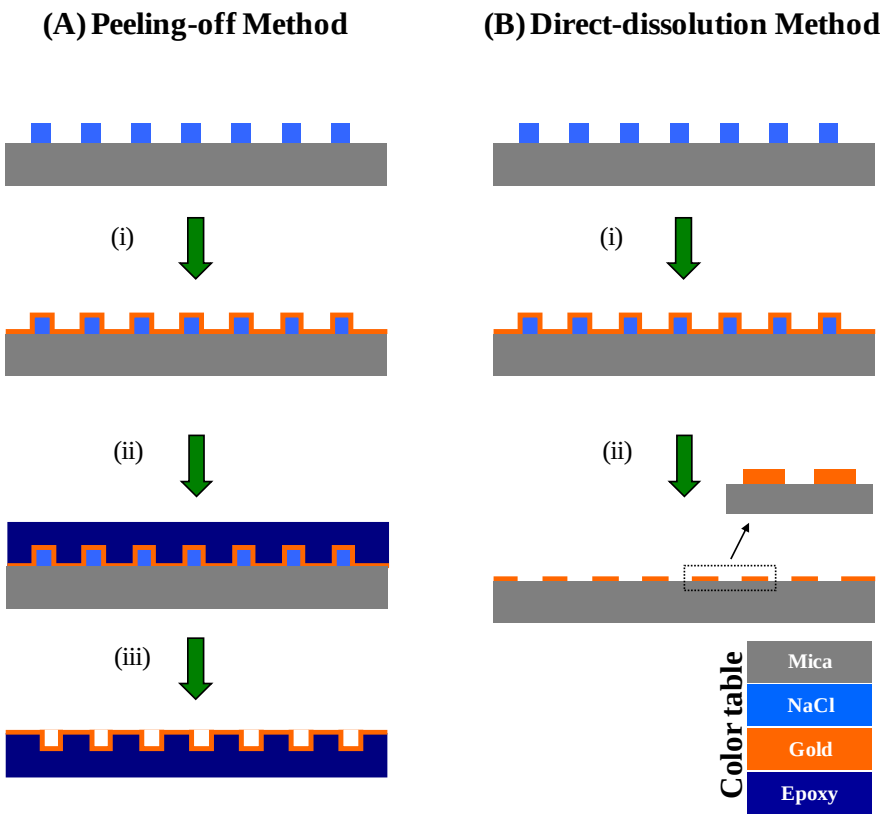

Figure 2.2 Patterning of thin gold films: (A) Peeling-off method: (i) sputter coat thin gold film; (ii) apply epoxy adhesive; and (iii) peel off the thin gold film. (B) direct-dissolution method: (i) sputter coat thin gold film; (ii) The gold deposited on the top of NaCl was removed while ultrasonicating in Milli-Q water.

In the direct-dissolution patterning, thin gold film (10 nm thickness) was first sputter-coated on the NaCl-covered mica slice. The sample was then immersed in Milli-Q water and ultrasonicated for 5 min to dissolve the NaCl nanocrystals. The gold deposited on the top of the NaCl nanocrystals would be removed when the NaCl supporter was dissolved during ultrasonication; whereas the gold deposited directly on the mica surface was retained.

2.2.5 Thermal Decomposition towards Porous Structures

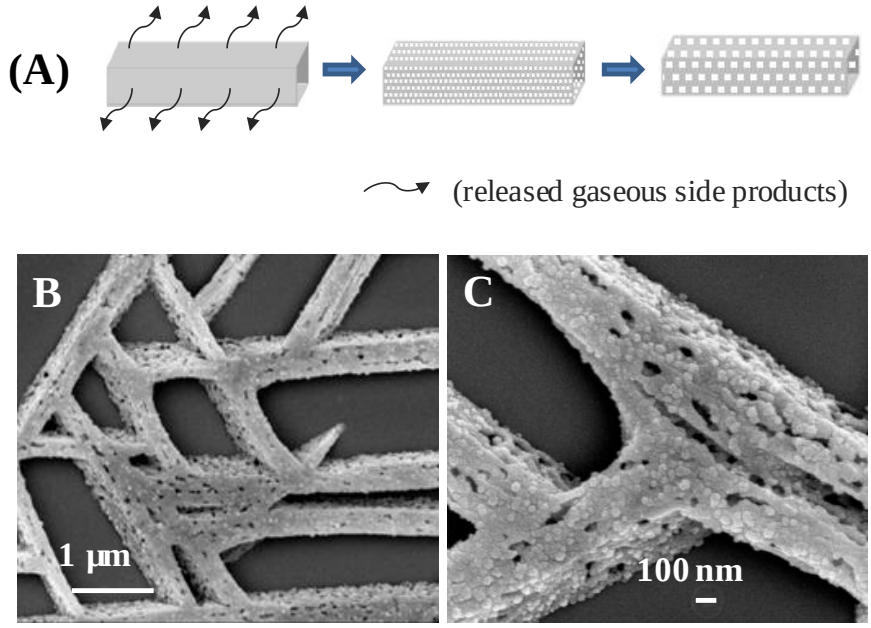

Figure 2.3 (A) Schematic model illustrating the formation of pores in the solid precursors as a result of releasing the gaseous side products. (B) SEM image showing the resulted porous ZnO structures after the thermal annealing. (C) Close-up view of (B).

To prepare porous structures, solid precursors with low decomposition temperatures were annealed in a furnace (Barnstead Thermolyne, F4800 Furnace) at different temperatures for various lengths of time. The release of gaseous

products during thermal decomposition resulted in the formation of porous structure (Figure 2.3) [1, 2].

2.3 Characterizations

2.3.1 Atomic Force Microscopy (AFM)

AFM employs a probe to sense the surface topography of the objects to be tested, in a similar way that we use our fingers to feel the environment in a dark or dim situation. The AFM probe has a sharp tip with particular curvature radius < 10 nm. The smaller the tip radius is, the better the resolution would be. To achieve extremely high sensitivity and resolution, AFM must be capable of controlling the tip-sample interactions with great precision; it must also be able to detect the very tiny variation in the tip-sample interactions and to convert it accurately into topographic information [3]. In practice, the precise control of the tip-sample interaction is accomplished with the use of an electronic feedback loop, which can adjust the tip-to-surface distance to keep a constant tip-specimen interaction at a user-specified setpoint level. As schematically illustrated in Figure 2.4, the AFM probe is mounted on a cantilever. A laser beam is directed on the back of the cantilever. The laser beam reflected off the cantilever back is detected by a position sensitive detector (PSD) consisting of two closely packed photodiodes. When the AFM probe is brought extremely close to the sample surface, the tip-sample attractive force is greatly increased. The cantilever is forced to distort in order to keep the tip-sample interaction at the user-specified level. The angular

displacement of the cantilever in turn causes the deviation of the laser beam position reached the PSD. Consequently, one photodiode collects more light than the other. The output signal (the difference between the photodiode signals normalized by their sum) is proportional to the angular displacement of the cantilever. Attributed to the long path of the laser beam (typically several cm), a small angular displacement of the cantilever can be amplified into a much larger changes in the output signal. By this way, AFM can detect the cantilever deflection less than 1 Å. That is why AFM can achieve a high Z-direction resolution < 1 Å.

Traditionally, the AFM probe is maintained immobile during scanning. The movements in the X, Y, and Z directions are accomplished by AFM sample that is mounted on a scanner that houses a piezoelectric tube or three individual piezoelectric crystals. Alternatively, the Z-direction movement is realized by the AFM probe that is mounted on a vertical piezoelectric scanner; the movements in the X and Y directions are done by the sample mounted on another independent piezoelectric block.

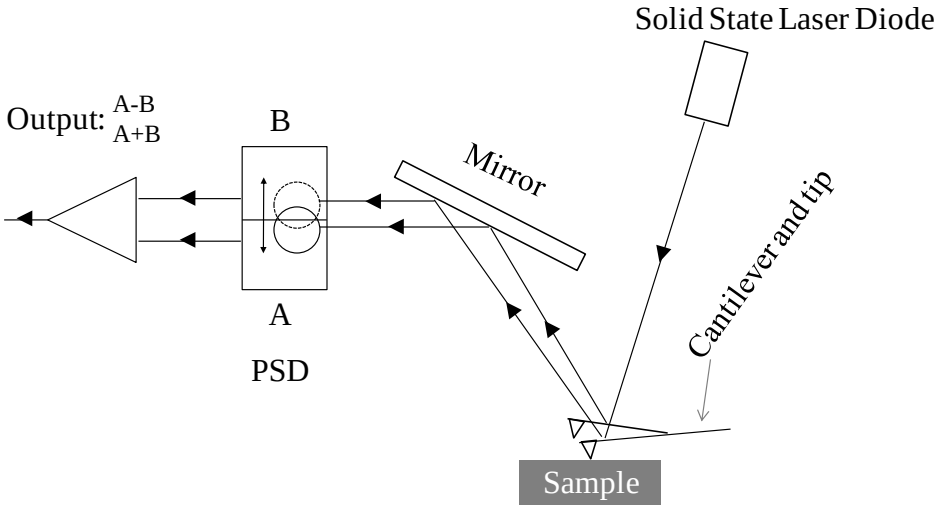

Figure 2.4 Schematic illustration of AFM working principle.

AFM is capable of measuring almost all kinds of tip-sample interactions, including mechanical contact force, van der Waals forces [4], capillary forces [5, 6], chemical bonding [7, 8], adhesion forces [9], electrostatic forces [10], magnetic forces [11, 12], Casimir forces [13], solvation forces [14], etc. By employing conductive probes, it can even measure the conductivity of sample - so-called conductive AFM [15, 16]. Besides topographic imaging, other major applications of AFM include force spectroscopy [17, 18] and dip-pen nanolithography [19-21].

AFM can be operated in several modes. Among of them, contact and tapping modes are most frequently used in practical applications. In contact mode, the AFM probe is in contact with the sample surface under the strong action of attractive force. The overall tip-sample interaction force is repulsive. While the sample is scanned under the AFM tip in the X and Y directions. Features on the sample surface force the cantilever to deflect, which in turn alter the output signal of the PSD. The feedback loop moves the sample in the Z direction accordingly to keep a constant tip-sample interaction. In order to boost the cantilever deflection and to reduce the lateral dragging force during scanning, low stiffness cantilevers with triangular configuration are used in contact AFM.

In tapping mode, the cantilever with rectangular configuration is externally oscillated at or close to its resonance frequency. The oscillation parameters (amplitude, phase and resonance frequency) are modified by the tip-sample interactions. The changes in oscillation parameters therefore deliver the information about the surface topography. If the topographic information is

provided by the changes in the oscillation frequency, it is called the frequency modulation. Stiff cantilevers are often employed in the frequency modulation as they provide greater stability when the AFM tip is brought very close to the sample surface. Usually it is easy to achieve a high resolution in the frequency modulation as the oscillation frequency can be measured with a very high sensitivity. If the information is presented by the changes in the oscillation amplitude or phase, it is called amplitude modulation. The variations in the oscillation phase provide image contrast caused by difference in surface adhesion and viscoelasticity, useful for the discrimination between different types of materials.

AFM has several advantages compared to other electron microscopic techniques such as SEM. It can work perfectly well in ultra-high vacuum (UHV) as well as in ambient and even liquid environments. The liquid AFM is particularly suitable for studying biological samples in living environment. In contrast, the electron microscopes (both SEM and TEM) require expensive UHV environment for proper operation. In principle, AFM can achieve a high resolution at atomic level, comparable to STM and TEM but higher than SEM. Unlike the electron microscopes that provide two-dimensional (2D) information of the sample surface topography, AFM can deliver true three-dimensional (3D) surface topography. While the electron microscopes require the samples to be well conductive, AFM can view both conductive and non-conductive samples and does not require complex sample preparation. The maximum scan size and resolution of AFM imaging depend on the choice of scanner. While SEM can view an area on the

order of millimeters with a depth of field on the order of millimeters, AFM can only image a maximum height on the order of 10-20 μm and a maximum area of around 150 x 150 μm^2. In principle, the scanner that can image a larger area has a poorer resolution at small-area imaging. The other disadvantage of AFM is the slow scan rate, resulting in the low output of AFM imaging. Typically, it takes several minutes to capture one AFM image (256 x 256 pixels). Fast-acting AFM has been proposed to improve the scanning productivity [22, 23]. Additionally, several factors can cause artificial and/or deformed AFM images, such as the hysteresis of the piezoelectric materials, the thermal drift, etc. Experiences are required to eliminate the artificial AFM imaging [24, 25]

2.3.2 Scanning Electron Microscopy (SEM) and Field-Emission SEM (FESEM)

When high-energy electron beam interacts with the atoms at or near the sample surface, as schematically illustrated in Figure 2.5, it produces several signals including secondary electrons, back-scattered electrons (BSE), characteristic X-rays, light (cathodoluminescence photons), and transmitted electrons. The as-produced signals contain the information about surface topography, composition, electrical conductivity, etc. SEM employs high-energy electron beam to scan the sample in a raster mode. In the standard detection mode, SEM collects the secondary electron signal and renders information about the sample surface topography. The characteristic X-ray signals are related to the elemental

composition of the sample in the energy dispersive X-ray spectroscopy (EDS).

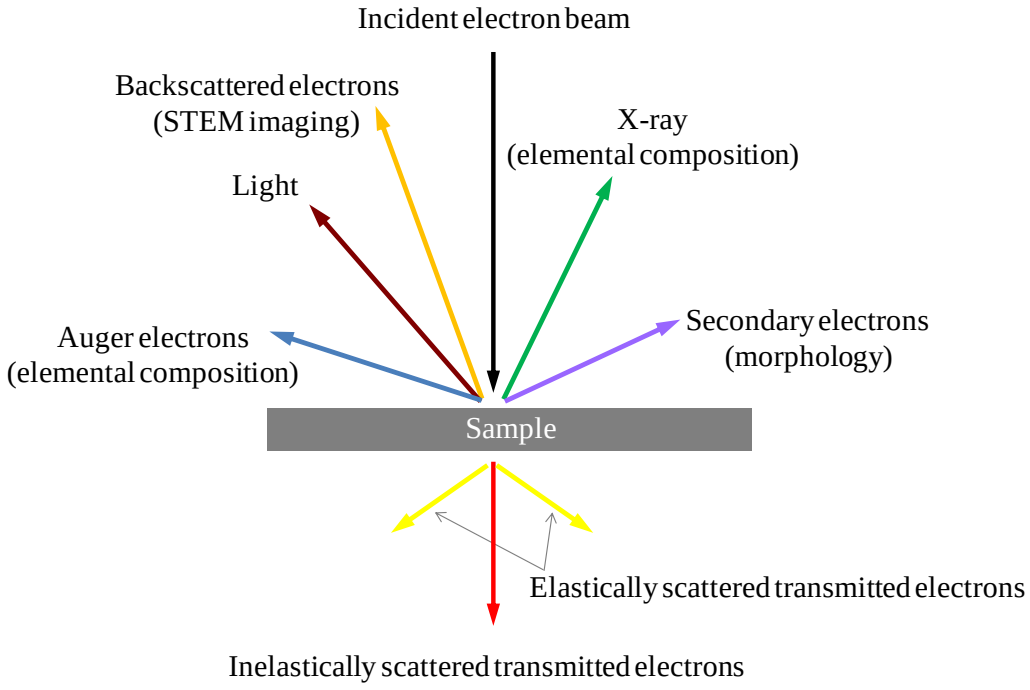

Figure 2.5 Interaction between the incident electron beam and the sample. The produced signals and the information they contain are given. STEM stands for scanning transmission electron microscopy.

The imaging resolution of SEM is largely determined by the diameter of the incident electron beam and the energy of the incident electrons. FESEM employs a field emission gun to produce electron beam with smaller diameter and greater electron density. Therefore, FESEM can achieve significantly higher spatial resolution than the conventional SEM.

Although environmental SEM is available since 1980s [26, 27], the SEM imaging is basically operated under vacuum conditions. It requires the sample to be conductive. Otherwise, the conductive coating is required. However, the conductive coating may conceal small features on the sample surfaces and makes the EDS analysis difficult.

2.3.3 Transmission Electron Microscopy (TEM)

TEM works on a similar principle as the transmission optical microscope (OM) but uses high-energy electron beam instead of natural light beam for the purpose of illumination. The resolution of OM is limited by the wavelength of light source (λ) [28]:

$$d = \frac{\lambda}{2n\sin\theta} = \frac{\lambda}{2NA}$$

where NA is the numerical aperture of the system.

For electrons, the de Broglie wavelength is dependent on their kinetic energy [29]:

$$\lambda_e \approx \frac{h}{\sqrt{2m_e E\left(1+\frac{E}{2m_e c^2}\right)}}$$

where h is Planck constant; c, the speed of light; m_e, the rest mass of electron; and E, the kinetic energy of electrons. By employing greatly accelerated electrons, TEM imaging can achieve a high resolution at atomic level.

To make sure that the electron beam can transmit through the samples, TEM requires the samples to be thin (at most hundreds nanometers in thickness). For this reason, the preparation of ultrathin TEM sample sometimes can be challenging.

Besides imaging, another major application of TEM is selected area electron diffraction (SAED). In SAED, the periodic atom arrays in the crystalline samples serve as the diffraction grating to the incident electrons. The resulting SAED patterns can provide valuable information about the crystal structures of the samples [30]. More detailed description of the diffraction phenomenon is given in the introduction of X-ray diffraction (XRD).

2.3.4 Polarized Optical Microscopy (OM)

Different from the normal (bright-field) optical microscope which uses a natural light for illumination, the polarized optical microscope employs a linearly polarized light for the purpose of illumination. The linearly polarized light can be obtained using a polarizing filter (polarizer), as illustrated in Figure 2.6. It is known that isotropic materials exhibit the same optical properties in all directions. The electromagnetically anisotropic materials, such as single crystals, exhibit direction-dependent optical properties when interacting with polarized light. This makes the polarized OM particularly suitable for the study of anisotropic crystalline structures [32-35]. As illustrated in Figure 2.7, the anisotropic materials appear dark when their optical axes are perpendicular to the vibration directions of polarizer and analyzer [36]. Such positions are called the extinction positions. The anisotropic materials display the maximum brightness at the diagonal position when their optical axes are at 45 ^{o} to the vibration directions of polarizer and analyzer.

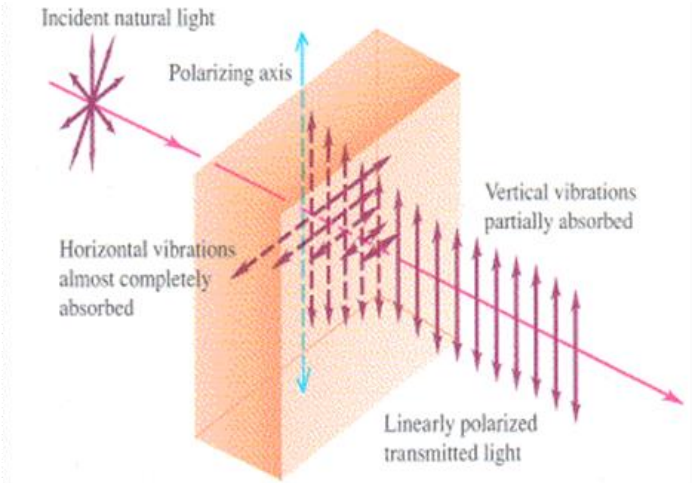

Figure 2.6 Linearly polarized light produced by a polarizing filter. Reproduced from [31].

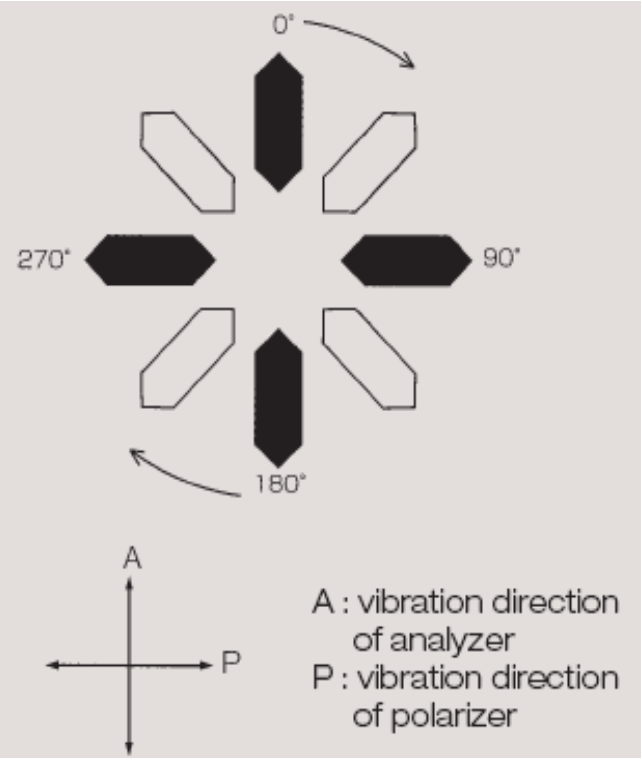

Figure 2.7 Extinction and diagonal positions of anisotropic materials. Reproduced from [37].

2.3.5 X-ray diffraction (XRD)

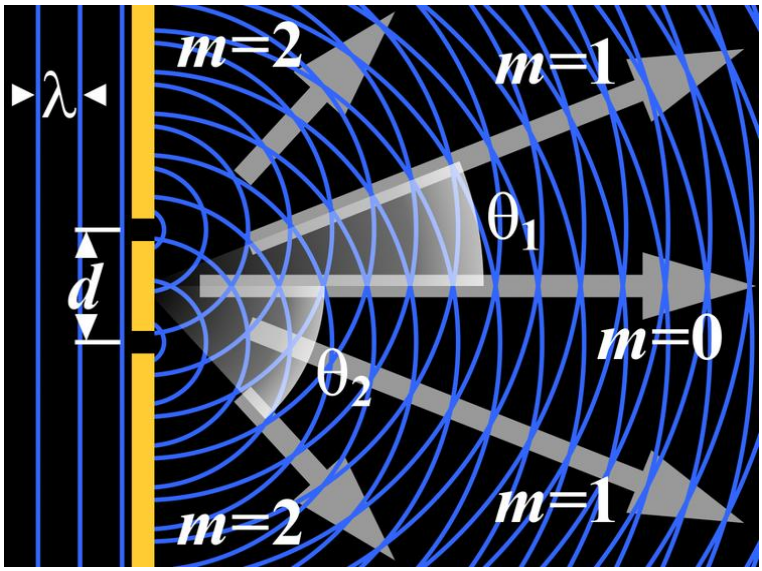

Figure 2.8 Illustration of wave diffraction.

When electromagnetic wave encounters an obstacle, various optical phenomena may be arisen, including reflection, refraction, interference, diffraction, and polarization. If the obstacle has a small size on the order of the wavelength of the electromagnetic wave, pronounced diffraction can occur as illustrated in Figure 2.8.

Crystals are comprised of a set of parallel lattice planes. The separation between the lattice planes (d) is on the order of the wavelength of X-ray. When the X-ray strikes on the crystal, the lattice planes serve as periodic scatters that produce a regular array of secondary spherical waves (Figure 2.9). This phenomenon is known as elastic scattering. These spherical waves interact with each other, resulting in either destructive interference (signal subtraction) or constructive interference (signal addition). X-ray diffraction is a consequence of constructive interference between the secondary waves when they meet the conditions given by Bragg's law:

$$2d\sin\theta = n\lambda$$

where λ is the wavelength of the X-ray; d, the separation between the lattice planes; θ, the angle of the diffracted wave; and n, an integer known as the order of the diffraction beam. The X-ray diffraction pattern provides information about the crystallographic structure of the sample to be studied.

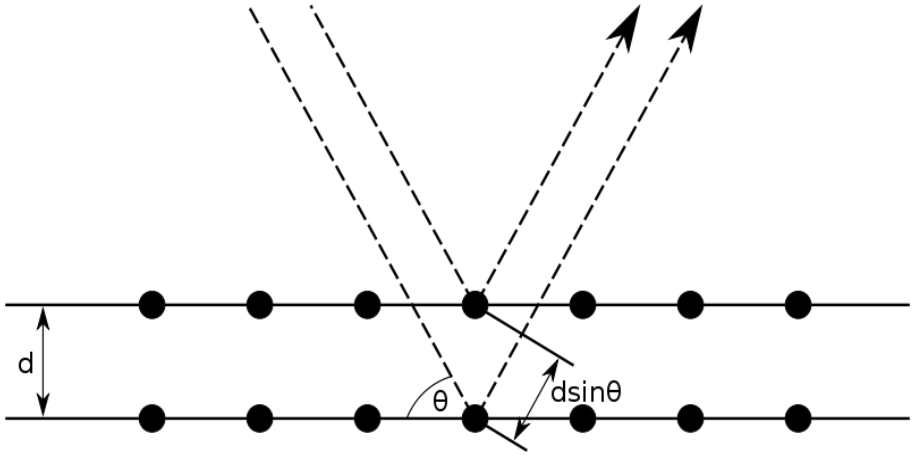

Figure 2.9 Illustration of Bragg condition for the constructive interference.

2.3.6 Electrical Probing for Conductivity Measurement

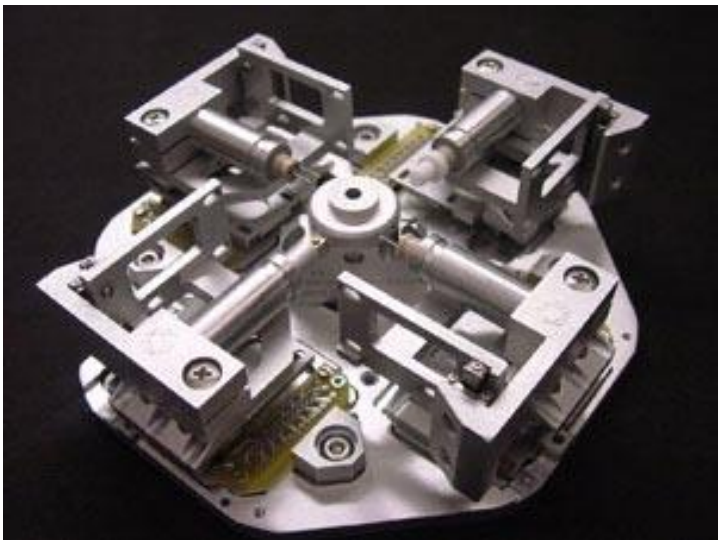

Figure 2.10 Four-positioner nanomanipulator system (sProber Nano-M, Zyvex Instruments) built in the vacuum chamber of an FESEM.

Figure 2.10 shows the four-positioner nanomanipulator system (sProber Nano-M, Zyvex Instruments) built in the vacuum chamber of an FESEM tool. The piezo-controlled tungsten nanoprobes have a tip size typically < 50 nm so that nanosized structures can be directly probed in a similar way for probing macroscopic objects. The system (FESEM together with sProber Nano-M) can

simultaneously read out the current-voltage (I-V) curves and capture the FESEM image (Figure 2.11).

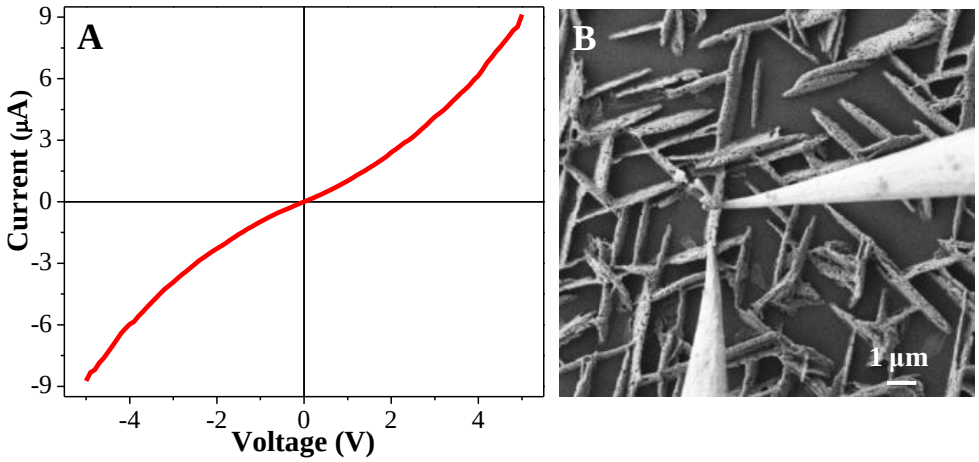

Figure 2.11 (A) I-V curve, and (B) SEM image showing the electrical probing of the interconnected networks of ZnO nanotubes [2].

2.3.7 Photoluminescence spectroscopy (PL) and Fluorescence Microscopy (FM)

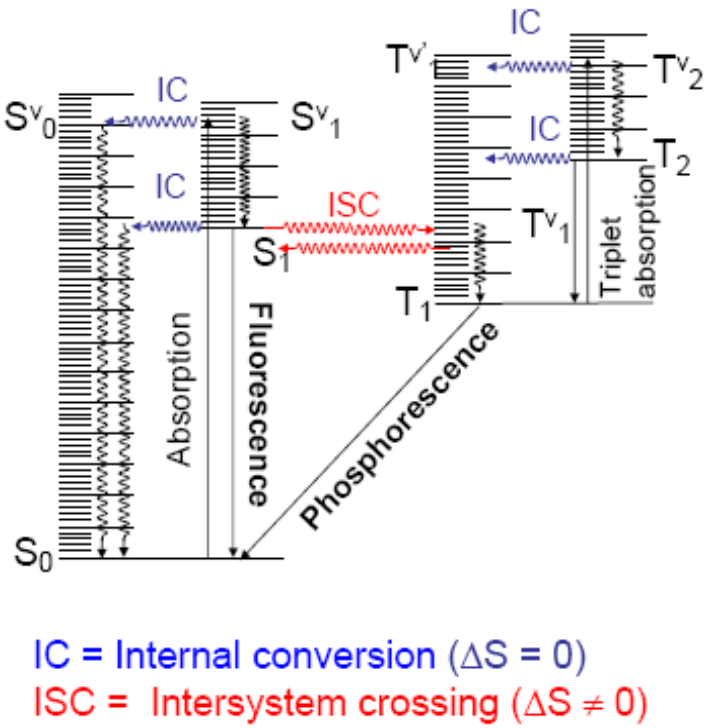

Figure 2.12 Jablonski diagram showing the typical electronic transitions.

Photoluminescence describes the emission of photons from a substance. In particular, a light is directed onto the substance to be tested. The substance absorbs the photons and is imparted the excess photon energy. The excess energy is then dissipated partially through the emission of other photons.

The photons can be emitted through different modes. In the simplest resonant radiation mode, the emitted photon has an equivalent energy to the absorbed photon. The resonant radiation is an extremely fast process (on the order of 10 ns) and does not involve significant internal energy transitions in the substance after the photon absorption. More frequently, the photons are emitted through fluorescence and/or phosphorescence. As schematically illustrated in Jablonski Diagrams (Figure 2.12), before fluorescence emission, the absorbed energy is partially dissipated in the form of thermal heat. The fluorescence emission always occurs at a lower-energy region than the photo-absorption. The fluorescence lifetime is extremely short, typically less than few nanoseconds. In phosphorescence emission, the energy from absorbed photons undergoes intersystem crossing from the singlet excited state (S_1) into the triplet excited state (T_1). The transition back to the lower singlet ground states (S_0) is quantum mechanically forbidden and occurs in a much slower rate than the fluorescence emission. Sometimes the phosphorescence can last minutes or even hours. PL is widely employed for the characterization of semiconducting materials [38, 39, and references therein.], provided that the photon energy ($E = h\nu$) is larger than the band gap (E_g). The PL signals provide valuable structural information of the

substance, such as impurities, defects, and crystalline quality.

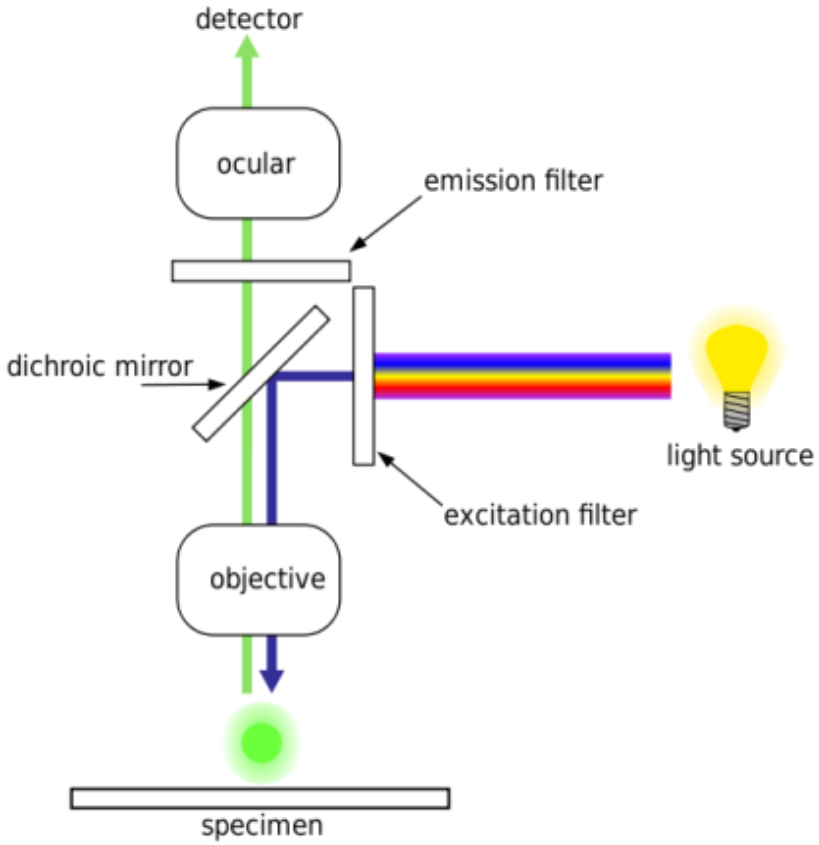

Figure 2.13 Schematic illustration of the fluorescence microscope (FM).

Fluorescence microscope (FM) is an optical microscope (OM), in which a monochromic high-energy light is used as the excitation source and the fluorescence emission from the sample is collected for the purpose of fluorescence imaging. The fluorescence emission occurs at a lower-energy region and is much weaker than the excitation source. As illustrated in Figure 2.13, the fluorescence emission and excitation source go through the same objective. In order to separate the fluorescence emission from the excitation source, an emission filter is employed. Besides the emission filter, the optical components in a FM also include the light source (xenon arc lamp or mercury-vapor lamp), the excitation filter (to

provide monochromic excitation light), and the dichroic mirror (or dichromatic beamsplitter) (see Figure 2.13). The filers and the dichroic mirror are chosen to match the spectral excitation and emission characteristics of the sample. In order to image the samples which do not show spectral excitation and emission characteristics, the fluorephore labeling is widely used especially in the biology field [40-43].

References

1. Yu, H.; Wang, D.; Han, M.-Y. *J. Am. Chem. Soc.* **2007**, *129*, 2333.

2. Wu J. H.; Varghese, B.; Zhou, X. D.; Teo, S. Y.; Sow, C. H.; Ang, S. G.; Xu, G. Q. *Chem. Mater*. **2010,** DOI: *10.1021/cm902490g*

3. Binnig, G.; Quate, C. F.; Gerber, C. *Phys. Rev. Lett.* **1986**, *56*, 930-933.

4. Larson, I.; Drummond, C. J.; Chan, D. Y. C.; Grieser, F. *J. Am. Chem. Soc.* **1993**, *115*, 11885.

5. Xu, L.; Lio, A.; Hu, J.; Ogletree, D. F.; Salmeron, M. *J. Phys. Chem. B* **1998**, *102*, 540.

6. Xiao, X. D.; Qian, L. M. *Langmuir* **2000**, *16*, 8153.

7. Boland, T.; Ratner, B. D. *Proc. Natl. Acad. Sci. USA* **1995**, *92*, 5297.

8. Uchihashi, T.; Sugawara, Y.; Tsukamoto, T.; Ohta, M.; Morita, S.; Suzuki, M. *Phys. Rev. B* **1997**, *56*, 9834.

9. Ong, Y. L.; Razatos, A.; Georgiou, G.; Sharma, M. M. *Langmuir* **1999**, *15*, 2719.

10. Stomp, R.; Miyahara, Y.; Schaer, S.; Sun, Q.; Guo, H.; Grutter, P.; Studenikin,

S.; Poole, P.; Sachrajda, A. *Phys. Rev. Lett.* **2005**, *94*, 056802.

11. Florin, E. L.; Radmacher, M.; Fleck, B.; Gaub, H. E. *Rev. Sci. Instruments* **1994**, *65*, 639.

12. Fu, L.; Liu, X. G.; Zhang, Y.; Dravid, V. P.; Mirkin, C. A. *Nano Lett.* **2003**, *3*, 757.

13. Fischbach, E.; Krause, D. E.; Mostepanenko, V. M.; Novello, M. Phys. Rev. D 2001, 64, 075010.

14. Bonaccurso, E.; Kappl. M.; Butt, H. J. *Curr. Opin. Coll. Inter. Sci.* **2008**, *13*, 107.

15. Wanunu, M.; Popovitz-Biro, R.; Cohen, H.; Vaskevich, A.; Rubinstein, I. *J. Am. Chem. Soc.* **2005**, *127*, 9207-9215.

16. Xu, D. G.; Watt, G. D.; Harb, J. N.; Davis, R. C. *Nano Lett.* **2005**, *5*, 571.

17. Merkel, R.; Nassoy, P.; Leung, A.; Ritchie, K.; Evans, E. *Nature* **1999**, *397*, 50.

18. Rief, M.; Clausen-Schaumann, H.; Gaub, H. E. *Nature Structural Bio.* **1999**, *6*, 346.

19. Demers L. M.; Ginger, D. S.; Park S. -J.; Li, Z.; Chung, S.-W.; Mirkin, C. A. *Science* **2002**, *296*, 1836.

20. Lee, K. -B.; Park, S. –J.; Mirkin, C. A.; Smith, J. C.; Mrksich, M. *Science* **2002**, *295*, 1702.

21. Ginger, D. S.; Zhang, H.; Mirkin, C. A. *Angew. Chem. Int. Ed.* **2004**, *43*, 30.

22. Schitter, G.; Rost, M. J. *Materials Today* **2008**, *11*, 40-48.

23. Lapshin, R. V.; Obyedkov, O. V. *Review of Scientific Instruments* **1993**, *64*,

2883–2887.

24. Lapshin, R. V. *Nanotechnology* **2004**, *15***,** 1135–1151.

25. Lapshin, R. V. *Measurement Science and Technology* **2007**, *18***,** 907–927.

26. Danilatos, G. D. *Advances in Electronics and Electron Physics* **1988**, *71*, 109.

27. Danilatos, G. D. *Microscopy Research and Technique* **1993**, *25*, 354.

28. Savile, B. *An introduction to the optical microscope* New York: Oxford University Press ; Oxford, OX : Royal Microscopical Society, **1984**.

29. Fultz, B.; Howe, J. *Transmission electron microscopy and diffractometry of materials* New York: Springer, **2002**.

30. Kong, X. Y.; Ding, Y.; Yang, R.; Wang, Z. L. *Science* **2004**, *303*, 1348.

31. http://kottan-labs.bgsu.edu/teaching/workshop2001/

32. Tong, Y. H.; Tang, Q. X.; Lemke, H. T.; Moth-Poulsen, K.; Westerlund, F.; Hammershoj, P.; Bechgaard, K.; Hu, W. P.; Bjornholm, T. *Langmuir* **2010**, *26*, 1130.

33. Koo, C. M.; Ham, H. T.; Kim, S. O.; Wang, K. H.; Chung, I. J.; Kim, D. C.; Zin, W. C. *MacroMolecules* **2002**, *13*, 5116.

34. Yang, H.; Coombs, N.; Ozin, G. A. *Nature* **1997**, *386*, 692.

35. Gehringer, L.; Bourgogne, C.; Guillon, D.; Donnio, B. *J. Am. Chem. Soc.* **2004**, *126*, 3856.

36. polarizer: the primary polarizing device which changes the natural incident light into linearly polarized light. Analyzer: the secondary polarizing device placed in the orthogonal position to the polarizer.

37. Olympus, *Basics of polarizing microscopy*.

38. Djurišić, A. B.; Leung, Y. H. *Small* **2006**, *2*, 944.

39. Özgür, Ü.; Alivov, Ya. I.; Liu, C.; Teke, A.; Reshchikov, M. A.; Doğan, S.; Avrutin, V.; Cho, S.-J.; Morkoç, H. *J. Appl. Phys.* **2005**, *98*, 041301.

40. Vazquez, J.; Belmont, A. S.; Sedat, J. W. *Current Biology* **2001**, *16*, 1227.

41. Baksh, M. M.; Jaros, M.; Groves, J. T. *Nature* **2004**, *427*, 139.

42. Henry, R. M.; Hoppe, A. D.; Joshi, N.; Swanson, J. A. *J. Cell Biology* **2004**, *164*, 185.

43. Li, Y. G.; Cu, Y. T. H.; Luo, D. *Nature Biotech.* **2005**, *23*, 885.

Chapter 3

Oriented NaCl Nanocrystals Grown on Mica from Thin Solution Layers: Morphology Transition and Self-assembly

3.1 Introduction

Spontaneous pattern formation in self-assembly is of practical significance and has been extensively studied [1 and references therein.] because of its simplicity and versatility. It may yield structures with newly emerged and/or amplified properties which otherwise are absent in the basic structural units [2, 3]. The basic units used for self-assembly can be small molecules [4, 5], biomacromolecules [6, 7], polymers [8, 9], or even pre-synthesized objects such as nanoparticles, nanorods and nanowires [10-13]. The driving forces for the bottom-up self-assembly can either originate from intermolecular interactions [14-17] or from external factors, such as fluidic, electric, and magnetic fields [18-23], irreversible liquid drying [24-28], etc. In general, the self-assembly driven by short-range intermolecular interactions usually results in patterns with limited spatial scales [29-34]; whereas large-scale self-assembled patterns can be achieved with the assistance of the aforementioned external factors.

In alkali halide group, most members have the NaCl-type crystal structure at room temperature [35]. The epitaxial growth of alkali halides on mica is appealing because it presents robust lattice mismatches through a choice of different alkali halides. A common feature of all these epitaxial alkali halides is that they primarily form oriented triangle-pyramidal islands with the (111) basal planes in contact with the mica (001)

plane. It is known that epitaxial crystallization is largely confined to systems with definite limit of lattice mismatch between the deposit and the substrate. Lamelas *et al.* [36] reported that a larger lattice mismatch between alkali halide and mica led to a lower nucleation density and a narrower condition span for the epitaxial growth. Therefore, it is understandable that previous studies mainly focused on the alkali halides with small lattice mismatches to mica [36-49], such as RbI (0%), KI (-4%), RbBr (-7%) and KBr (-10%). Herein we report the epitaxial growth of oriented NaCl nanocrystals on mica from thin solution layer under a wide variety of ambient humidity. Although the lattice mismatch between NaCl and mica is as large as 23%, oriented epitaxial NaCl nanocrystals have been successfully grown on mica. The condition span for the epitaxial growth was found to be rather wide. At low ambient humidity (dry conditions), the epitaxial NaCl nanocrystals have well-defined triangle-pyramidal shape. At high ambient humidity (wet conditions), the epitaxial triangular pyramids gradually developed into cubic islands, and eventually into long nanowires with a length on the order of millimeters. The morphology transition of the NaCl epitaxial nanocrystals can be attributed to the water adsorption at the surface of the growing NaCl nanocrystals. The oriented NaCl nanocrystals can spontaneously organize into richly patterned, highly ordered arrays with exceptionally large spatial scales (up to ~10 mm^2). The self-assembly of the oriented NaCl nanocrystals was possibly due to the formation of directional high-concentration zones in the evaporating thin solution layers. The NaCl nanocrystal arrays were further employed as templates for patterning thin gold films. The excellent morphology match between the patterned gold films and the original NaCl templates suggests high pattern fidelity.

3.2 Experimental Section

3.2.1 Crystal Growth

NaCl (white crystalline powder, ≥ 99.5%) was purchased from Merck and used as received. NaCl aqueous solution with concentrations in the range of 0.25 – 2 wt% (weight concentration) was prepared by dissolving the NaCl powder in Milli-Q water (Millipore, ≥ 18 $m\Omega.cm^{-1}$). The mica substrates, $KAl_2(Si_3AlO_{10})(OH)_2$, were purchased from Mateck-GmbH. Clean mica surface was prepared by cleavage in the ambient air just prior to each sample preparation.

For crystal growth, a solution droplet (~20 μL) was pipetted onto the freshly cleaved mica surface and then quickly removed by N_2 flow. Such a process resulted in the formation of a thin solution layer on the mica surface, which was subjected to rapid evaporation in N_2 atmosphere. After the N_2 flow was stopped, the mica slice was transferred into a desiccator and incubated for 1~3 hrs. All experiments were carried out at room temperature (RT). The ambient humidity was controlled with the dehumidifiers and recorded with a portable digital hygrothermometer with ± 5% accuracy.

3.2.2 Thin Gold Film Patterning

The as-grown NaCl patterns were used as templates for patterning thin gold films. Two methods were employed, namely peeling-off (Figure 2.2A) and direct-dissolution method (Figure 2.2B). Please refer to Figure 2.2 for the schematic illustration of the patterning process. Steps involved in the peeling-off patterning included: (i) Thin gold film (10 nm thickness) was sputter-coated on the NaCl-covered mica slice. (ii) A drop

of epoxy adhesive was applied onto the top of gold film. (iii) The gold film was peeled off after the epoxy adhesive had been solidified.

In the direct-dissolution patterning, thin gold film (10 nm thickness) was first sputter-coated on the NaCl-covered mica slice. The sample was then immersed in Milli-Q water and ultrasonicated for 5 min. The ultrasonication in Milli-Q water would remove both the NaCl templates and the gold deposited on top of the NaCl templates. However, the gold deposited on the mica surface was well retained. The resulting patterned thin gold film consisted of many discrete and parallel thin gold belts with a uniform thickness of 10 nm (see the later Results & Discussions).

3.2.3 Atomic Force Microscopy (AFM) Characterization.

Morphologies of the oriented NaCl nanocrystals and the patterned thin gold films were examined using Atomic Force Microscopy (AFM, Nanoscope IIIa, Veeco, USA). The AFM operation was carried out under dry ambient conditions (ambient humidity < 35%) in order to avoid any possible deformation of the NaCl nanocrystals by the ambient humidity. AFM images with large scan sizes were collected in tapping mode with a “J” scanner and a silicon tip (force constant: 42 N/m, Nanoworld). The atomic resolution AFM images were achieved in contact mode with an “A” scanner and an oxide-sharpened silicon nitride tip (force constant: 0.12 N/m, Veeco).

3.3 Results

3.3.1 Oriented NaCl Nanocrystals and Mechanism of Morphology Transition

Figure 3.1A shows the NaCl islands grown at 36% (ambient humidity, hereafter all the percent values refer to ambient humidity unless otherwise stated) from a 0.25 wt% thin solution layer. All the NaCl islands are in well-defined triangle-pyramidal shape and oriented in the same direction, consistent to the literature reports [49, 50]. The pointing apexes and three side facets of the triangular pyramids are clearly visible in the phase image (Figure 3.1B). Shown in Figure 3.1C is the three-dimensional (3D) surface plot of a single NaCl triangle-pyramidal island. The standard triangle-pyramidal shape together with the singular orientation of the NaCl islands suggests a possible epitaxial mechanism for the growth of the oriented triangle-pyramidal NaCl islands [49, 50]. The schematic model given in Figure 3.2A shows the atomic arrangement of the uppermost layer of the mica (001) cleaved plane. Upon exposure to solution, K^+ cations at the uppermost layer will enter into the solution, leaving the vacancies (represented by the red dots, Figure 3.2B) available for the Na^+ species in the solution. Figure 3.2B schematically illustrates the epitaxial alignment of the $(111)_{Na}$ plane of NaCl at the mica (001) plane, with a lattice mismatch as large as 23%. The epitaxial orientations are $[11\text{-}2]_{NaCl}$ // $[010]_{mica}$ and $[1\text{-}10]_{NaCl}$ // $[100]_{mica}$. The (100) plane of NaCl crystals has low surface energy and is more stable than the $(111)_{Na}$ and/or $(111)_{Cl}$ planes [60]. The triangular pyramid with three stable (100) side planes has the lowest surface energy. Therefore, the epitaxial NaCl nanocrystals with $(111)_{Na}$ basal plane grow into the triangle-pyramid shape.

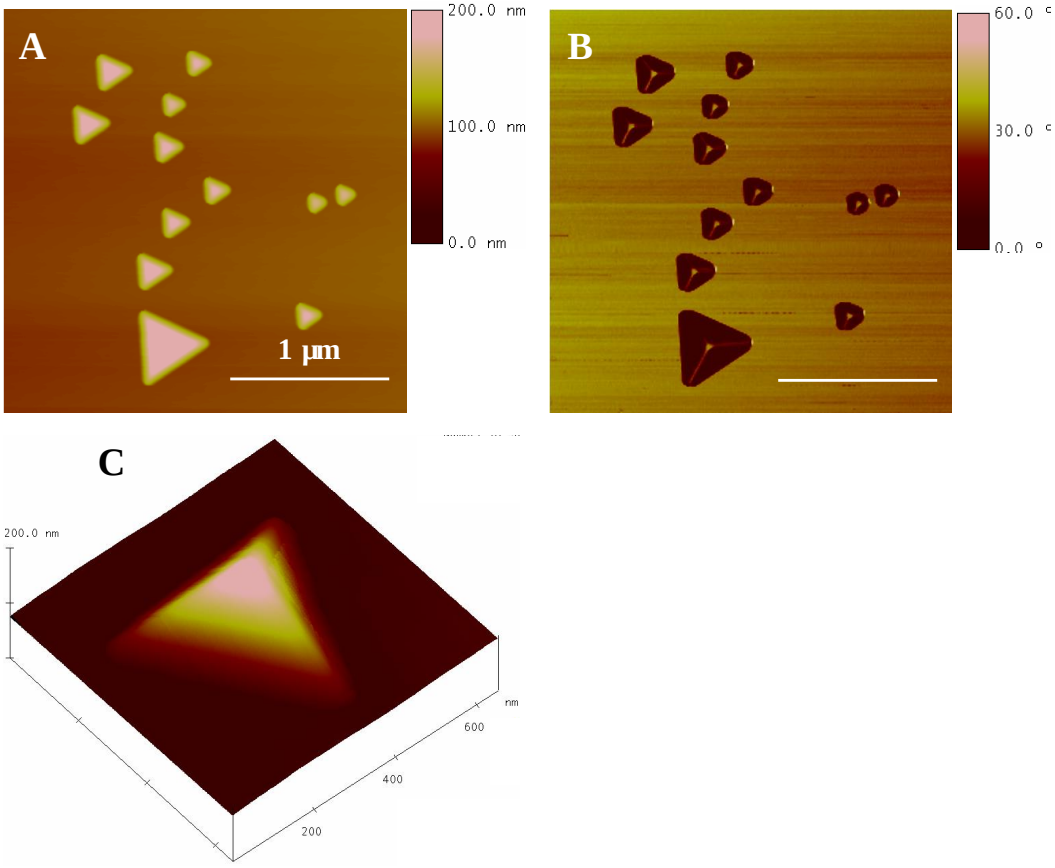

Figure 3.1 Oriented NaCl triangle-pyramidal islands grown at the ambient humidity of 36% from a 0.25 wt% thin solution layer. (A) AFM height image, (B) AFM phase image, and (C) 3D surface plot of a single NaCl triangle-pyramidal island. The scale bars represent 1 µm.

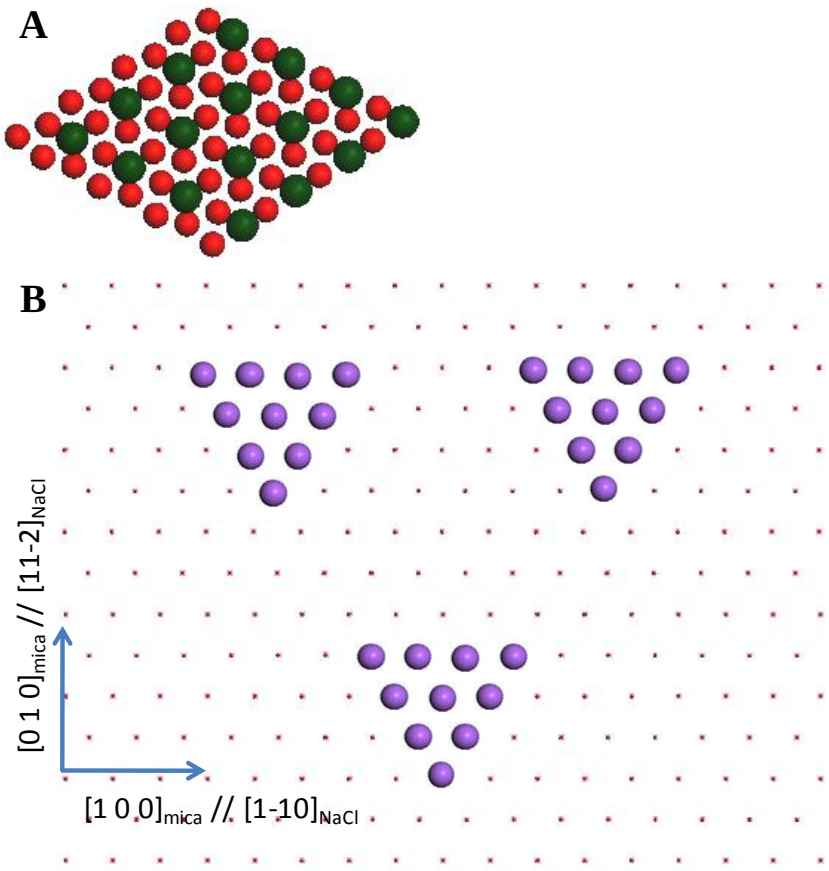

Figure 3.2 (A) Atomic arrangement of the uppermost layer of the mica (001) cleaved plane. (B) Schematic model illustrating the epitaxial alignment of the (111) basal plane of the NaCl islands at the mica (001) cleaved plane. Red, green, and purple balls represent O, K and Na atoms, respectively.

Figure 3.3 shows that quasi-cubic NaCl islands, instead of triangular-pyramidal islands, were grown at a higher ambient humidity of 56% from a 0.25 wt% thin solution layer. All the quasi-cubic islands are oriented in the same direction, suggesting that their growth may also be governed by the same epitaxial mechanism. It is known that crystallization includes two major steps: primary nucleation and subsequent crystal growth. The quasi-cubic islands suggest that morphology transition (triangle-pyramidal islands → cubic islands) may have occurred during crystal growth under the high-humidity condition.

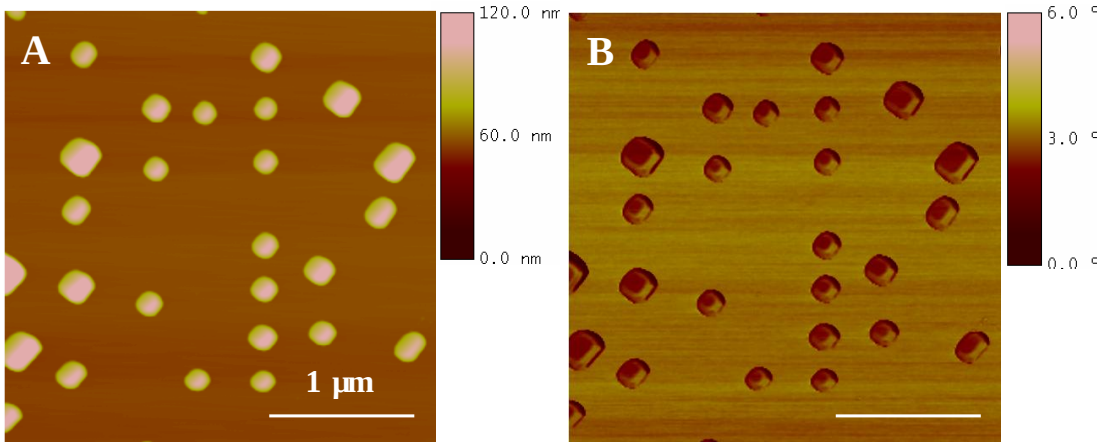

Figure 3.3 Oriented NaCl cubic islands grown at the ambient humidity of 56% from a 0.25 wt% thin solution layer. (A) AFM height image, and (B) AFM phase image. The scale bars represent 1 μm.

For better understanding of the morphology transition, the ambient humidity was increased slowly and the NaCl islands grown at different ambient humidities were characterized carefully using AFM. The results are shown in Figure 3.4. Figure 3.4A shows the NaCl islands grown at the ambient humidity of 42%. Compared to the triangle-pyramidal island grown at the ambient humidity of 36%, it is slightly elongated (denoted by the arrow). The original pointing apex was replaced by a small triangular terrace (denoted by the triangular frame). Nevertheless, the three side facets are still clearly visible in the AFM phase image. Different from the triangle-pyramidal islands with three obvious triangular side facets, the NaCl islands grown at the ambient humidity of 52% has a large rectangular, oblique side facet (as shown in Figure 3.4B). Its basal plane is not in the standard triangular form because one of the basal edges slightly expanded outward. Eventually, a new corner (the forth corner, α) was developed at the middle of the expanding edge. In addition, one of its basal corners (the bottom-left corner, Figure 3.4B) has grown up into an almost-90-degree corner,

different from the 60-degree basal corners of the standard triangular pyramids. Figure 3.4C shows the quasi-cubic NaCl islands grown at the ambient humidity of 56%. Comparing the NaCl islands grown at the ambient humidities of 52% and 56%, it is clear that a slight increase in the ambient humidity has induced significant morphology transition. The initially oblique, rectangular side facet has developed into an almost flat rectangular top facet. The newly appeared basal corner (α) has been fully developed and all the four basal corners now have grown up into almost-90-degree ones. Finally, standard cubic islands were obtained at the ambient humidity of 58% as shown in Figure 3.4D.

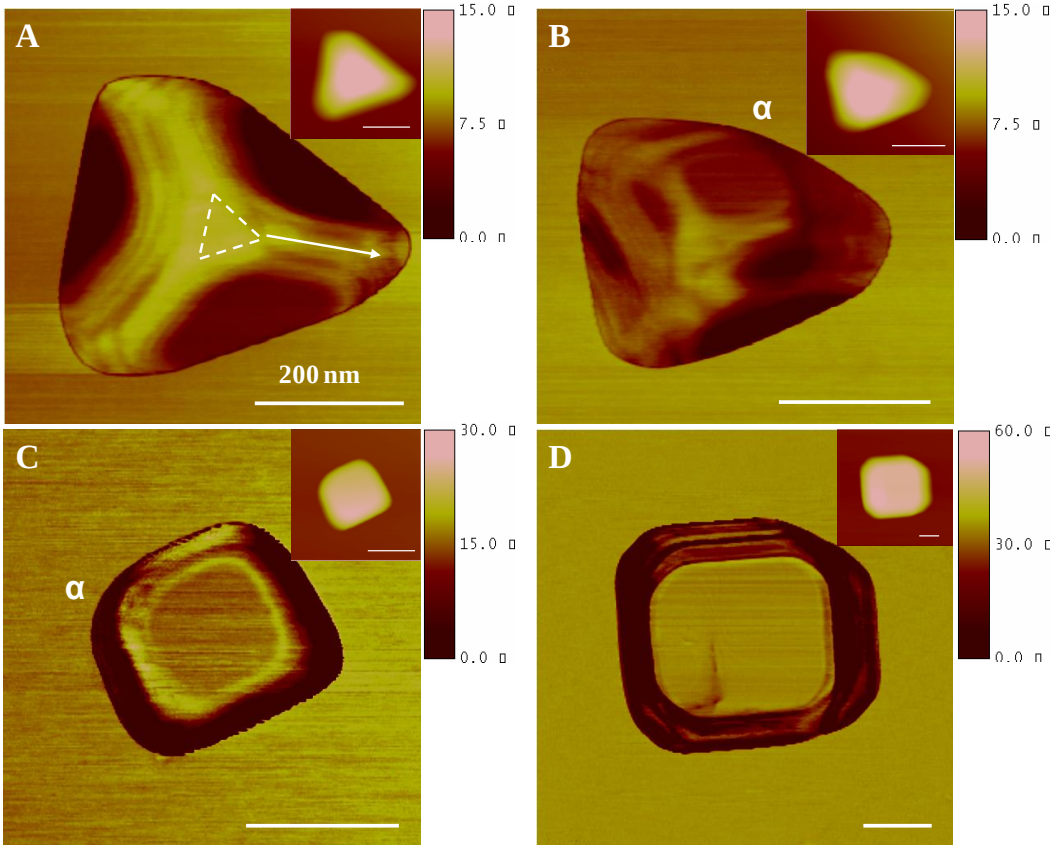

Figure 3.4 AFM phase images showing the NaCl islands grown at the ambient humidity of (A) 42%, (B) 52%, (C) 56%, and (d) 58%. The inset images are the corresponding AFM height images. The concentration in all cases is 0.25 wt%. The scale bars represent 200 nm.

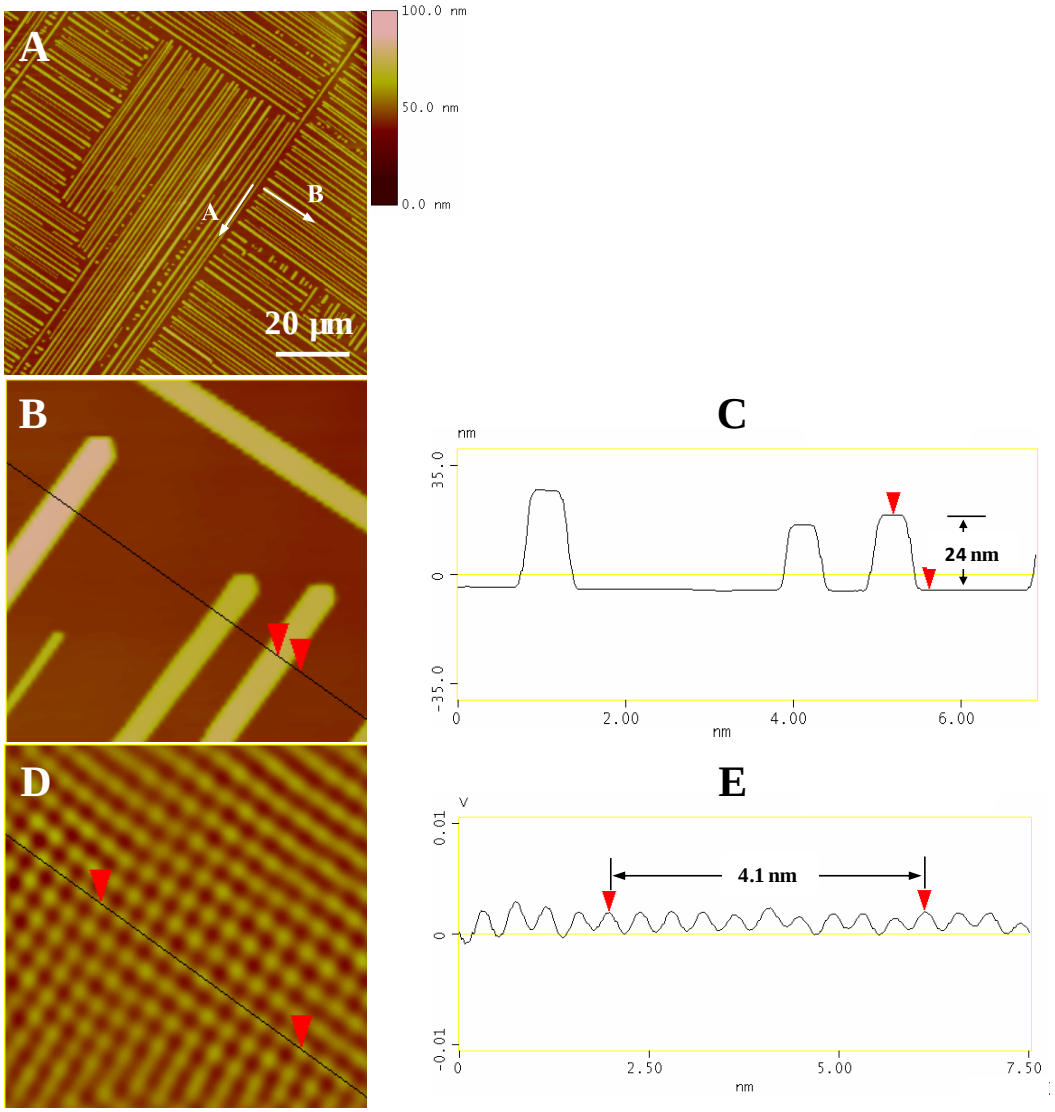

Figure 3.5 (A) Long NaCl nanowires grown at the ambient humidity of 72% from a 0.5 wt% thin solution layer. (B) Close-up view of the orthogonal ends of the long NaCl nanowires. (C) Cross section profile of (B). (D) Fourier filtered atomic resolution AFM deflection image of the top surface of the NaCl nanowires, showing fourfold symmetry and periodicity of ~0.41 nm. (E) Cross section profile of (D) showing a periodicity of ~0.41 nm.

At an even higher ambient humidity of 72%, as shown in Figure 3.5A, exceptionally long NaCl nanowires were obtained from a 0.5 wt% thin solution layer. The NaCl nanowires are exclusively oriented in two perpendicular directions. The perpendicular nanowires are rarely seen to run into each other as the nanowire growth

stops whenever two perpendicular nanowires are running close to each other, suggesting possible screening effect during crystal growth. The NaCl nanowires have a length on the order of millimeters, an approximate width of 1 μm, and an approximate height of 25 nm. The orthogonal ends, as disclosed by the close-up view (Figure 3.5B), suggest that the NaCl nanowires might be (100) oriented. The atomic resolution AFM deflection image exhibits a regular array of protrusions with fourfold symmetry and periodicity of ~0.41 nm (Figure 3.5C), further confirming the (100) orientation.

Note that the NaCl nanowires shown in Figure 3.5 are identical to each other in two perpendicular directions (A- and B-Directions), i.e., the nanowire density and length are almost the same in both directions. We call this a homogeneous growth of the NaCl nanowires. The growth of NaCl nanowires was then investigated as a function of the synthesis conditions, such as the NaCl concentration and the ambient humidity. Figure 3.6A shows that at the ambient humidity of 67%, a large quantity of NaCl nanowires were grown in A-Direction from the same 0.5 wt% thin solution layer; whereas only a few NaCl nanowires were grown in B-Direction. In addition, the NaCl nanowires oriented in A-Direction are much shorter than that in B-Direction. We call this an inhomogeneous growth of the NaCl nanowires. Similar inhomogeneous growth of the NaCl nanowires can also be observed at the same ambient humidity of 72% when the NaCl concentration was increased to 1 wt% (Figure 3.6B). The NaCl nanowires grown at the ambient humidity of 72% from a 2 wt% thin solution layer are oriented in the same direction, as shown in Figure 3.6C. It suggests that the growth of NaCl nanowires in the other perpendicular direction has been completely suppressed. The conditions for the homogeneous and inhomogeneous growth of NaCl nanowires

are summarized in Table 3.1 and 3.2. It can be seen that the transition from homogeneous to inhomogeneous growth can be induced either by a decrease in the ambient humidity or by an increase in the NaCl concentration. It is known that decreasing the ambient humidity would cause a faster solvent evaporation and thus a higher supersaturation level in the evaporating solution layer. The higher supersaturation level in turn would result in a higher nucleation density on the mica substrate. Similarly, the increased NaCl concentration would also induce a higher nucleation density on the mica substrate. It implies that a low nucleation density favors for the homogeneous growth of the NaCl nanowires; whereas a high nucleation density favors for the inhomogeneous growth of the NaCl nanowires.

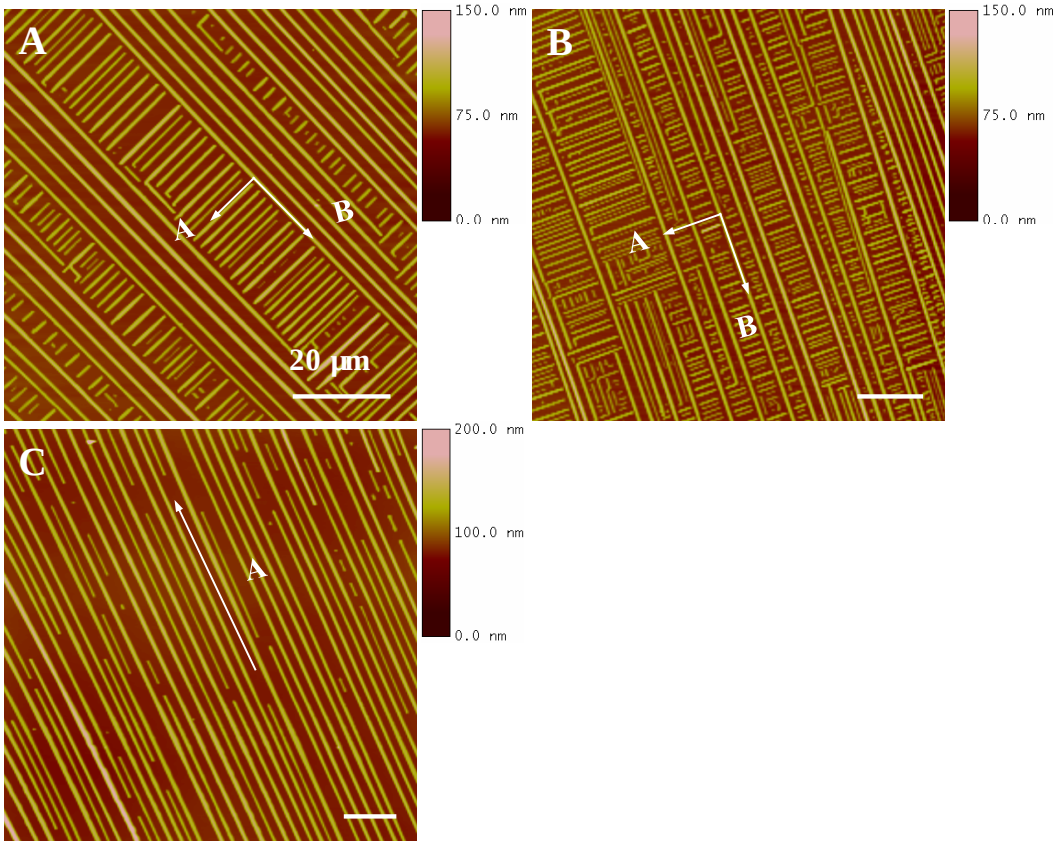

Figure 3.6 Long NaCl nanowires grown at: (A) concentration = 0.5 wt%, RH = 67%; (B) concentration = 1 wt%, RH = 72%; and (C) concentration = 2 wt%, RH = 72%. Note: RH is the relative ambient humidity. The scale bars represent 20 µm.

Table 3.1 NaCl concentrations for the homogeneous and inhomogeneous growth of long NaCl nanowires. See the text for the details.

	Homogeneous Growth	Inhomogeneous Growth	
Concentration (wt.%)	0.5	1	2

Table 3.2 Ambient humidities for the homogeneous and inhomogeneous growth of long NaCl nanowires. See the text for the details.

	Homogeneous Growth	Inhomogeneous Growth
Ambient Humidity (%)	67	72

The morphology transition of the epitaxial NaCl nanocrystals can be understood as follows. It is known that two major steps are involved in the NaCl-on-mica epitaxial crystallization: primary epitaxial nucleation at the solution-mica interface and subsequent crystal growth in the evaporating thin solution layer. At the very beginning, triangle-pyramidal nanocrystals were formed upon the NaCl-on-mica epitaxial nucleation. The concentration field was established with a highest concentration at the corners of the triangle-pyramidal islands but a lowest concentration at the centers of their side facets [52]. At low ambient humidity, a series of events occurred successively: (1) the solvent (i.e. water) was evaporated rapidly; (2) a high supersaturation level was established in the evaporating solution layer due to the fast solvent evaporation; (3) the high supersaturation level in turn induced a high nucleation density of the NaCl epitaxial nanocrystals; and (4) since the supply of NaCl solute was finite in the thin solution layer, a higher nucleation density resulted in smaller sizes of NaCl nanocrystals. The small NaCl nanocrystals can keep their triangle-pyramidal shape during growth as the inhomogeneity in the concentration can

be compensated by the variation in the kinetic coefficient [53], i.e. the lower step density near the corners of the small nanocrystals and the higher step density at the facet centers ensure the uniform growth rate over the entire surface of the small growing nanocrystals. At high ambient humidity, the solvent evaporation was much slower compared to that at the low ambient humidity. Consequently, the nucleation density was low and the average size of the NaCl nanocrystals was large. It is not possible to keep the growth rate uniform all over the surface of a large growing crystal. The growth at the corners was fast since a highest concentration has been established at the corners. The as-grown NaCl islands were slightly elongated as elucidated in Figure 3.4A. As the evaporation and crystal growth going on, the evaporating solution layer was getting thinner while the triangle-pyramidal islands were growing larger. The pointing apexes of the triangle-pyramidal islands would be exposed to the ambient air as long as the evaporating solution layer was getting thinner than the growing NaCl islands. The water vapor from the ambient air was then adsorbed immediately at the exposed apexes [54-58]. It was reported that water adsorption can cause solvation at the NaCl surface [59]. At low ambient humidity (< 40%), the adsorbed water only induces the solvation of the cations (Na^+) [59]. The solvated cations are preferentially accumulated at the steps. The changes caused by water adsorption are reversible upon drying under the low-humidity condition. At high ambient humidities (> 40%), however, the adsorbed water induces the solvation of both ionic species (Na^+ and Cl^-). The highly mobile solvated ions would leave the pointing apexes, running down along one of the three oblique side facets and finally re-entering into the evaporating solution layer at the middle site of the basal edge. It would give rise to two major consequences.

Firstly, the triangular-pyramidal islands would be truncated due to the loss of the solvated ions at the apexes. Theoretically, the height of the NaCl islands would keep equivalent to the thickness of the evaporating solution layer provided that the solvation phenomenon is significant enough at high ambient humidity. Secondly, the ionic concentration in the evaporating solution layer would be largely increased, attributed to the re-entering of the solvated ions. The increased concentration greatly facilitated the continuous growth of the NaCl islands at the basement, especially at the middle site of the basal edge where the solvated ions re-entered into the evaporating solution layer. Thus, the overall morphology transition can be described as an ion relocation process, in which the ions at the exposed apexes were relocated to the growing basement of the NaCl islands. In general, the higher the ambient humidity is, the more significant the ion relocation process would be. This explains why a more dramatic morphology transition was observed at high ambient humidity as elucidated in Figure 3.4. The triangle-pyramidal islands finally developed into cubic islands under high-humidity condition because the cubic NaCl terminated with large (100) facets has the lowest surface energy [60]. On the other hand, the growth at the NaCl islands basement also largely decreased the distance gap between the discrete NaCl islands. As schematically illustrated in Figure 3.7A, while the NaCl islands were getting thinner (with a smaller height “h”), they became closer to each other (with a smaller distance gap “d”) or even coalesced to each other to form continuous long nanowires. The partially coalescent NaCl islands, i.e., the intermediate state between the discrete islands and the continuous long nanowires, are shown in Figure 3.7B. The AFM data given in Figure 3.7C-D shows that the continuous long nanowires on average are only

about ¼ in height compared to the discrete islands, strongly supporting the validity of the coalescence mechanism.

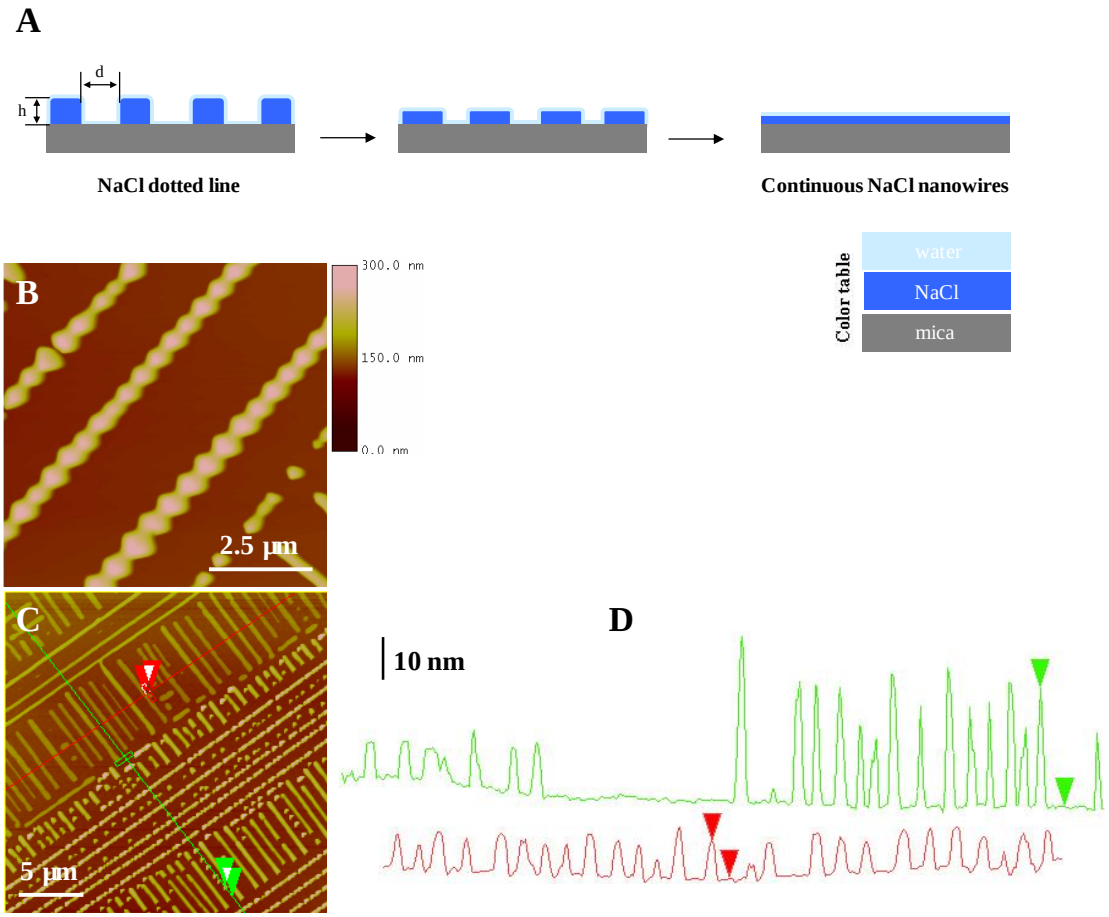

Figure 3.7 (A) Schematic model illustrating the coalescence of discrete islands into continuous long nanowires. (B) Partially coalescent NaCl islands grown at the ambient humidity of 68% from a 2 wt% thin solution layer. (C) NaCl discrete islands together with continuous nanowires grown at the ambient humidity of 58% from a 0.25 wt% thin solution layer. (D) Cross section profile of (C): the mean height of the continuous nanowires (as shown in the below red curve) is only about ¼ of that of the discrete islands (as shown in the above green curve).

3.3.2 Self-Assembly of Disrect NaCl Islands

Figure 3.8 shows that the oriented NaCl islands were self-assembled into long dashed lines. These dashed lines further organized into long-range ordered arrays, in

which they were either parallel to each other or form an angle between each other (hereafter it would be referred as "orientation angle"). The orientation angle is largely dependent on the ambient humidity at which the NaCl islands were grown. As shown in Figure 3.8A, the orientation angle was 60 ° at the ambient humidity of 42%. It gradually grew up into 82 ° and 90 ° at the ambient humidities of 52% (Figure 3.8B) and 56% (Figure 3.8C), respectively.

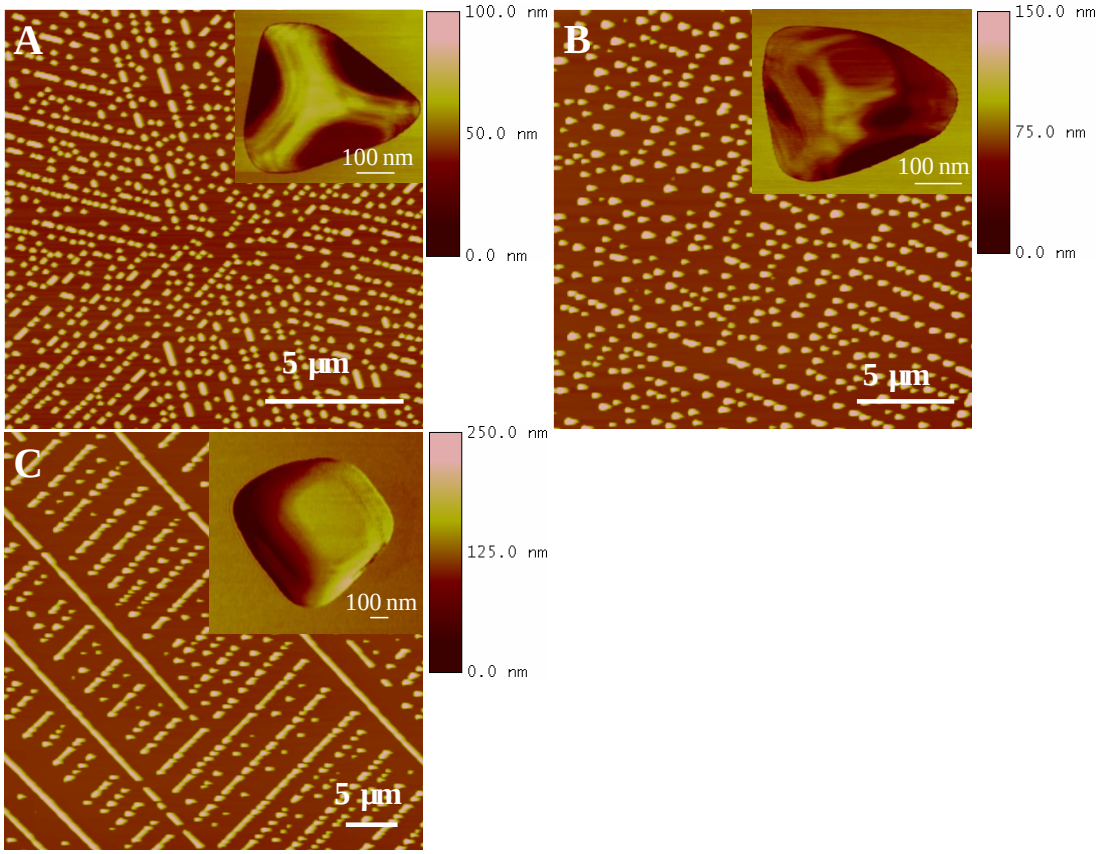

Figure 3.8 Long-range ordered arrays of the oriented NaCl islands (A) with an orientation angle of 60 °, grown at the ambient humidity of 42%, (B) with an orientation angle of 82 °, grown at the ambient humidity of 52%, and (C) with an orientation angle of 90 °, grown at the ambient humidity of 56%. The inset is the close-up view of single NaCl islands. The concentration in all cases is 0.25 wt%. The scale bars represent 5 µm.

The self-assembly of the oriented NaCl islands can be understood as following. As mentioned above, the concentration field establishes a highest concentration at the corners of the NaCl islands but a lowest concentration at the centers of the side facets. Such an inhomogeneous concentration distribution together with the singular orientation of the NaCl epitaxial islands may induce the formation of inhomogeneous concentration distribution in the evaporating thin solution layer. The high-concentration zones would be directed along the oriented corners of the epitaxial islands. In particular, when the NaCl islands are in well-defined triangle-pyramidal shape at low ambient humidity, the high-concentration zones are oriented in directions at 60 º to each other as schematically illustrated in Figure 3.9A. Once the high-concentration zones are established in the thin solution layer, it would exert significant impact on the secondary nucleation events. It is understandable that the secondary nucleation events would be mainly restricted in the high-concentration zones. Typical Oswald ripening would occur simultaneously. The primary NaCl islands located beyond the high-concentration zones would be dissolved as a sacrifice of the crystal growth in the high-concentration zones. Consequently, it would result in the formation long-range ordered arrays with an orientation angle of 60 °. As the ambient humidity increased, the triangle-pyramidal islands with 60-degree corners gradually grow up to the cubic islands with 90-degree corners. The distribution of the high-concentration zones in the evaporating solution layer are re-directed along two perpendicular directions as schematically illustrated in Figure 3.9B, resulting in the long-range ordered arrays with an orientation angle of 90 °. A similar consideration can also be applied to the cases when the NaCl islands are in the intermediate shape

between the triangle-pyramidal and the cubic shapes. The resulting long-range ordered arrays will have an orientation angle between 60 ° and 90 °.

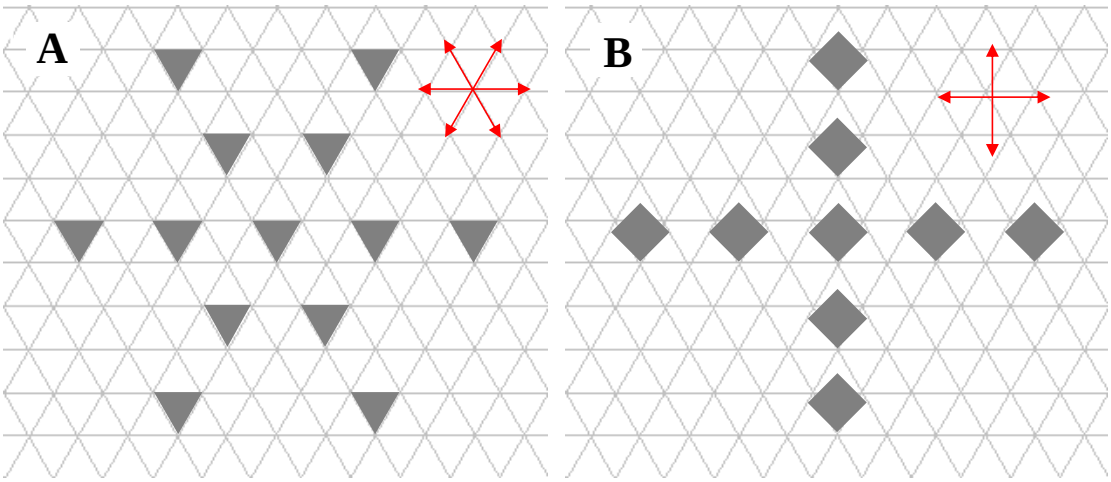

Figure 3.9 Schematic model illustrating (A) the formation of long-rang ordered arrays of oriented NaCl triangle-pyramidal islands with an orientation angle of 60 °, grown at low ambient humidity; and (B) the formation of long-rang ordered arrays of oriented NaCl cubic islands with an orientation angle of 90 °, grown at a high ambient humidity. The network represents the pseudohexagonally arranged potassium ion framework in the mica surface.

3.3.3 Patterned Thin Gold Film

Here we demonstrate that the oriented NaCl long nanowires can be employed as templates for patterning thin gold films. Two advantages of the NaCl-on-mica system are taken into consideration: (i) the mica cleavage surface is atomically flat; (ii) the NaCl templates can be easily removed by water dissolution.

Figure 3.10 shows the patterned thin gold film prepared by the peeling-off method. The periodic nanotrenches in the patterned gold films have a depth and width equal to the NaCl templates. The protrusions in the cross section profile (Figure 3.10B) indicate that the applied mechanical forces for peeling off the thin gold film distorted it as well, especially at the edge of the nanotrenches. The patterned thin film has a very smooth

top surface made up of continued gold, as revealed in the close-up view (Figure 3.10C).

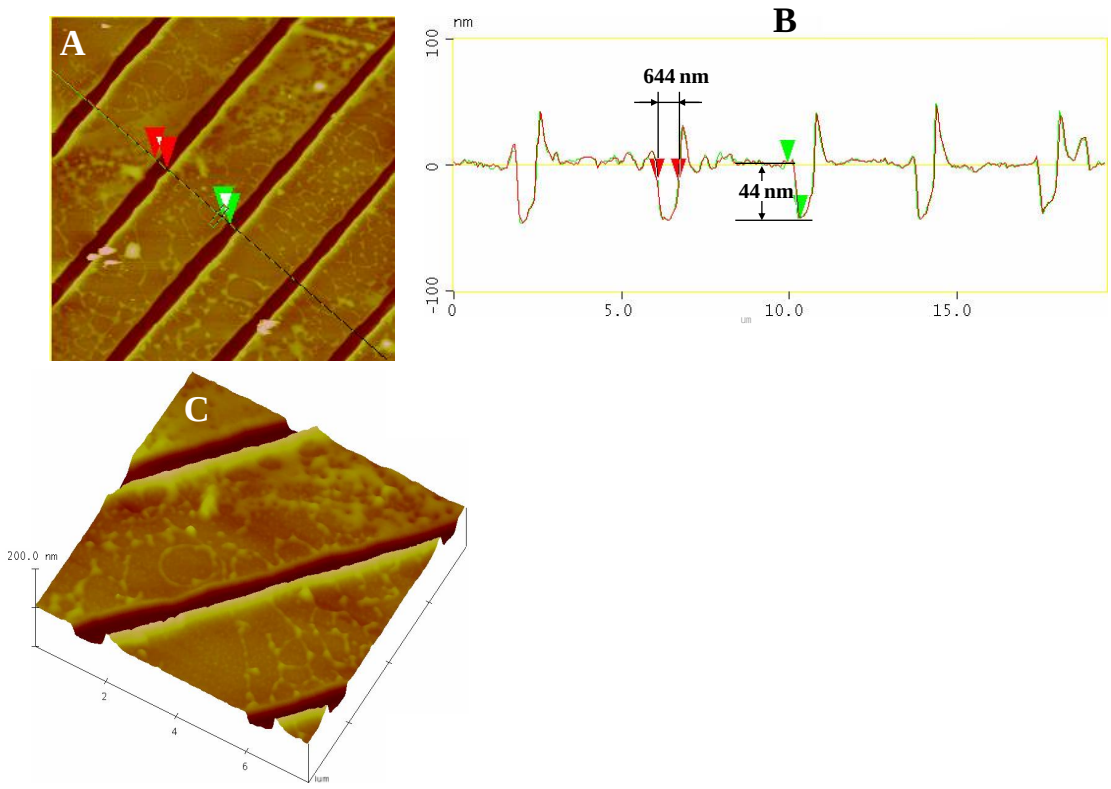

Figure 3.10 (A) Patterned thin gold film prepared by the peeling-off method. (B) Cross section profile and (C) close-up view of the thin gold film shown in (A).

In the direct-dissolution method, the ultrasonication in Milli-Q water removed both the NaCl template and the gold deposited on top of the NaCl template. However, the gold deposited on the mica surface was well retained. The resulting thin gold film is shown in Figures 3.11. Each dissolved NaCl nanowire left one nanotrench in the patterned thin gold film. The nanotrenches have a width equal to the NaCl templates and a uniform depth same to the sputter-coating thickness (10 nm), as shown in Figure 3.11B. The patterned thin gold film consisted of many small gold nanoparticles is not smooth, as disclosed by the close-up view (Figure 3.11C). The bottom of the

nanotrenches is mica but not gold, different from the patterned thin gold film prepared by the peeling-off method.

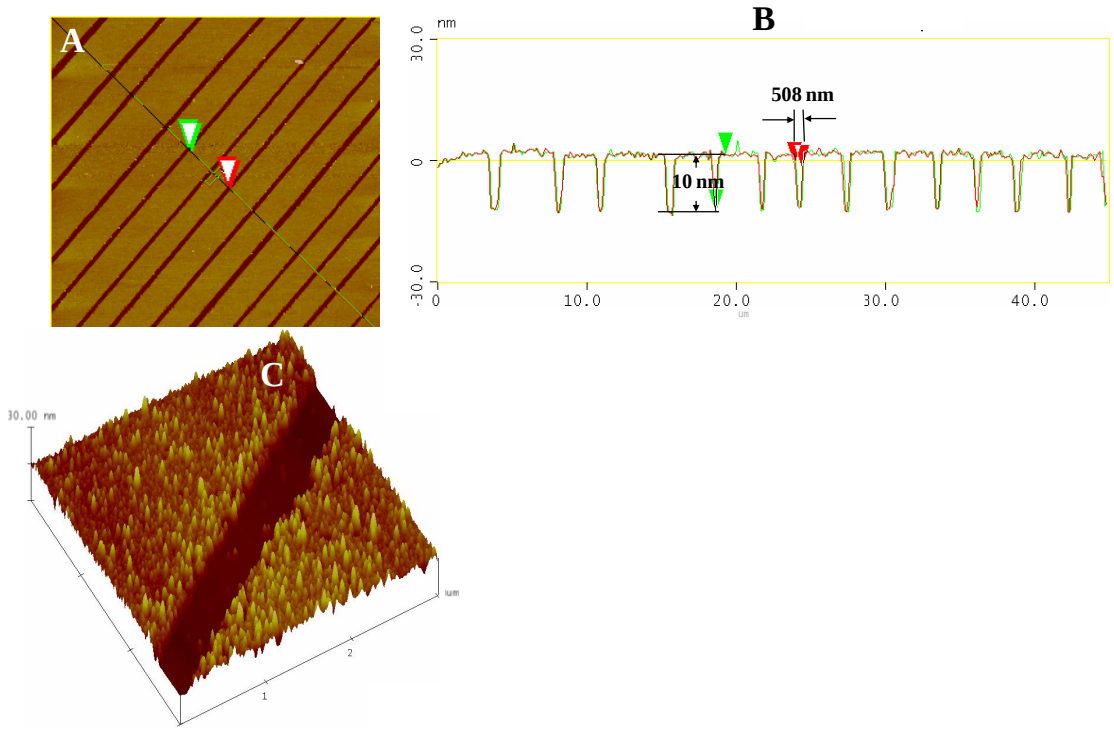

Figure 3.11 (A) Patterned thin gold films prepared by direct-dissolution method. (B) Cross section profile and (C) close-up view of the thin gold film shown in (A).

3.4 Conclusions

In conclusion, we reported a systematic study of the NaCl-on-mica epitaxial crystallization from thin solution layers under a wide range of experimental conditions. Variously shaped NaCl epitaxial nanocrystals were obtained, including the well-defined triangle-pyramidal islands, the cubic islands, and the exceptionally long NaCl nanowires. The morphology transition of the NaCl epitaxial nanocrystals can be attributed to the water adsorption at the surface of the growing NaCl nanocrystals. The oriented NaCl nanocrystals can spontaneously organize into richly patterned arrays

with exceptionally large spatial scales (up to ~10 mm^2). The self-assembly of the oriented NaCl nanocrystals may possibly be due to the formation of directional high-concentration zones in the evaporating thin solution layers. The oriented NaCl long nanowires were further employed as templates for patterning thin gold films. The excellent match between the patterned gold films and the original NaCl templates suggests high pattern fidelity, making it comparable to the photolithographic technique.

References

1. Feyter, S. D.; Schryver, F. C. *Chem. Soc. Rev.* **2003**, *32*, 139.

2. Du, Y.; Han, S.; Jin, W.; Zhou, C.; Levi, A. F. *Appl. Phys. Lett.* **2003**, *83*, 996.

3. Xia Y. *Adv. Mater.* **2001**, *13*, 369.

4. De Feyter, S.; De Schryver, F. C. *J. Phys. Chem. B* **2005**, *109*, 4290.

5. Camillone, N.; Leung, T. Y. B.; Schwartz, P.; Eisenberger, P.; Scoles, G. *Langmuir* **1996**, *12*, 2737.

6. Winfree, E.; Liu, F. R.; Wenzler, L. A.; Seeman, N. C. *Nature* **1998**, *394*, 539.

7. Goetz, R.; Gompper, G.; Lipowsky, R. *Phys. Rev. Lett.* **1999**, *82*, 221.

8. Hanski, S.; Junnila, S.; Almasy, L.; Ruokolainen, J.; Ikkala, O. *Macromolecules* **2008**, *41*, 866.

9 . Jenekhe, S. A.; Chen, X. L. *Science* **1999**, *283*, 372.

10. Mattoussi, H.; Mauro, J. M.; Goldman, E. R.; Anderson, G. P.; Sundar, V. C.; Mikulec, F. V.; Bawendi, M. G. *J. Am. Chem. Soc.* **2000**, *122*, 12142.

11. Yin, Y. D.; Lu, Y.; Gates, B.; Xia, Y. N. *J. Am. Chem. Soc.* **2001**, *123*, 8718.

12. Steiner, D.; Azulay, D.; Aharoni, A.; Salant, A.; Banin, U.; Millo, O. *Nanotech.* **2008**, *19*, 065201.

13. Pacholski, C.; Kornowski, A.; Weller, H. *Angew. Chem. Int. Ed.* **2002**, *41*, 1188.

14. Simard, M.; Su, D.; Wuest, J. D. *J. Am. Chem. Soc.* **1991**, *113*, 4696.

15. MacGillivray, L. R.; Atwood, J. L. *Nature* **1997**, *389*, 469.

16. Müller, M.; Kübel, C.; Müllen, K. *Chem.–Eur. J.* **1998**, *4*, 2099.

17. Weck, M.; Dunn A. R.; Matsumoto, K.; Coates, G. W.; Lobkovsky, E. B.; Grubbs, R. H. *Angew. Chem. Int. Ed.* **1999**, *38*, 2741.

18. Krupke, R.; Hennrich, F.; Weber, H. B.; Kappes, M. M.; Lo¨hneysen, H. V. *Nano Lett.* **2003**, *3*, 1019.

19. Zussman, E.; Theron, A.; Yarin, A. L. *Appl. Phys. Lett.* **2003**, *82*, 973.

20. Messer, B.; Song, J. H.; Yang, P. D. *J. Am. Chem. Soc.* **2000**, *122*, 10232.

21. Huang, Y.; Duan, X. F.; Wei, Q. Q.; Lieber, C. M. *Science* **2001**, *291*, 630.

22. Deng, Z. X.; Mao, C. D. *Nano Lett.* **2003**, *3*, 1545.

23. Grzybowski, B. A.; Stone, H. A.; Whitesides, G. M. *Nature* **2000**, *405*, 1033.

24. Karthaus, O.; Gråsjö, L.; Maruyama, N.; Shimomura, M. *Chaos* **1999**, *9*, 308.

25. Yabu, H.; Shimomura, M. *Adv. Func. Mater.* **2005**, *15*, 575.

26. Hong, S. W.; Xu, J.; Xia, J.; Lin, Z.; Qiu, F.; Yang, Y. *Chem. Mater.* **2005**, *17*, 6223.

27. van Hameren, R.; Schön, P.; van Buul, A. M.; Nolte, R. J. M. *Science* **2006**, *314*, 1433.

28. Hong, S. W.; Xu, J.; Lin, Z. *Nano Lett.* **2006**, *6*, 2949.

29. Zhang, H-M.; Xie, Z-X.; Mao, B-W.; Xu, X. *Chem. Eur. J.* **2004**, *10*, 1415.

30. Feyter, S. D.; Miura, A.; Yao, S.; Chen, Z.; Würthner, F.; Jonkheijm, P.; Schenning, A. P. H. J. E.; Meijer, W.; Schryver, F. C. D. *Nano Lett.*, **2005**, *5*, 77.

31. Kim, K.; Plass, K. E.; Matzger, A. J. *J. Am. Chem. Soc.* **2005**, *127*, 4879.

32. Plass, K. E.; Engle, K. M.; Matzger, A. J. *J. Am. Chem. Soc.* **2007**, *129*, 15211.

33. Feyter, S. D.; Schryver, F. C. D. *J. Phys. Chem. B* **2005**, *109*, 4290.

34. Park, S.; Lee, D. H.; Xu, J.; Kim, B.; Hong, S. W.; Jeong, U.; Xu, T.; Russell, T. P. *Science* **2009**, *323*, 1030.

35. Sirdeshmukh, D. B.; Sirdeshmukh, L.; Subhadra, K. G. *Alkali Halides: A Handbook of Physical Properties;* Springer-Verlag: Berlin, **2001**

36. Lamelas, F. J.; Seader, S.; Zunic, M. *Phys. Rev. B* **2003**, *67*, 045414.

37. Lamelas, F. J.; Schmidt, J. D.; Xiong M. *Phys. Rev. B* **1998**, *58*, 14270.

38. Zouckermann, R. *Proc. European Regional Conf. Electron Microscopy, Delft* **1961**, *1*, 316.

39. Royer, L. *Bull. Soc. franc. Mineral* 1928, *51*, 7.

40. Deicha, G. *C. R. Acad. Sci., Paris* **1946**, *223*, 1155.

41. Deicha, G. *Bull. Soc. franc. Mineral* **1947**, *70*, 177.

42. Deicha, G. *Ibid.* **1947**, *70*, 318.

43. Deicha, G. *Nature* 1949, *164*, 68.

44. Lisgarten, N. D. *Trans. Faraday Soc.* 1954, *50*, 684.

45. West, C. D. *J. Opt. Soc. Amer.* **1945**, *35*, 26.

46. Upreti, M. C.; Walton, A. G. *J. Chem. Phys.* **1966**, *44*, 1936.

47. Kamentsev, I. E. *Kristallografiya* **1956**, *1*, 240.

48. Oles'kiv, S. P.; Freik, D. M. *Neorganicheskie Materialy* **1974**, *10*, 610.

49. Schulz, L. G. *Acta Cryst.***1951**, *4*, 483.

50. Koch, F. A.; Vook, R. W. *Thin Solid Films,* **1972**, *14*, 231.

51. Lomonosov, A. M.; Meshkov G. B.; Yaminsky I. V. *Proceedings of Scanning Probe Microscopy-2004;* Russia: Nizhny Novgorod, **2004.**

52. Berg, W. F. *Proc. Roy. Soc., A* **1937**, *164*, 79.

53. Chernov, A. A. *J. Cryst. Grow.* **1974**, *24-25*, 11.

54. Luna, M.; Rieutord, F.; Melman, N. A.; Dai, Q.; Salmeron, M. *J. Phys. Chem. A* **1998**, *102*, 6793.

55. Park, S. H.; Sposito, G. *Phys. Rev. Lett.* **2002**, *89*, 085501.

56. Arsic, J.; Kaminski, D. M.; Radenovic, N.; Poodt, P.; Graswinckel, W. S.; Cuppen, H. M.; Vlieg, E. *J. Chem. Phys.* **2004**, *120*, 9720.

57. Shindo, H.; Ohashi, M.; Baba, K.; Seo. A. *Surf. Sci.* **1996**, *357-358*, 111.

58. Wassermann, B.; Mirbt, S.; Reif, J.; Zink, J. C.; Matthias, E. *J. Chem. Phys.* **1993**, *98*, 10049.

59. Luna, M.; Rieutord, F.; Melman, N. A.; Dai, Q.; Salmeron, M. *J. Phys. Chem. A* **1998**, *102*, 6793.

60. Tasker, P. W. *Philos. Mag. A* **1979**, *39*, 119.

Chapter 4

Interconnected Networks of $Zn(NO_3)_2.6(H_2O)$ Nanotubes and Its Solid-Phase Transformation into Porous Zinc Oxide Architectures

4.1 Introduction

It is widely recognized that the properties of nanomaterials depend not only on the compositions, crystal structures, sizes and shapes, but also on the way in which they are organized into higher-order hierarchical architectures. ZnO is an important wide band gap semiconducting material with interesting optical, optoelectronic, and piezoelectric properties. The optical properties largely depend on the sizes, shapes, defects, and impurities of ZnO nanostructures [1, 2 and references therein]. To achieve ZnO optical devices, it is important to realize the well-controlled structural properties as well as the light emissions by manipulating the fabrication of ZnO nanostructures. A variety of ZnO nanostructures have been reported, including nanoparticles [3-5], nanorods [6-8], nanowires [9-11], nanobelts [12-14], nanotubes [15-18], core-shell structures [19, 20], and other complex hierarchical structures [21, 22]. ZnO nanotubes, owing to the large surface area and possible quantum-confinement effect, have raised great interests recently [23-27]. A feasible strategy to further increase the surface area and hence to achieve enhanced functionality of ZnO nanotubes is the introduction of pores into their walls. However, such an attribute is rarely explored so far [28, 29]. Current

strategies towards highly porous structures include thermal decomposition [30], chemcial reduction [31], Kirkendall counterdiffusion [32], template-assisted methods [33, 34], etc. The thermal stability of zinc nitrate hexahydrate has drawn wide attentions [35-40]. The releasing of gaseous side products during the thermal decomposition renders a promising way for the preparation of porous ZnO structures.

In the present study, we developed the one-step synthesis of highly oriented, interconnected $Zn(NO_3)_2.6H_2O$ nanotubes on mica and subsequent solid-phase thermal decomposition into porous ZnO architectures. The $Zn(NO_3)_2.6H_2O$ nanotubes with rectangular cross-section were prepared from a thin solution layer governed by an epitaxial growth mechanism. These epitaxial nanotubes were oriented in directions at ~60 ° to each other and self-assembled into macroscopic interconnected hexagonal networks on mica surfaces. It was found that fast evaporation of the solvent was crucial for the formation of high-quality $Zn(NO_3)_2.6H_2O$ rectangular nanotubes. While the overall geometrical configuration of the network-like assemblies was largely retained in the thermal decomposition of $Zn(NO_3)_2.6H_2O$ nanotubes, the resulting porosity could be tailored by varying the annealing temperature and time. The photoluminescence (PL) spectra at room temperature (RT) exhibited a strong dependence on the annealing temperatures, implying that various types of defects were evolved in the porous ZnO architectures prepared at different temperatures. The electrical measurements

demonstrated that the porous ZnO interconnected networks were electrically interconnected as a single integrated unit and exhibited a symmetric, linear current-voltage (*I*-*V*) characteristic.

4.2 Experimental Section

Zinc nitrate hexahydrate crystalline powder (reagent grade, 98%) was purchased from Aldrich and used as received. Solutions with concentrations in the range of 0.025-0.4 M were prepared by dissolving the zinc nitrate hexahydrate powder in Milli-Q water (Millipore, ≥18 $M\Omega.cm^{-1}$). The mica substrate, $KAl_2(Si_3AlO_{10})(OH)_2$, was purchased from Mateck GmbH. Clean mica surfaces were prepared by cleaving the samples in the ambient air just prior to each experiment.

To grow $Zn(NO_3)_2.6H_2O$ rectangular nanotubes, a droplet (~20 μL) of the zinc nitrate hexahydrate solution was pipetted onto a freshly cleaved mica surface and then removed quickly by N_2 flow. Such a process resulted in a thin solution layer on the mica surface, which was then subjected to rapid evaporation in N_2 atmosphere. After the N_2 flow was stopped, the mica slice was transferred into a desiccator and incubated for 1~3 hrs. To prepare porous ZnO architectures, the as-synthesized $Zn(NO_3)_2.6H_2O$ nanotubes were annealed in a furnace (Barnstead Thermolyne, F4800 Furnace) at different temperatures for various lengths of time.

Morphology of the as-synthesized structures was characterized using

scanning electron microscopy (SEM, JEOL JSM-5200), and field-emission SEM (FESEM, JEOL JSM-6701F). The crystallographic and compositional information was obtained using powder X-ray diffraction (XRD, Siemens D5000, operated at 40 kV and 40 mA) with monochromatized Cu Kα radiation (λ = 1.54 Å), energy-dispersive X-ray spectroscopy (EDS, JSM-3010, operated at 300kV), and selected area electron diffraction (SAED, JSM-3010, operated at 300kV). The PL measurements were performed at RT using a He-Cd laser (325 nm) as the excitation source (Renishaw system 2000). The electrical properties were measured at RT in a FESEM chamber (JEOL, JSM7401-F, vacuum $<10^{-4}$ Pa) equipped with nanomanipulators (sProber Nano-M, Zyvex Instruments). The piezo-controlled tungsten nanoprobes have a tip size typically < 50 nm.

4.3 Results and Discussion

4.3.1 Highly Oriented $Zn(NO_3)_2.6H_2O$ Rectangular Nanotubes

Figure 4.1 shows typical SEM images of samples grown from a 0.1 M solution layer evaporated in N_2 atmosphere for ~20 sec. The mica surface was covered with interconnected 1D nanostructures that were oriented in directions at ~60 º to each other. These 1D nanostructures were self-assembled into isolated clusters (Figure 4.1A) or into extended networks (Figure 4.1C). A more careful and close-up view (Figure 4.1D) revealed that most of these 1D nanostructures have open rectangular ends, indicating the hollow tubular structure. When a lower

concentration of 0.025 M was applied, isolated clusters were found to be the major product (Figure 4.2A), whereas extended networks were predominant at the concentration of 0.4 M (Figure 4.2B). The concentration-dependent self-assemblies can be explained as follows. During evaporation, the thin solution layer tends to rupture into small droplets to reduce the total free surface energy [41]. On the other hand, the $Zn(NO_3)_2.6H_2O$ crystals appeared at the mica-solution interface serve as nails that can pin the solution layer against the mica surface and hence hinder it from rupture [42]. At higher concentrations, the thin solution layer becomes saturated soon after the starting of evaporation. The $Zn(NO_3)_2.6H_2O$ crystals emerge at the mica-solution interface before the solution layer ruptures, leading to the formation of large extended networks. In contrast, when a low concentration (0.025 M) was applied, the thin solution layer was found to have ruptured into small isolated droplets before the occurrence of any noticeable crystallization at the mica-solution interface. Consequently, each small droplet developed into one isolated cluster.

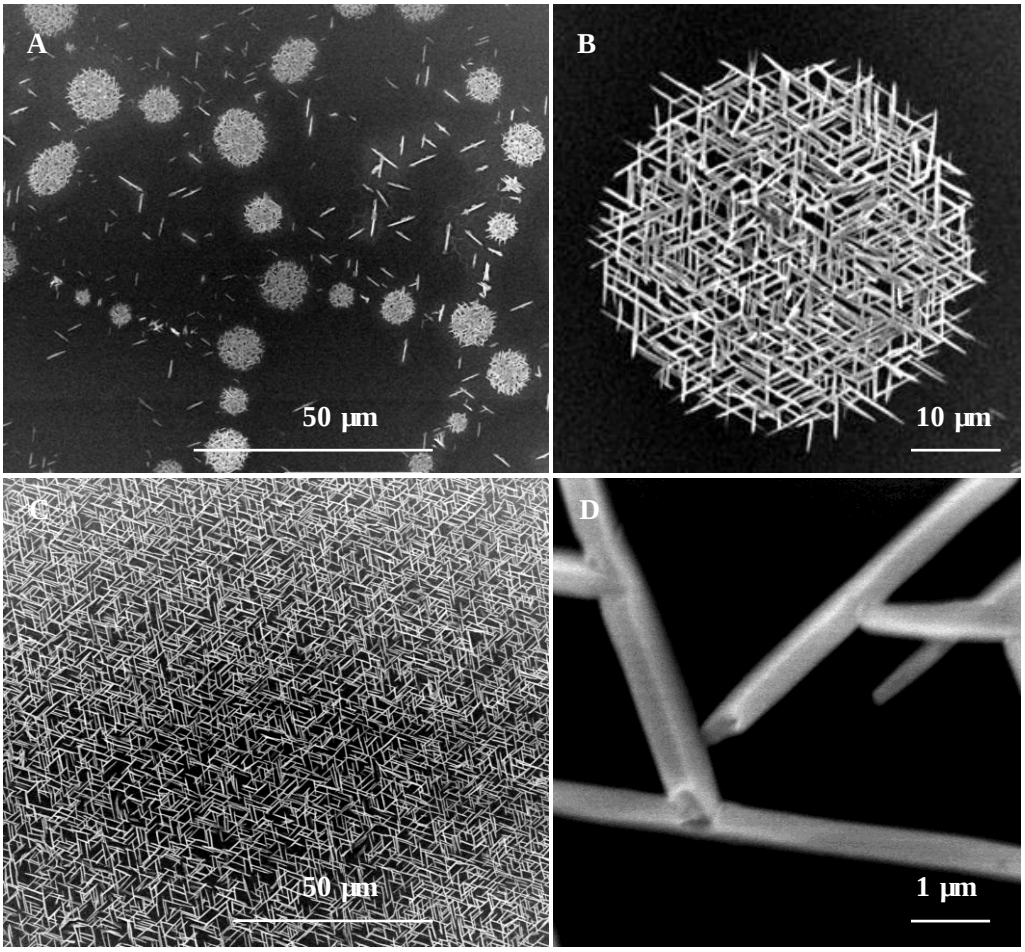

Figure 4.1 Highly oriented, interconnected $Zn(NO_3)_2.6H_2O$ nanotubes on mica substrates, grown from a 0.1 M solution layer evaporated in N_2 atmosphere for ~20 sec. (A) Nanotubes self-assembled in the form of isolated clusters. (B) Close-up view of a single cluster. (C) Nanotubes self-assembled in the form of extended networks. (D) Close-up views of (C).

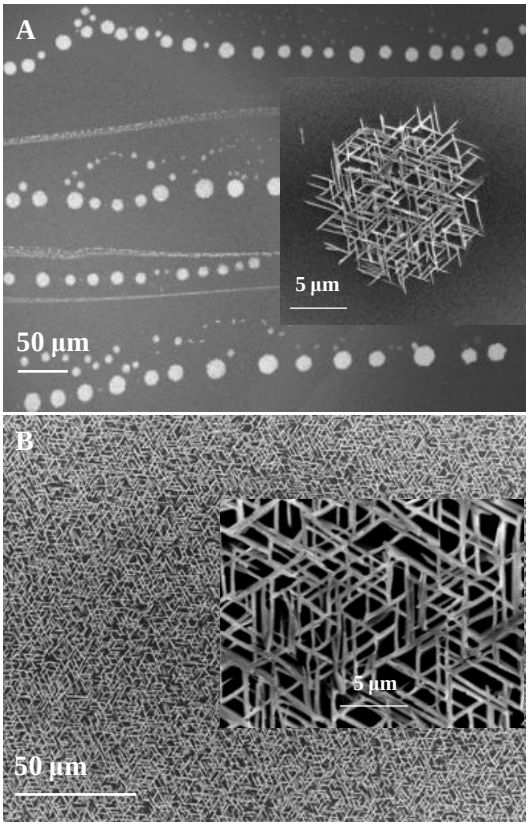

Figure 4.2 Interconnected $Zn(NO_3)_2.6H_2O$ nanotubes (A) self-assembled in the form of isolated clusters, grown from a 0.025 M solution layer. Inset is the close-up view of a single cluster. (B) Self-assembled in the form of extended network, grown from a 0.4 M solution layer. Inset is the close-up view.

Similar experiments were carried out on other substrates, including amorphous glass, Si(100), and highly ordered pyrolytic graphite (HOPG). Tubular crystals with random orientation were obtained on the surfaces of amorphous glass and Si(100) (Figure 4.3). However, no noticeable crystals were obtained on the surface of HOPG. This is attributable to the hydrophobic nature of the HOPG surface. The N_2 flow completely removes the solution droplet from the HOPG surface. This prevents the formation of a thin solution layer on the HOPG surface, which is essential for the growth of $Zn(NO_3)_2.6H_2O$ crystals. The hexagonal patterning on mica suggests a possible epitaxial growth mechanism, which is attributable to the

surface lattice structure and ionic nature of mica. XRD results further suggests that the $Zn(NO_3)_2.6H_2O$ nanotubes have {113} planes parallel to the mica substrate (as will be discussed later). Figures 4.4A-B show the schematic models of the unit cell of orthorhombic $Zn(NO_3)_2.6H_2O$ and its (113) plane, respectively. The atomic arrangement of the uppermost layer of cleaved mica is displayed in Figure 4.4C. Upon exposure to solution, K^+ cations at the uppermost layer will enter into the solution, leaving the vacancies (represented by the red dots in Figure 4.4D) available for the cation species in the solution. Figure 4.4D depicts the epitaxial alignment of $Zn(NO_3)_2.6H_2O$ (113) plane at the cleaved mica surface. The $Zn(H_2O)_6^{2+}$ cations are located either at the vacancy sites or at the bridge sites (the middle sites between two neighboring red dots). The epitaxial orientations are $[010]_{mica} // [1\bar{1}0]_{nitrate}$ and $[100]_{mica} // [21\bar{1}]_{nitrate}$. The lattice mismatches along the directions of $[010]_{mica}$ and $[100]_{mica}$ are calculated to be -1 and 10 %, respectively. The growth of 1D $Zn(NO_3)_2.6H_2O$ nanotubes can be attributed to both its anisotropic orthorhombic structure [43] and the anisotropic lattice mismatches in two perpendicular directions. The nanotubes grow preferentially along the direction of $[010]_{mica}$ or $[1\bar{1}0]_{nitrate}$ (the direction with smaller lattice mismatch), whereas the growth is essentially hindered along the direction of $[100]_{mica}$ or $[21\bar{1}]_{nitrate}$ (the direction with larger lattice mismatch). Owing to the crystal symmetry of mica substrate, preferential growth can also take place along the identical directions of $[2\bar{1}0]_{mica}$ and $[\bar{2}\bar{1}0]_{mica}$. The nanotubes elongate until encountering each other or the

complete depletion of $Zn(NO_3)_2.6H_2O$ in solution, resulting in the formation of interconnected hexagonal networks.

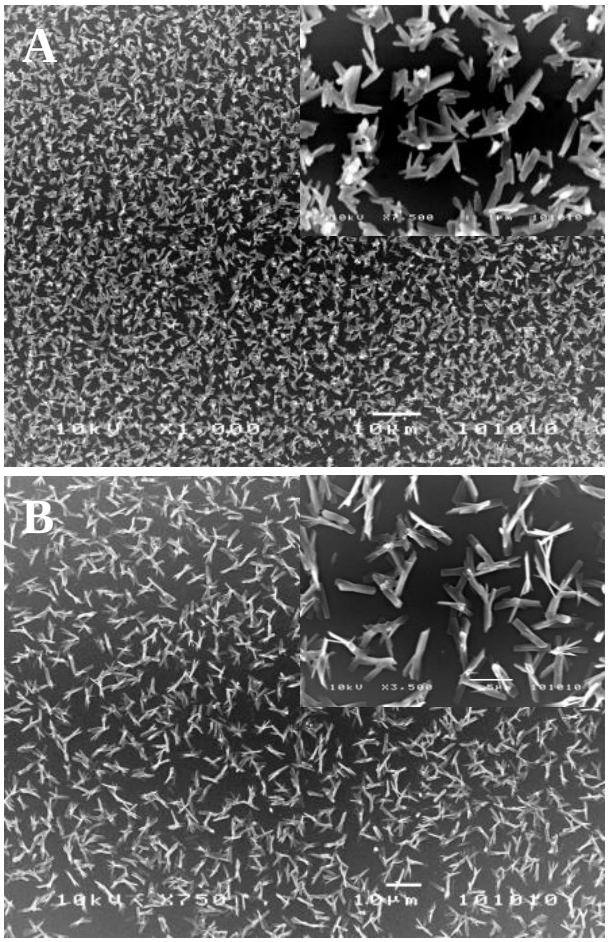

Figure 4.3 $Zn(NO_3)_2.6H_2O$ nanotubes grown (A) on amorphous glass, and (B) on Si (100). The inset is the close observation. In both cases the concentration was 0.4 M.

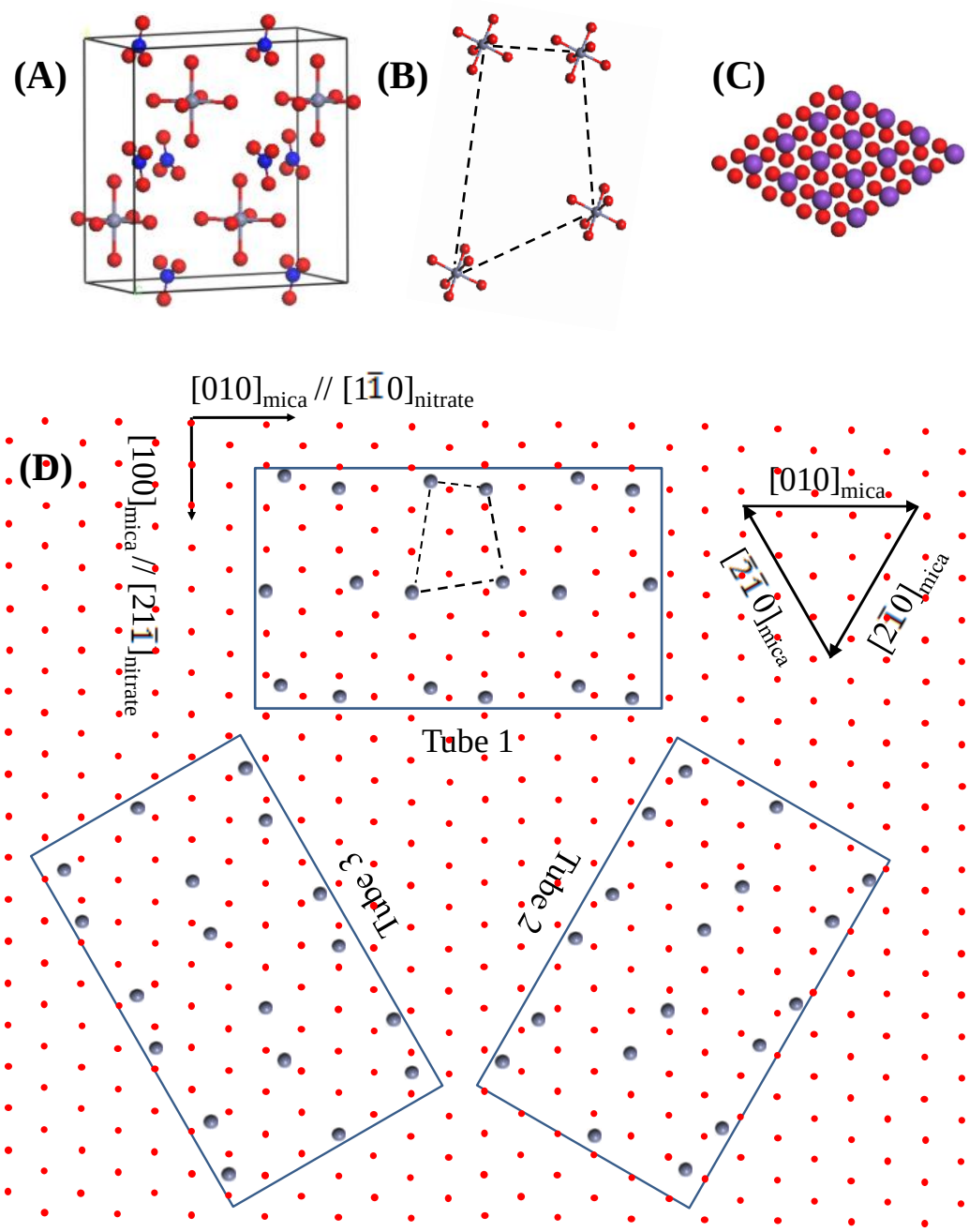

Figure 4.4 (A) Unit cell of orthorhombic $Zn(NO_3)_2.6H_2O$. For clarity, H atoms of the water molecules are not shown. (B) (113) plane of $Zn(NO_3)_2.6H_2O$. For clarity, NO_3^- anions are not shown. (C) Atomic arrangement of the uppermost layer of cleaved mica. (D) Schematical model illustrating the epitaxial alignment of the $Zn(NO_3)_2.6H_2O$ (113) plane at the cleaved mica surface. For clarity, the water molecules coordinated with Zn^{2+} cations are not shown. Blue, red, grey and purple balls represent N, O, Zn and K atoms, respectively.

The N_2-blowing time was found to be crucial for the nanotube growth. When the N_2 flow was cut off immediately after the solution droplet was removed from the mica surface, large thin-walled nanotubes with random orientation together with partially folded-up, randomly-oriented small nanotubes were obtained (Figure 4.5). On the other hand, increasing the N_2-blowing time will yield more oriented small nanotubes (Figure 4.6). Due to large diameters and thin walls, most of the thin-walled nanotubes collapsed (Figure 4.5-4.6). Even though, their tubular structure can still be identified from the upward opening ends (denoted by the arrowheads, Figure 4.6B). The folding-up of these large collapsed nanotubes began either from one end of the large collapsed nanotube (Figure 4.6B, denoted by the arrows), or from its two long sides (Figure 4.6C). The folding-up was more complete with a longer N_2-blowing time (Figure 4.6D-F). As discussed above, the oriented nanobutes were epitaxially grown on the mica substrate. The randomly oriented nanotubes shown in Figure 4.5, however, are nonepitaxial ones that possibly crystallized at the solution-air interface and then deposited on the mica substrate. Some of the nonepitaxial nanotubes were also found to be folded up. Thus, the folding-up behavior may be governed by some reasons other than the lattice-mismatch-induced stress, which typically exists in the epitaxial crystals. Note that the thin solution layer was evaporated in two stages. Firstly, it was rapidly evaporated in N_2 atmosphere. After the N_2 flow was stopped, the remaining solvent would be evaporated slowly in the desiccators. Therefore, a longer

N_2-blowing time would lead to an overall faster crystal growth. The fast-grown nanotubes may have a higher density of crystallographic defects. Stress originating from these defects may also be responsible for the folding-up phenomena. Figure 4.6G schametically illustrates the folding-up process beginning from the long sides of large collapsed nanotubes.

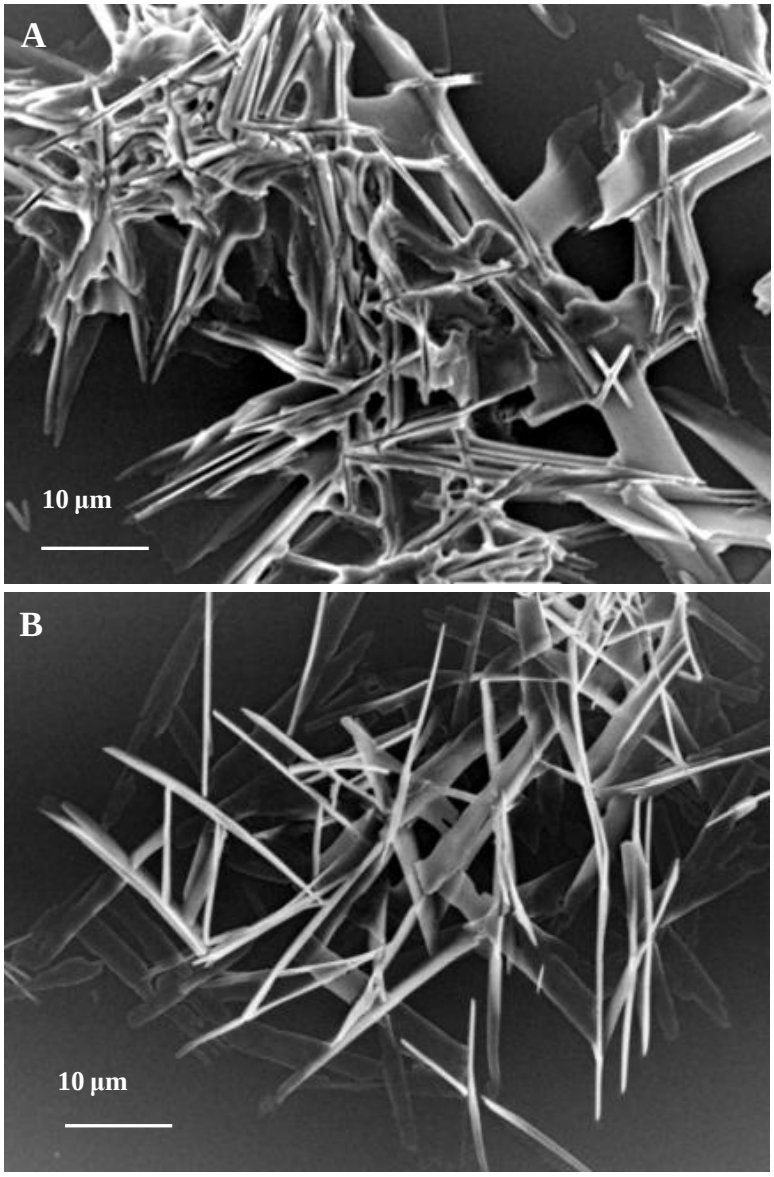

Figure 4.5 Randomly oriented $Zn(NO_3)_2.6H_2O$ nanotubes prepared from a 0.4 M solution layer. The N_2 gas flow was cut off immediately after the solution droplet was blown away from the mica surface.

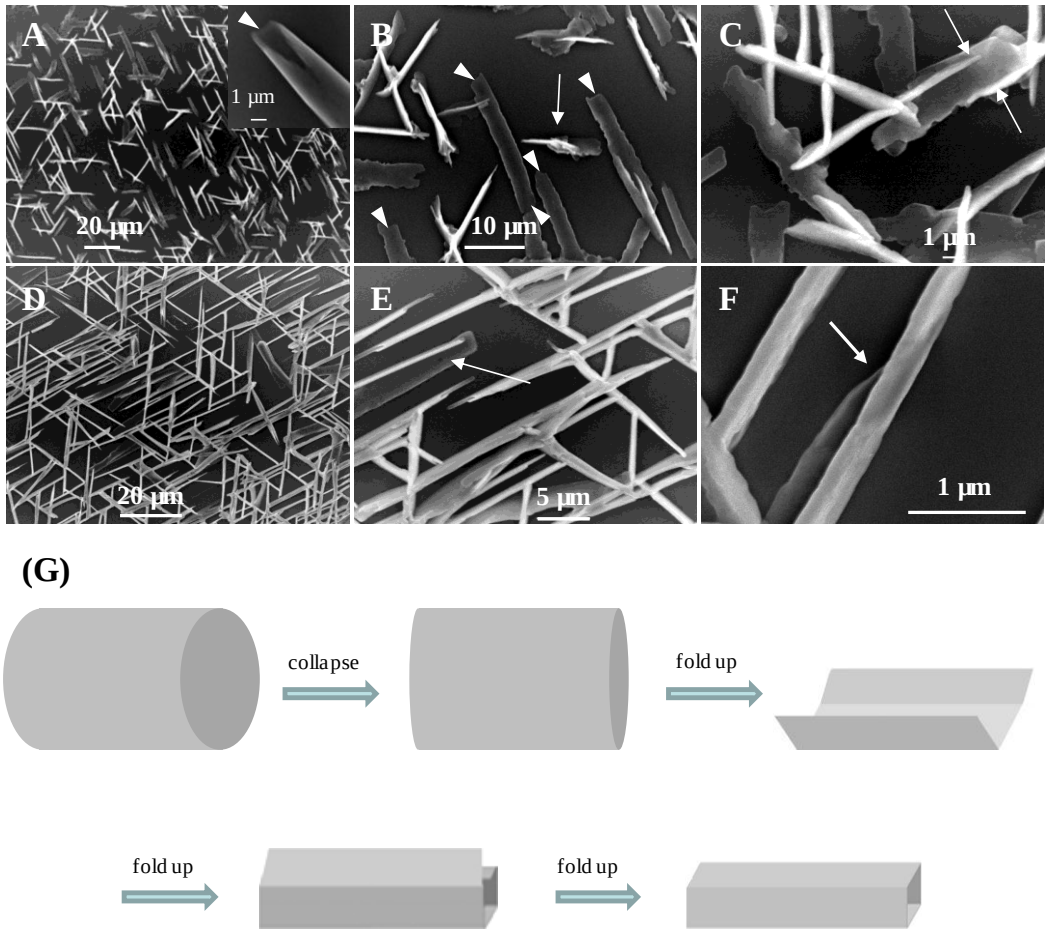

Figure 4.6 $Zn(NO_3)_2.6H_2O$ nanotubes grown from a 0.4 M solution layer evaporated in N_2 atmosphere (A-C) for ~5 sec; and (D-F) for ~10 sec. Inset of (A) shows a large thin-walled nanotubes. (G) Schematic model illustrating the folding-up of large thin-walled nanotube into small rectangular nanotube.

4.3.2 Porous ZnO Architectures

The thermal transformation of $Zn(NO_3)_2.6H_2O$ into ZnO begins at ~40 ℃ [44]. Intermediate hydrates of $Zn(OH)(NO_3).H_2O$ and $Zn_3(OH)_4(NO_3)_2$ as well as gaseous side products of the solid-phase transformation were reported in literature [39, 40]. Curve (i) in Figure 4.7A shows the XRD pattern of bare mica. The $Zn(NO_3)_2.6H_2O$ nanotubes grown on mica substrate presents a strong (113)

reflection at 44.4 °at RT (Curve (ii), Figure 4.7A). The XRD results indicate that the as-synthesized $Zn(NO_3)_2.6H_2O$ nanotubes were single-crystalline and with {113} planes (also the peripheral planes) parallel to the mica substrate. The small peak at 10.87 °can be indexed to the (200) reflection of $Zn(NO_3)(OH).H_2O$ — one of the intermediate hydrates in the thermal decomposition of $Zn(NO_3)_2.6H_2O$ [39]. This indicates that a mild solid-phase transformation of $Zn(NO_3)_2.6H_2O$ nanotubes readily took place at RT. The $Zn(NO_3)_2.6H_2O$ nanotubes were then subjected to thermal annealing at 255 ℃ for various lengths of time. The evolution of XRD patterns were traced and shown in Figure 4.7A. The XRD pattern at 1 hr (Curve (iii)) shows reflections from the intermediate $Zn_3(OH)_4(NO_3)_2$ but with no reflection from $Zn(NO_3)_2.6H_2O$, implying a completed conversion from $Zn(NO_3)_2.6H_2O$ into $Zn_3(OH)_4(NO_3)_2$. The reflections of $Zn_3(OH)_4(NO_3)_2$ vanished at 4 hr (Curve (iv)), indicating the end of thermal decomposition. On the other hand, the ZnO (002) reflection (hexagonal wurtzite, JCPDS card no. 36-1451) started to appear at 4 hr, which was enhanced either by a prolonged annealing at the same temperature (Figure 4.7B) or by annealing at higher temperatures (Figure 4.7C).

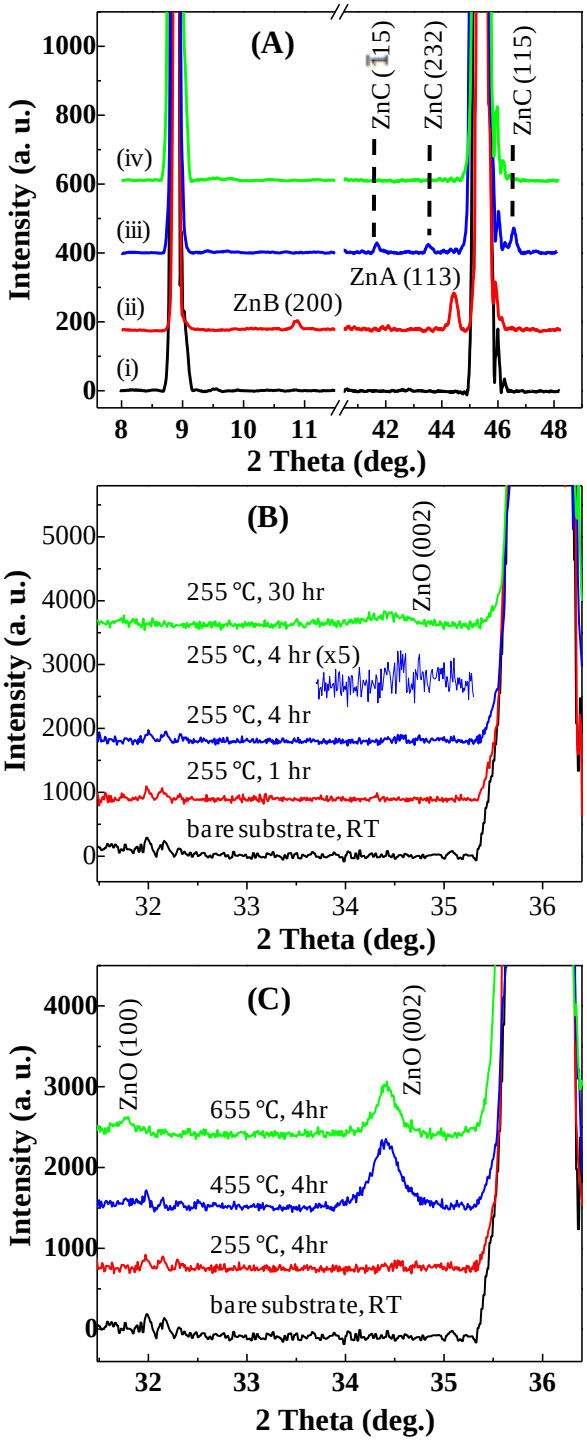

Figure 4.7 (A) Annealing time-dependent evolution of XRD patterns while annealing at 255 ℃, recorded with a time-per-step parameter of 1 sec. (i) bare mica; (ii) $Zn(NO_3)_2.6H_2O$ nanotubes at RT; (iii) after annealing at 255 ℃ for 1 hr; and (iv) after annealing at 255 ℃ for 4 hr. ZnA, ZnB, and ZnC denote $Zn(NO_3)_2.6H_2O$, $Zn(OH)(NO_3).H_2O$, and $Zn_3(OH)_4(NO_3)_2$, respectively. (B) Evolutions of ZnO XRD patterns as a function of the annealing time at 255 ℃, and (C) as a funtion of the annealing temperature, recorded with a time-per-step parameter of 20 sec.

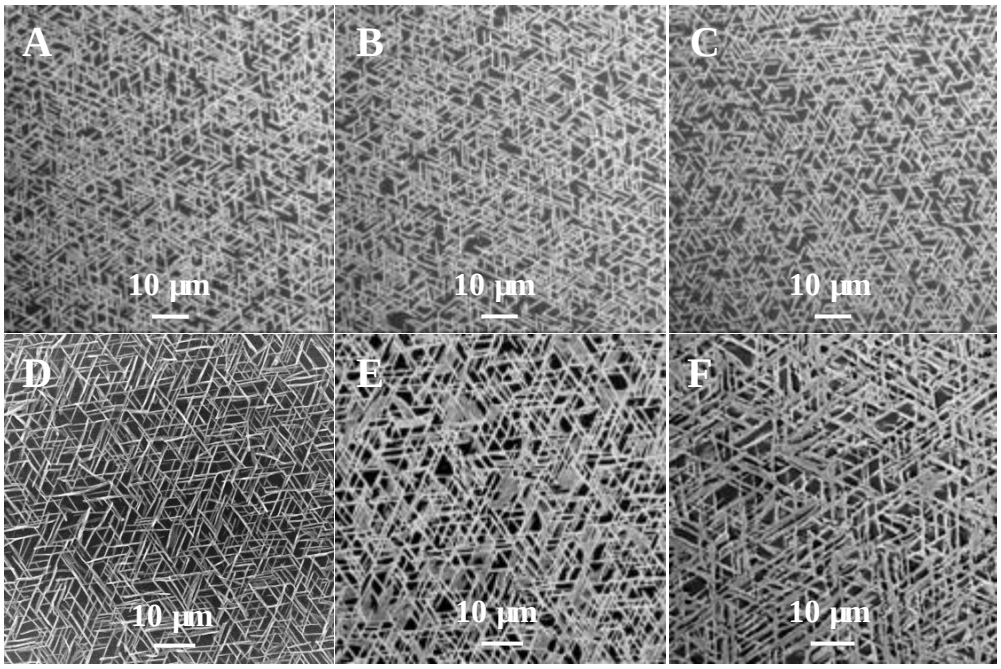

Figure 4.8 Low-magnification SEM images of the network-like assemblies after annealing at different conditions: (A) 255 ℃, 1 hr, (B) 255 ℃, 4 hr, (C) 255 ℃, 30 hr, (D) 355 ℃, 4 hr, (E) 430 ℃, 4 hr, and (F) 655 ℃, 4 hr.

Morphology evolution as a function of the annealing condition was monitored as well. Low-magnification SEM images (Figure 4.8) show that the overall geometrical configuration of the interconnected networks was largely retained after the high-temperature annealings. Close-up view revealed that nanosized pores began to be noticeable after annealing at 255 ℃ for 1 hr, with small size and low density (Figure 4.9A). Both the pore size and density were greatly enhanced after annealing for another 3 hr at the same temperature (Figure 4.9B). When $Zn(NO_3)_2.6H_2O$ nanotubes were subjected to high-temperature annealing, pores are supposed to form in the nanotube walls as a result of releasing the gaseous side products. On the other hand, pores might be formed due to the structural contraction from $Zn(NO_3)_2.6H_2O$ (with density ~2.065 $g.cm^{-3}$) to ZnO

(with density ~5.606 $g.cm^{-3}$) during the thermal annealing. Besides, the formation of pores might also be attributed to the self-organization and recrystallization of ZnO at high temperatures. After a long-term heating up to 30 hr, the pore size was further increased whereas the density dropped significantly (Figure 4.9C). This could be because the small pores have merged into larger ones, as schematically illustrated in Figure 4.9D.

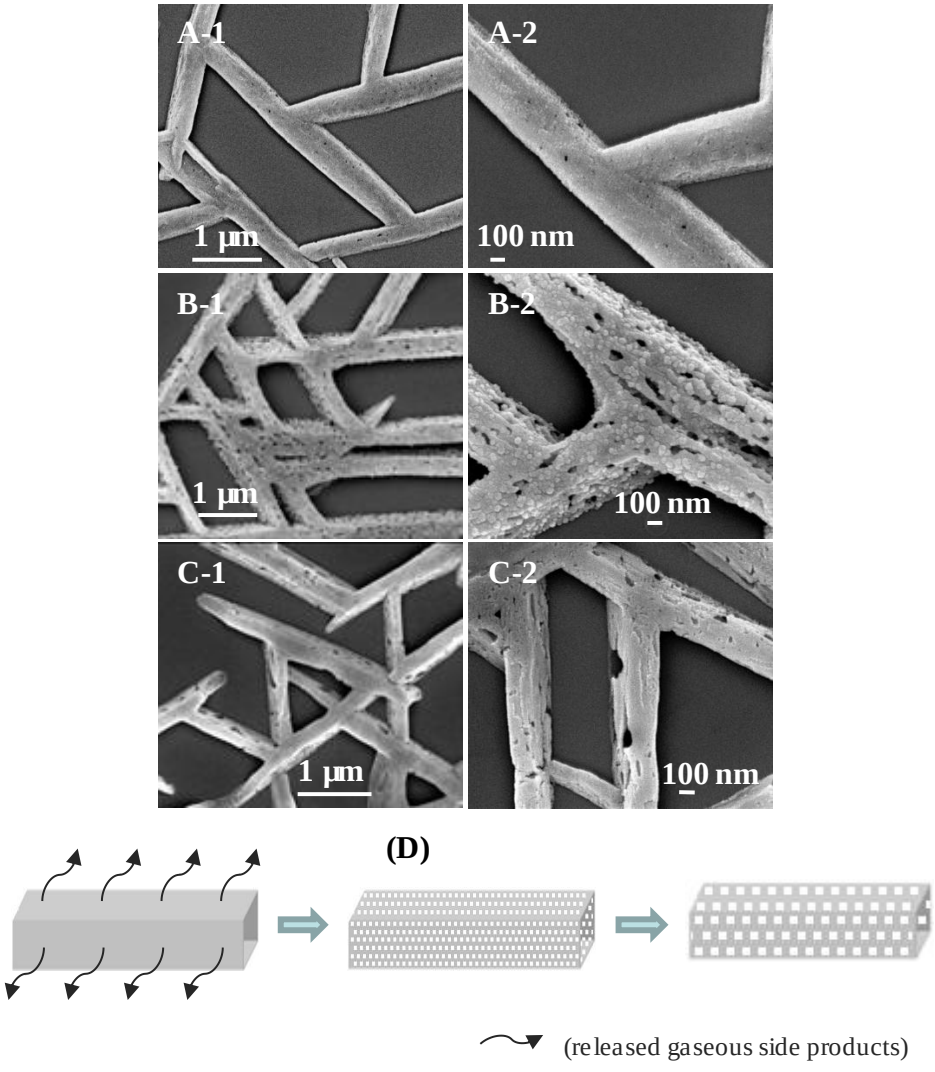

Figure 4.9 Annealing time-dependent morphology evolution of the porous ZnO architectures, after annealing at 255 ℃ for (A) 1 hr, (B) 4hr, and (C) 30 hr. The right panel is the close-up view of the left panel. (D) Schematic model illustrating the formation of pores in the nanotube walls as a result of releasing the gaseous side products.

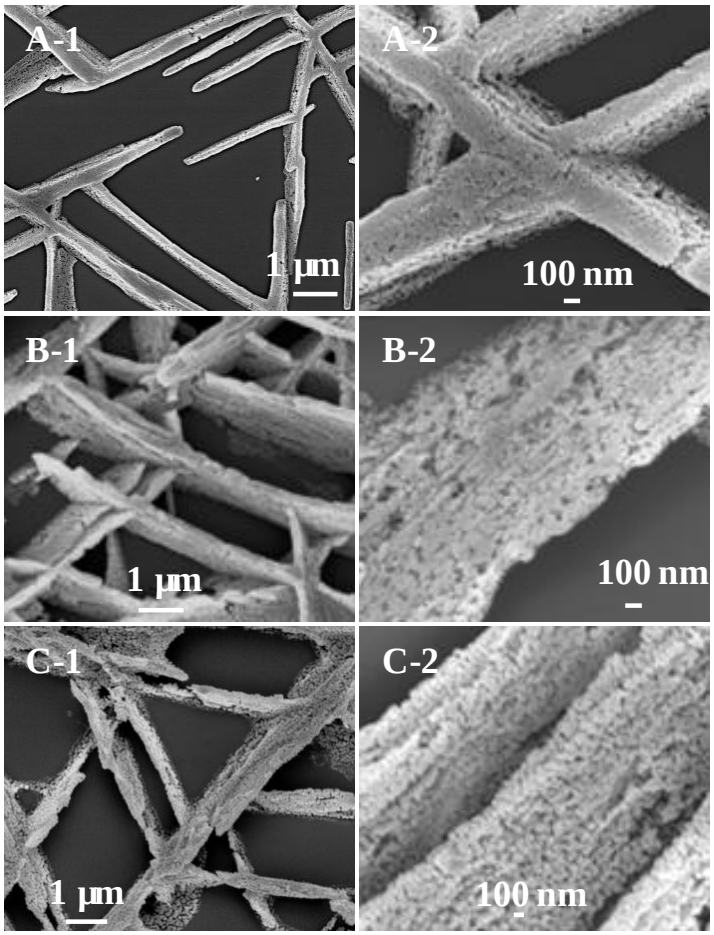

Figure 4.10 Nanosized ZnO granules after annealing 4 hr at (A) 380 ℃, (B) 430 ℃, and (C) 655 ℃. The right panel is the close-up view of the left panel.

Nanosized ZnO granules started to appear at the temperature of 380 ℃ because of a rapid decomposition (Figure 4.10A). Close-up view disclosed that the ZnO granules formed at this temperature were still connected to each other (Figure 4.10A-2). Well-defined ZnO granules with an average size of ~20 nm were obtained at 430 ℃. At the same time, the initial hollow tubular structure was replaced by an erect thin-ribbon structure (Figure 4.10B), which eventually fell on the mica substrate (Figure 4.10C). At higher temperatures, larger-sized ZnO granules were obtained as the small granules were melted and merged into larger

ones. For example, the ZnO granules obtained at 655 ℃ had an average size of ~ 75 nm.

All the annealed samples exhibited two main PL emissions (Figure 4.11A): the near-band-edge (NBE) excitonic related ultraviolet (UV) emission centered at ~380 nm; and the broad deep-level (DL) related visible emission in a wide range of 520 - 750 nm. Both UV and visible emissions show a strong dependence on the annealing temperature. With increase in the annealing temperature, the intensity of UV emission was largely enhanced due to an improved crystallinity of the ZnO samples [45]. The yellow-IR emissions can be attributed to the oxygen interstitials in the oxygen-rich ZnO [46, 47], which is also supported by the EDS analysis (Figure 4.11B). The 655 ℃-annealed ZnO sample exhibited strong green-red emission. The largely enhanced intensity indicates the presence of large amount of defects [48]. An obvious blue shift of the visible emission was noticed as compared to the ZnO samples annealed at low temperatures. The green and yellow-red emissions are attributed to the oxygen vacancies and interstitials, respectively [46-51]. Generally, the green and yellow emissions cannot be observed simultaneously in the same sample [52]. In our case, the high-temperature annealing at 655 ℃ could possibly have broken the Zn-O bonds [48], resulting in the oxygen vacancies. The presence of oxygen vacancies in the high-temperature samples was also confirmed from the EDS spectrum (Figure 4.11C). Due to the short annealing time (4hr in this case), the oxygen vacancies (i.e., green defects)

were limited in the surface layer with the interior oxygen interstitials (i.e., yellow-red defects) retained. As a result, broad green-red emission was achieved.

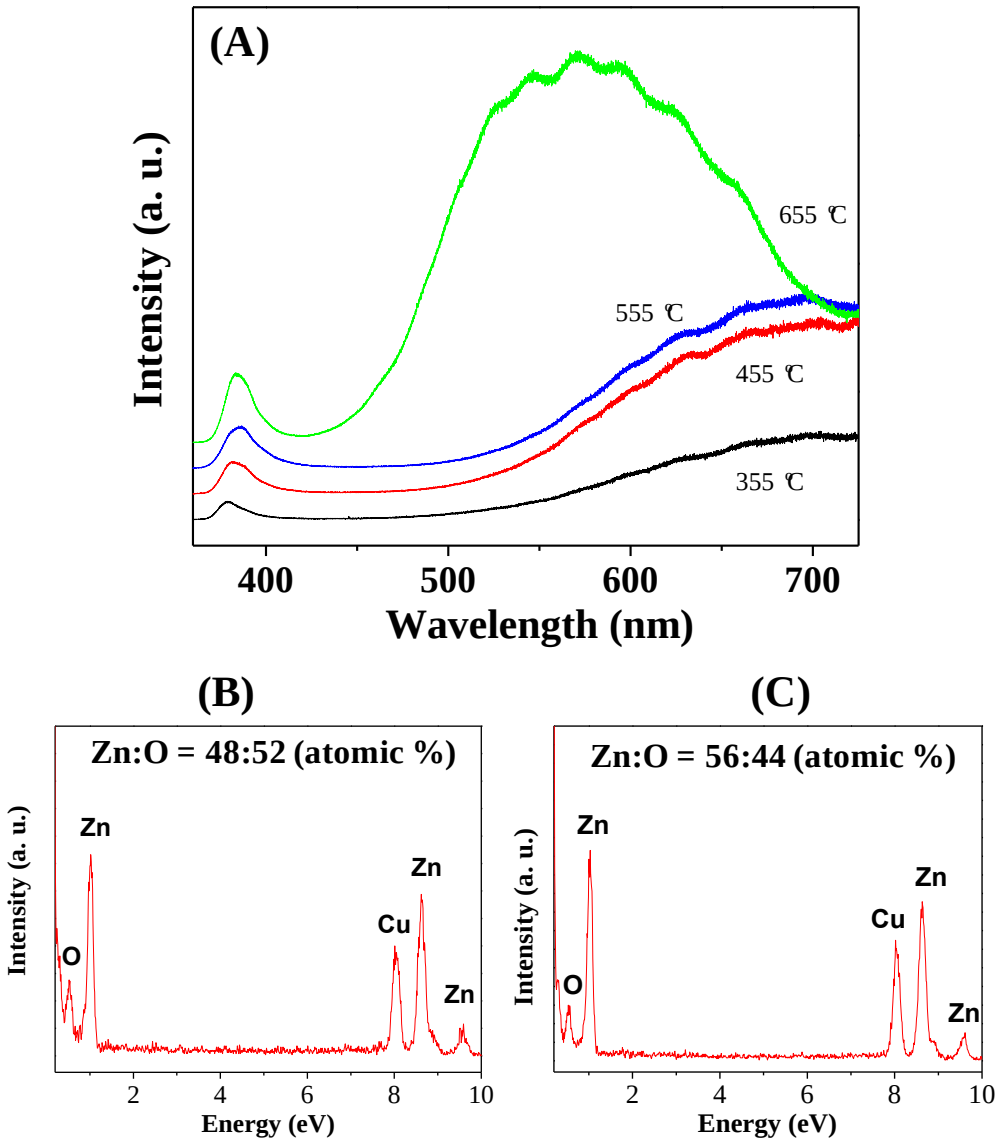

Figure 4.11 (A) PL spectra of the porous ZnO architectures annealed at different temperatures. (B) Typical EDS spectra of the ZnO samples annealed at the temperatures of 355-555 ℃. The Zn:O atomic ratio is 47:52, indicating an oxygen-rich ZnO. (C) Typical EDS spectra of the ZnO samples annealed at the temperature of 655 ℃. The Zn:O atomic ratio is 56:44, indicating an oxygen-deficient ZnO.

Electrical properties of the porous ZnO interconnected networks were examined using two-probe electrical measurements. Single porous ZnO architecture in the network assembly exhibited a symmetric, nonlinear *I-V* response with a measured resistance (R_M) of ~0.74 MΩ (Figure 4.12A). The symmetric, nonlinear nature of the *I-V* curve could either be due to the intrinsic semiconducting nature of the porous ZnO or be characteristic of the Schottky contact between the tungsten probe and the ZnO sample. As the distance between two probes was increased, a rise in the resistance and a transition from the nonlinear to linear *I-V* response was observed (Figure 4.12B-C). The results indicate that the large interconnected network was electrically interconnected and functioned as a single integrated unit. In addition to the longer electrical path, the rise in resistance could be attributed to the large number of interfaces between the interconnected ZnO architectures. The linear *I-V* characteristic could be due to the dominant contribution from the interconnected ZnO architectures compared to that from the Schottky contacts. We have also studied the electrical properties of the isolated clusters with different sizes (Figure 4.13). Similar to the extended network, the clusters showed a symmetric, linear *I-V* response.

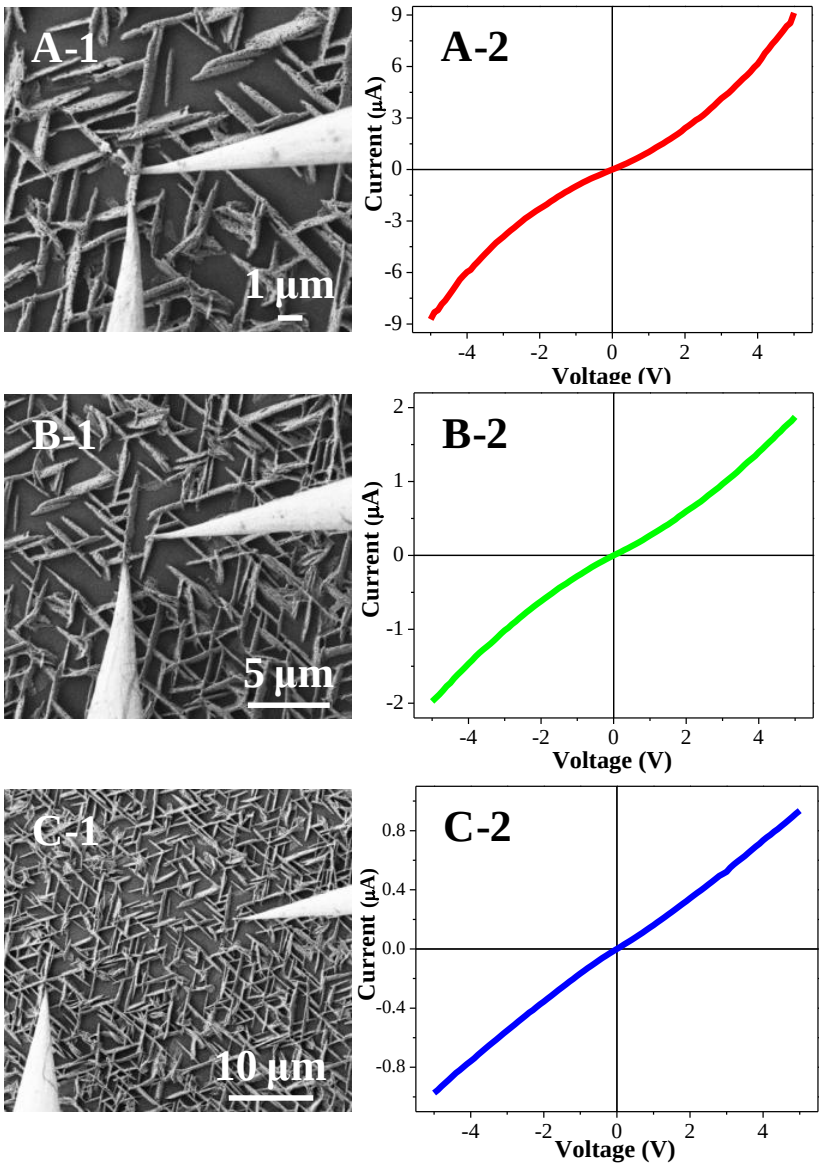

Figure 4.12 Electrical properties of the porous ZnO interconnected networks as a function of the distance between two tungsten probes. (A) R_M ~ 0.74 MΩ, (B) R_M ~ 3.21 MΩ, and (C) R_M ~ 6.0 MΩ.

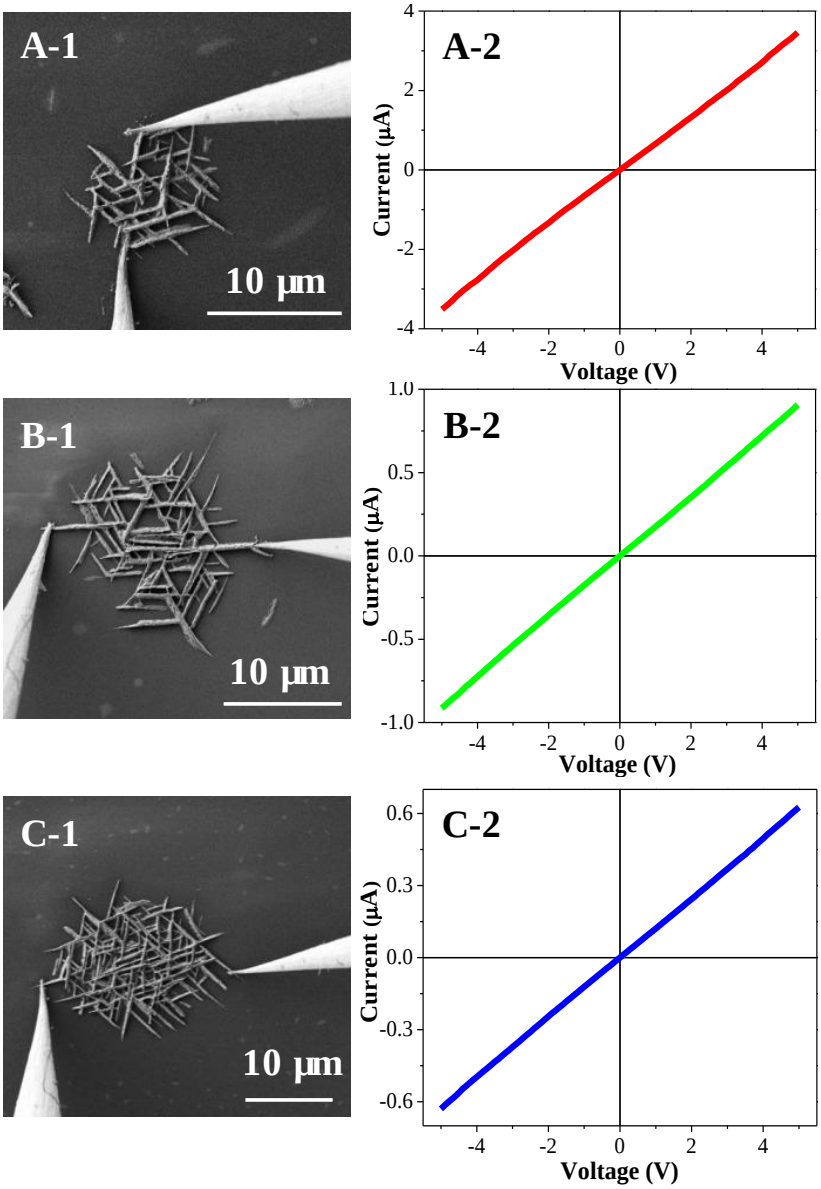

Figure 4.13 Electrical properties of the nanoporous ZnO clusters as a function of the cluster size. (A) R_M ~ 1.45 MΩ, (B) R_M ~ 5.5 MΩ, (C) R_M ~ 8.0 MΩ.

4.4 Conclusions

In conclusion, the epitaxial growth of $Zn(NO_3)_2.6H_2O$ rectangular nanotubes on mica substrates was demonstrated. The solid-phase thermal transformation of $Zn(NO_3)_2.6H_2O$ nanotubes into porous ZnO architectures was explored. The epitaxial $Zn(NO_3)_2.6H_2O$ nanotubes were oriented in directions at

approximately 60 °to each other and self-assembled into large-area, interconnected hexagonal networks. The ZnO architectures with well-tailored porosities were fabricated through the solid-phase thermal decomposition of $Zn(NO_3)_2.6H_2O$ nanotubes under different annealing conditions. The PL spectra exhibited a strong dependence on the annealing temperatures, suggesting the presence of various types of defects in the porous ZnO architectures annealed at different temperatures. The porous ZnO interconnected networks were electrically interconnected and functioned as a single integrated unit that exhibited a symmetric, linear *I-V* characteristic. The epitaxial growth together with the folding-up phenomena renders an intelligent approach to synthesize oriented tubular structures. The synthetic approach described in this article could be further explored to synthesize other 1D materials.

References

1. Djurišić, A. B.; Leung, Y. H. *Small* **2006**, *2*, 944.

2. Özgür, Ü.; Alivov, Ya. I.; Liu, C.; Teke, A.; Reshchikov, M. A.; Doğan, S.; Avrutin, V.; Cho, S.-J.; Morkoç H. *J. Appl. Phys.* **2005**, *98*, 041301.

3. Beek, W. J. E.; Wienk, M. M.; Janssen, R. A. J. *Adv. Funct. Mater.* **2006**, *16*, 1112.

4. Brayner, R.; Ferrari-Iliou, R.; Brivois, N.; Djediat, S.; Benedetti, M. F.; Fivet, F. *Nano Lett.* **2006**, *6*, 866.

5. Kim, J. Y.; Osterloh, F. E. *J. Am. Chem. Soc.* **2005**, *127,* 10152.

6. Kang, B. S.; Pearton, S. J.; Ren, F. *Appl. Phys. Lett.* **2007**, *90,* 083104.

7. Wang, G.; Chen, D.; Zhang, H.; Zhang, J. Z.; Li, J. H. *J. Phys. Chem. C* **2008**, *112*, 8850.

8. Wang, W.; Summers, C. J.; Wang, Z. L. *Nano Lett.* **2004**, *4*, 423.

9. Xiang, B.; Wang, P.; Zhang, X.; Dayeh, S. A.; Aplin, D. P. R.; Soci, C.; Yu, D.; Wang, D. *Nano Lett.* **2007**, *7*, 323.

10. Huang, M. H.; Samuel, M.; Feick, H.; Yan, H.; Wu, Y.; Kind, H.; Weber, E.; Russo, R.; Yang, P. *Science* **2001**, *292,* 1897.

11. Nadarajah, A.; Word, R. C.; Meiss, J.; Konenkamp, R. *Nano. Lett.* **2008**, *8*, 534.

12. Wang, W.; Zeng, B.; Yang, J.; Poudel, B.; Huang, J.; Naughton, M. J.; Ren, Z. *Adv. Mater.* **2006**, *18*, 3275.

13. Kong, X. Y.; Wang, Z. L. *Nano Lett.* **2003**, *3*,1625.

14. Song , R. -Q.; Xu, A. -W.; Deng, B.; Li , Q.; Chen, G. -Y. *Adv. Funct. Mater.* **2007**, *17,* 296.

15. Li, Q.; Kumar, V.; Li, Y.; Zhang, H.; Marks, T. J.; Chang, R. P. H. *Chem. Mater.* **2005**, *17,* 1001.

16. Hu, J. Q.; Li, Q.; Meng, X. M.; Lee, C. S.; Lee, S. T. *Chem. Mater.* **2003**, *15,* 305.

17. Sun, Y.; Fuge, G. M.; Fox, N. A.; Riley, D. J.; Ashfold, M. N. R. *Adv. Mater.* **2005**, *17,* 2477.

18. Zhang, J.; Sun, L.; Liao, C.; Yan, C. *Chem. Commun.* **2002**, 262.

19. Law, M.; Greene, L. E.; Radenovic, A.; Kuykendall, T.; Liphardt, J.; Yang, P. *J. Phys. Chem. B* **2006**, *110*, 22652.

20. Haldar, K. K.; Sen, T.; Patra, A. *J. Phys. Chem. C* **2008**, *112*, 11650.

21. Zhang, Y.; Xu, J.; Xiang, Q.; Li, H.; Pan, Q.; Xu, P. *J. Phys. Chem. C* **2009**, *113*, 3430.

22. Lao, J. Y.; Wen, J. G.; Ren, Z. F. *Nano Lett.* **2002**, *2*, 1287.

23. Li, L.; Pan, S.; Dou, X.; Zhu, Y.; Huang, X.; Yang, Y.; Li, G.; Zhang, L. *J. Phys. Chem. C* **2007**, *111*, 7288.

24. Vayssieres, L.; Keis, K.; Hagfeldt, A.; Lindquist, S. -E. *Chem. Mater.* **2001**, *13*, 4395.

25. Zhou, X. F.; Hu, Z. L.; Chen, Y.; Shang, H. Y. *Mater. Res. Bull.* **2008**, *43*, 2790.

26. Jeong, J. -S.; Lee, J. -Y.; Cho, J. -H.; Suh, H. -J.; Lee, C. -J. *Chem. Mater.* **2005**, *17*, 2752.

27. Li, M. -K.; Wang, D. -Z.; Ding, S.; Ding, Y. -W.; Liu, J.; Liu, Z. -B. *Appl. Surf. Sci.* **2007**, *253*, 4161.

28. Wang, H.; Li, G.; Jia, L.; Wang, G.; Tang, C. *J. Phys. Chem. C* **2008**, *112*, 11738.

29. Zhang, W.; Zhang, D.; Fan, T.; Ding, J.; Guo, Q. X.; Ogawa, H. *Nanotechnology* **2006**, *17*, 840.

30. Yu, H.; Wang, D.; Han, M. –Y. *J. Am. Chem. Soc.* **2007**, *129*, 2333.

31. Yang, J.; Qi, L.; Lu, C.; Ma, J.; Cheng, H. *Angew. Chem. Int. Ed.* **2005**, *44*, 598.

32. Navias, L. *J. Am. Ceram. Soc.***1961**, *44***,** 434.

33. Lu, A. H.; Schüth, F. *Ad*v. *Mater.* **2006**, *18*, 1793.

34. Sun, D.; Riley, A. E.; Cadby, A. J.; Richman, E. K.; Korlann, S. D.; Tolbert, S. H. *Nature* **2006**, *441*, 1126.

35. Shanmugam, Y.; Lin, F. -Y.; Chang, T. -H.; Yeh, C. -T. *J. Phys. Chem. B* **2003**, *107*, 1044.

36. Jackson, J. G.; Novichikhin, A.; Fonseca, R. W.; Holcombe, J. A. *Spectrochimica Acta B* **1995**, *50*, 1423.

37. Mu, J.; Perlmutter D. D. *Thermochimica Acta* **1982**, *56*, 253.

38. Małecki, A.; Małecka B. *Thermochimica Acta* **2006**, *446*, 113.

39. Kozak, A. J.; Wieczorek-Ciurowa, K.; Kozak A. *J. Thermal Anal. Cal.* **2003**, *74*, 497.

40. Auffredic, J.-P.; Louër, D. *J. Solid State Chem.* **1983**, *46*, 245.

41. Yabu, H.; Shimomura, M. *Adv. Funct. Mater.* **2005**, *15*, 575.

42. Deegan, R. D.; Bakajin, O.; Dupont, T. F.; Huber, G.; Nagel, S. R.; Witten, T. A. *Nature* **1997**, *389*, 827.

43. Xia, Y. N.; Yang, P.; Sun, Y. G.; Wu, Y. Y.; Mayers, B.; Gates, B.; Yin, Y. D.; Kim, F.; Yan, Y. Q. *Adv. Mater.* **2003**, *15*, 353.

44. Małecki, A.; Małecka B.; Gajerski, R.; Łabuś, S. *J. Therm. Anal. Cal.* 2003, *72*, 135.

45. Cho, S.; Ma, J.; Kim, Y.; Sun, Y.; Wang, G.; Ketterson, J. B. *Appl. Phys. Lett.* **1999**, *75*, 2761.

46. Greene, L. E.; Law, M.; Goldberger, J.; Kim, F.; Johnson, J. C.; Zhang, Y.; Saykally, R. J.; Yang, P. *Angew. Chem. Int. Ed.* **2003**, *42*, 3031.

47. Li, D.; Leung, Y. H.; Djurišić, A. B.; Liu, Z. T.; Xie, M. H.; Shi, S. L.; Xu, S. J.; Chan, W. K. *Appl. Phys. Lett.* **2004**, *85*, 1601.

48. Zhong, J.; Kitai, A. H.; Mascher, P. *J. Electrochem. Soc.* **1993**, *140*, 3644.

49. Vanheusden, K.; Warren, W. L.; Seager, C. H.; Tallant, D. R.; Voigt, J. A.; Gnade, B. E. *J. Appl. Phys.* **1996**, *79*, 7983.

50. Vanheusden, K.; Seager, C. H.; Warren, W. L.; Tallant, D. R.; Voigt, J. A. *Appl. Phys. Lett.* **1996**, *68*, 403.

51. Li, Y.; Meng, G. W.; Zhang, L. D.; Phillipp, F. *Appl. Phys. Lett.* **2000**, *76*, 2011.

52. Studenikin, S. A.; Golego, N.; Cocivera M. *J. Appl. Phys.* **1998**, *84*, 2287.

53. Ryu, H. –W.; Park, B. –S.; Akbar, S. A.; Lee, W. –S.; Honga, K. –J.; Seo, Y. –J.; Shin, D. –C.; Park, J. –S.; Choi, G. –P. *Sensors and Actuators B* **2003**, 96, 717.

54. Law, J. B. K.; Thong, J. T. L. *Nanotechnology* **2008**, *19*, 205502.

Chapter 5

Macroscopic Concentric Ring Arrays of Radially-Oriented Anthracene Wires Based on Irreversible Liquid Drying and Molecular Self-Assembly

5.1 Introduction

Although surface patterning can now be achieved by various techniques [1-10], it remains a challenge to pattern nanostructures in macroscopic spatial scales. Spontaneous pattern formation in self-assembly is of practical significance and has been extensively studied [11 and references therein] because of its simplicity and versatility. It renders fundamental scientific opportunities to explore the self-assembly behaviors at molecular level. It may also yield structures with newly-emerged and/or amplified properties that otherwise are lack in the elementary structural units [12, 13]. Solution-based self-assembly of organic semiconducting materials is cost effective and highly desirable for fabrication of high-density electronic devices. Self-assembly processes driven by the short-range intermolecular interaction, however, usually result in patterns with limited spatial extent [14-18]. Large-scale patterns of organic compounds have been achieved through the self-assembly processes coupled with irreversible liquid drying processes [19-23].

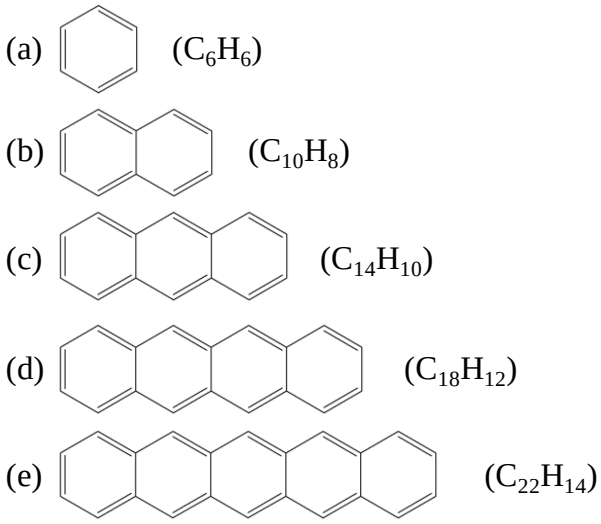

Figure 5.1 Structures of acene molecules: (a) benzene (n = 1), (b) naphthalene (n = 2), (c) anthracene (n = 3), (d) tetracene (n = 4), and (e) pentacene (n = 5).

Acenes are polycyclic aromatic hydrocarbons composed of linearly fused benzene rings [24, 25]. As shown in Figure 5.1, the smallest member in the acene group is benzene. Increasing the number of aromatic rings (n) gives naphthalene (n = 2), anthracene (n = 3), tetracene (n = 4), pentacene (n = 5), and others. The electron rich π-surfaces and rigid linear planar structures of the ancene molecules can effectively facilitate the molecular stacking with maximum overlap of the π-surfaces. Compared to tetracene and pentacene, anthracene has a wider band gap, but exhibits better solubility in most of organic solvents and chemical stability. The drawbacks associated with the wide band gap can be overcome either through the growth of high-quality anthracene single crystals [26] or through the designing and synthesis of anthracene derivatives [27]. For example, the thin film transistors based on the anthracene derivative of (di(phenylvinyl))anthracene were reported to have a parallel performance to the pentacene-based devices [28]. The maximum

optical absorption of acenes depends on the number of aromatic rings in the molecules [29]. With an excitonic singlet state and a photoexcitation energy of E_{S1} = 3.1 eV [30], anthracene is promising candidate for blue organic light emitting diodes (OLEDs).

We developed one-step construction of macroscopic concentration ring arrays of radially-oriented anthracene wires through a simple fast evaporation method. These anthracene wires were grown from fast-dried thin solution layer and found to be substrate-independent. The formation of concentric ring arrays is possibly due to the repeating slipping-and-sticking motions of the contact line - the evaporating frontier where the gas, liquid, and solid phases meet. The growth of one-dimensional (1D) anthracene wires can be attributed to both π-π interaction between anthracene molecules and fingering instability during the irreversible drying of thin solution layers. The radial orientation of anthracene wires was directly driven by the outward capillary flow in the evaporating thin solution layer. The competition between the capillary flow and the Marangoni convectional flow determines either straight or curved anthracene wires. The self-assembled anthracene wire arrays exhibited intense red, green, and blue fluorescence emissions, suggesting possible applications for OLED development.

5.2 Experimental Section

Anthracene white crystalline powder (≥99%) was purchased from Fluka and used as received. Solutions with concentrations in the range of 1-10 mM were

prepared by dissolving the anthracene powder in toluene (Merck, analytical reagent grade) or acetone (Merck, analytical reagent grade). The Si substrates were cleaned by successive ultrasonication procedures: (1) in washing detergent, 5 min; (2) in Milli-Q water (Millipore, ≥18 $M.cm^{-1}$) for 3 times, 5 min for each; (3) in piranha solution (H_2SO_4:H_2O_2 = 7:3), 30 min; (4) in Milli-Q water for 3 times, 5 min for each. The mica substrates, $KAl_2(Si_3AlO_{10})(OH)_2$, were purchased from Mateck-GmbH. Clean mica surface was prepared by cleavage in the ambient air just prior to each sample preparation.

To grow self-assembled anthracene wires, a solution droplet (1-10 μL) was pipetted onto the freshly cleaned substrate. Initially the droplet spread out to form thin solution layer. The solvent evaporation became evident soon after the spreading solution layer established its equilibrium on the substrate. Ideally, the equilibrium thin solution layer was in perfect circular shape with a radius of 3-15 mm. The evaporation rate was controlled by several methods: (1) employing volatile organic solvents with different boiling points (b.p.), i.e., toluene (b.p. 110 ℃) and acetone (b.p. 56 ℃); (2) conducting the evaporation at different temperatures; (3) evaporating the solvent either in the ambient air or in the solvent vapor atmosphere.

Morphology of the self-assembled anthracene wires was characterized by means of bright-field and polarized optical microscopy (OM, Nikon, Eclipse LV100D), fluorescence microscopy (FM, Zeiss Axiovert Microscope with a Zeiss AxioCam MRc digital camera), and tapping-mode atomic force microscopy

(TM-AFM, Nanoscope IIIa, Veeco) operated with "J" scanner and silicon cantilever (force constant: 42 N/m, Nanoworld). The crystallographic information was obtained using powder X-ray diffraction (XRD, Siemens D5000, operated at 40 kV and 40 mA) with monochromatized Cu Kα radiation (λ = 1.54 Å).

5.3 Results and Discussion

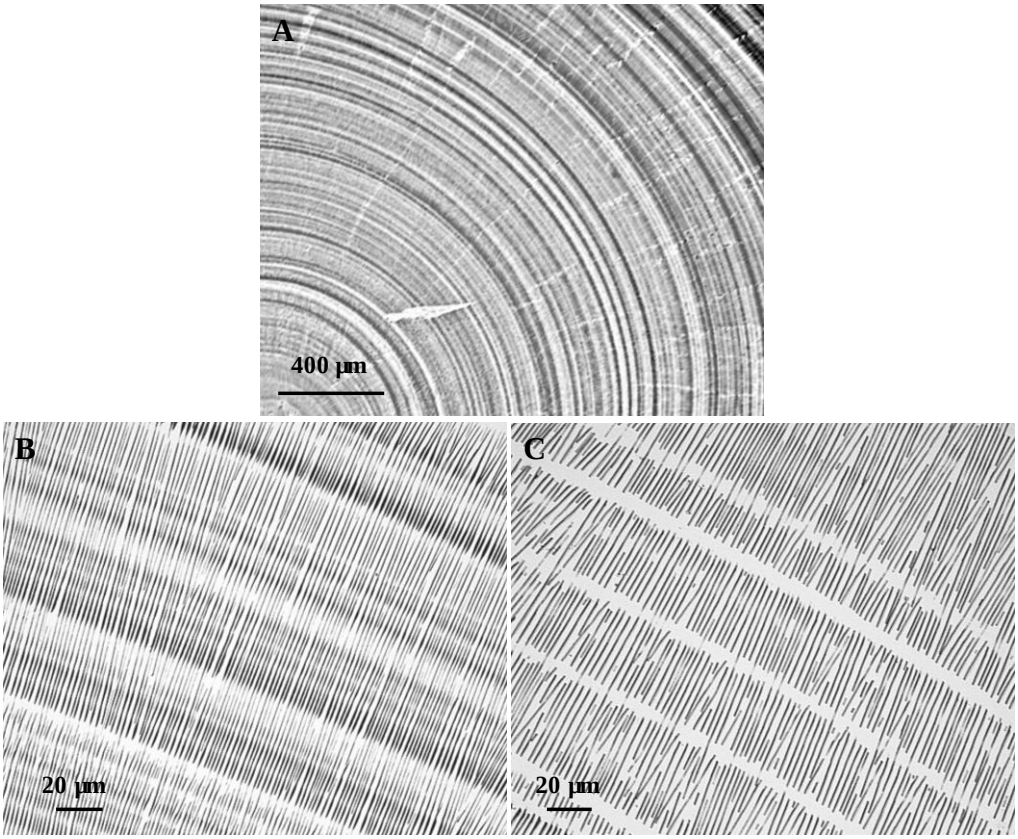

Figure 5.2 Optical micrograph images showing macroscopic concentric ring arrays of radially-oriented anthracene wires grown on Si at 30 ℃, from a 1 mM anthracene/toluene thin solution layer. (B) Close-up view of the long anthracene wires deposited at the peripheral area; (C) Close-up view of the short anthracene wires deposited at the central area.

Figure 5.2A shows typical macroscopic concentric ring arrays of radially-oriented anthracene wires grown on Si at 30 ℃, from 1 mM

anthracene/toluene thin solution layer. Duo to the large spatial scale, the optical micrograph image (with the smallest magnification) only exhibits partial frame of this circular pattern. The concentric ring arrays consist of many circular, alternate black and bright rings covered with millions of radially-oriented anthracene wires. The anthracene wires deposited at the peripheral area are long and run over several circular rings (Figure 5.2B); while much shorter wires can be identified at the central area because there is no anthracene deposited in the narrow bright circular rings (Figure 5.2C). The high-resolution AFM characterization further reveals that the anthracene wires have a width of 1 ± 0.2 μm and a mean height of 130 nm (Figure 5.3).

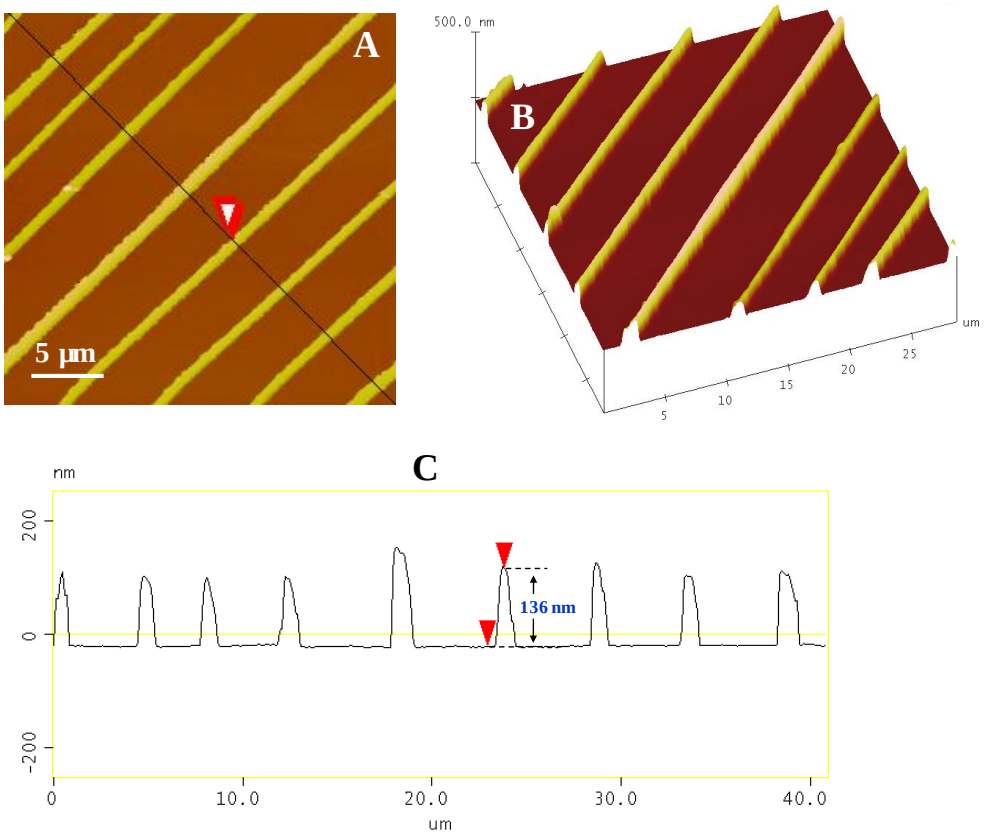

Figure 5.3 High-resolution AFM images showing the anthracene wires grown on Si at 30 ℃, from a 1 mM anthracene/toluene thin solution layer. (A) 2D top view; (B) 3D surface plot; and (C) cross-section profile of the anthracene wires.

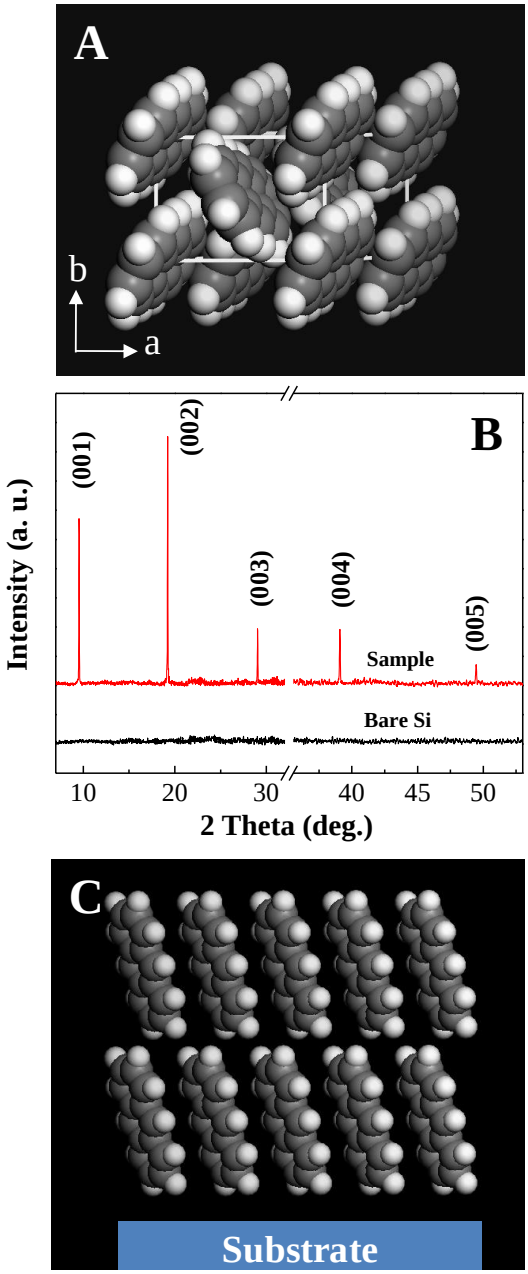

Figure 5.4 (A) Unit cell of monoclinic anthracene; (B) Charateristic XRD pattern of the self-assembled anthracene wires grown on Si; and (C) schematic model illustrating the edge-on orientation of the anthracene molecules on the Si substrate.

Anthracene has a monoclinic prismatic crystal structure with the unit cell parameters of a = 8.559 Å, b = 6.04 Å, c = 11.16 Å, $\alpha = \gamma = 90^{o}$, and $\beta = 124^{o}$ (JCPDS card no. 33-1532). Each unit cell has two molecules and a well defined cleavage plane (the ab plane) (Figure 5.4A). The self-assembled anthracene wires

grown on Si, as shown in Figure 5.4B, exhibit 5 diffraction peaks at 9.54, 19.20, 29.04, 39.07, and 49.45 º. These peaks can be assigned the anthracene (00l) diffractions (l = 1, 2, 3, 4, and 5), indicating the high-quality of single crystalline anthracene wires. The characteristic XRD peaks also suggest that the self-assembled anthracene molecules adopt an edge-on orientation as illustrated in Figure 5.4C, possibly attributed by the π-π stacking between the planar anthracene molecules.

It is known that electromagnetically anisotropic materials, such as single crystals, exhibit direction-dependent optical properties when interacting with polarized light. The anisotropic materials appear dark under polarized optical microscope when their optical axes are perpendicular to the vibration directions of polarizer and analyzer [37]. Such positions are called the extinction positions. However, they display the maximum brightness at the diagonal position when their optical axes are at 45 ºto the vibration directions of polarizer and analyzer. The highly-uniform molecular stacking in the self-assembled anthracene wires suggests possible unique optical properties of these anthracene nanowires. Figure 5.5 shows both the bright-field and polarized optical micrograph images of the same self-assembled anthracene wires. It is manifested that the anthracene wires oriented in different directions exhibit brightness contrast under the polarized optical microscope (Figure 5.5B). The brightest wires (denoted by the solid arrows) are always oriented at approximate 45 º to the darkest ones (denoted by the dash arrows).

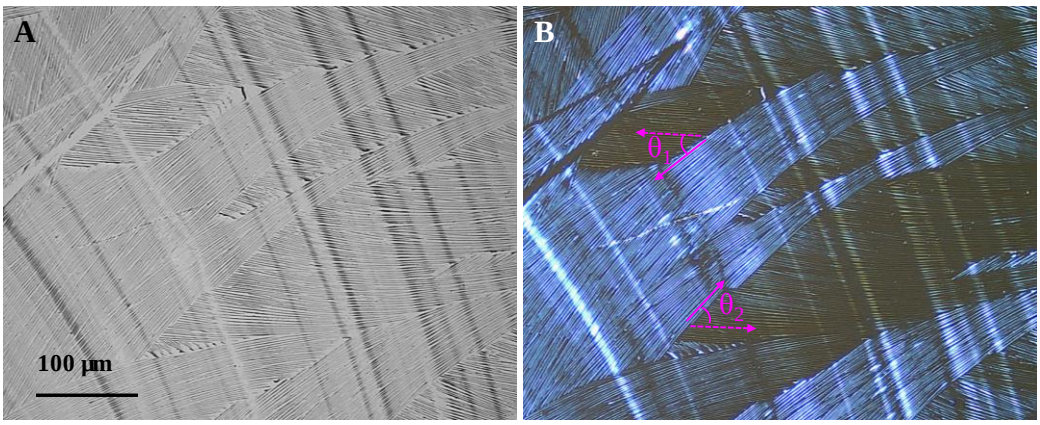

Figure 5.5 Bright-field (A) and polarized (B) optical micrograph images showing the same self-assembled anthracene wires. The brightest wires (denoted by the solid arrows) are always oriented at approximate 45 °to the darkest ones (denoted by the dash arrows). θ_1 = 41 °, and θ_2 = 49 °.

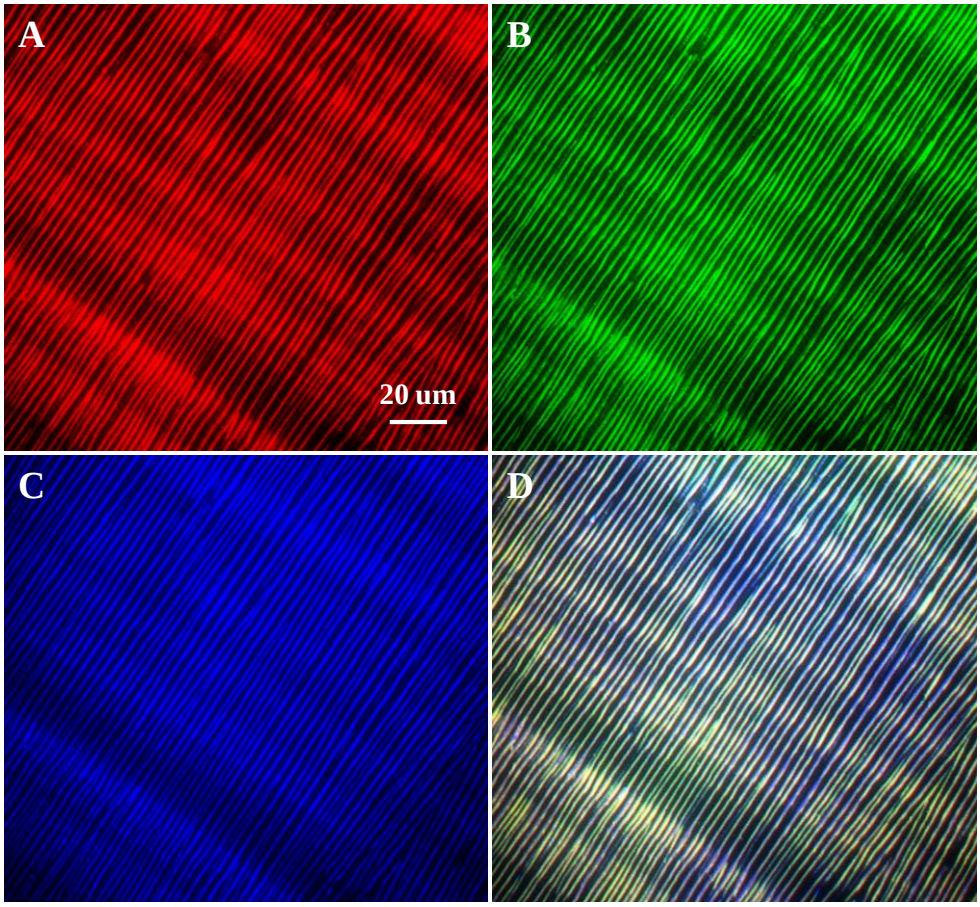

Figure 5.6 FM images showing (A) red, (B) green, and (C) blue fluorescence emissions of the self-assembled anthracene wires. (D) is the merged image of (A), (B) and (C).

The self-assembled anthracene wire arrays were visualized using fluorescence microscopy (FM). As shown in Figure 5.6, the self-assembled anthracene wire arrays exhibited intense red, green, and blue fluorescence emissions under the excitations of 546 nm, 500 nm, and 445 nm, suggesting a promising candidate for OLED development.

The formation of macroscopic concentric ring arrays of radially-oriented anthracene wires can be understood as following. When the solution droplet is pippetted onto a solid surface, it spreads out fast to form thin solution layer until the equilibrium is established. The solution layer is initially held immobile at the contact line. The force holding the solution layer in place originates from the surface roughness of substrates, the chemical heterogeneity, etc [31, 32]. The solute dispersed in solution can also exert great influence on the contact line motion. For example, the solute aggregates on the substrate can serve as surface roughness that contributes to the contact line sticking. As schematically illustrated in Figure 5.7, during evaporation (I→II), the slipping contact line is stuck several times. The formation of circular, alternate black and bright rings is possibly due to the repeating slipping-and-sticking motions of the contact line. The black-and-grey contrast of the circular rings is approximately proportional to the surface loading of anthracene. The bright rings have a much lower surface loading of anthracene compared to the black rings. The backward slipping of contact line gives a low surface loading of anthracene, evidenced by the bright rings. If the contact is slipping fast and the solution is dilute, even no aggregation can occur during the

slipping periods. Such situation usually happens at the end of evaporation, yielding the short anthracene wires in the central area. In contrast, the sticking of contact line assures a heavier surface loading within the same time period and hence leads to the deposition of black rings.

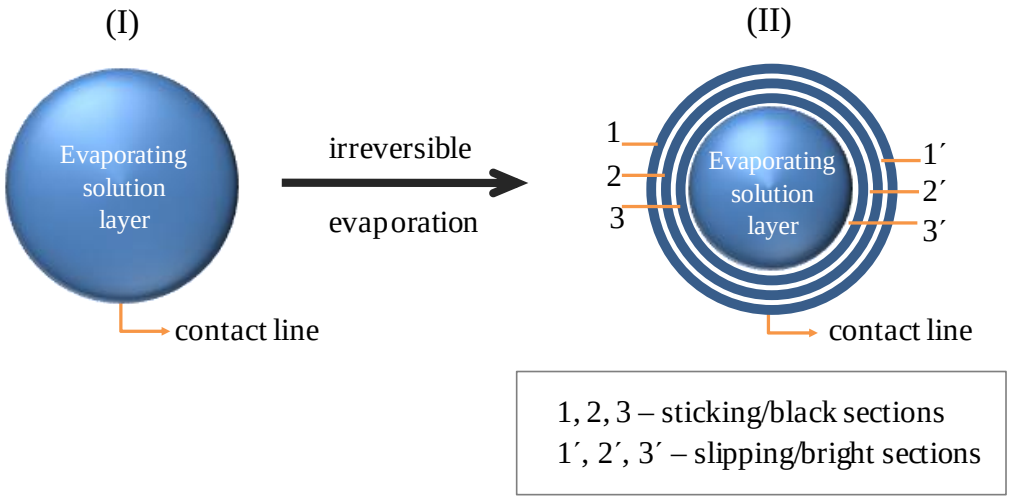

Figure 5.7 Proposed mechanism responsible for the formation of concentric ring arrays. During the evaporation of thin solution layer (I→II), the slipping contact line is stuck several times. Each sticking of the contact line yields one circular high-surface-loading ring. In contrast, each slipping of contact line generates one low-surface-loading ring. The repeating slipping-and-sticking motions of the contact line lead to the formation of concentric ring arrays.

During evaporation, the solvent loss is most remarkable at the contact line. The capillary flow forces the interior solution outward to compensate the solvent loss at the contact line. The interior anthracene solute is carried outward to the contact line as well (Figure 5.8). Consequently, the anthracene concentration at the region close to the contact line is greatly increased. Anthracene condenses on the substrate as long as the local concentration reaches the supersaturation threshold. On the other hand, the anthracene condensation largely decreases the local surface tension. The

immobile contact line is free to slip backward again. The surface tension gradient further squeezes liquid diffusing away the high-surface-tension and low-concentration regions to the low-surface-tension and high-concentration regions, as schematically illustrated in Figure 5.8B. Such a mass transfer phenomenon is so-called solutal Marangoni effect and commonly referred as "fingering instablility" [33-36]. The resulting fluid flow is called Marangoni convectional flow. The anthracene deposition is thus largely enhanced by the Marangoni convectional flow. The primary anthracene aggregates served as "fingers" to collect more anthracene source from the solution phase and eventually develop into 1D radially-oriented wires. In this regard, the growth of anthracene wires is the cooperative outcome of the capillary flow and the Marangoni convectional flow. If the capillary flow is stronger than the Marangoni convectional flow, the anthracene aggregation occurs along Route I and hence straight wires are grown (Figure 5.9); otherwise, it takes place along Route II and yields the curved wires. The straight anthracene wires shown in Figure 5.2 imply that the capillary flow was stronger than the Marangoni convectional flow in the 1 mM evaporating solution layer.

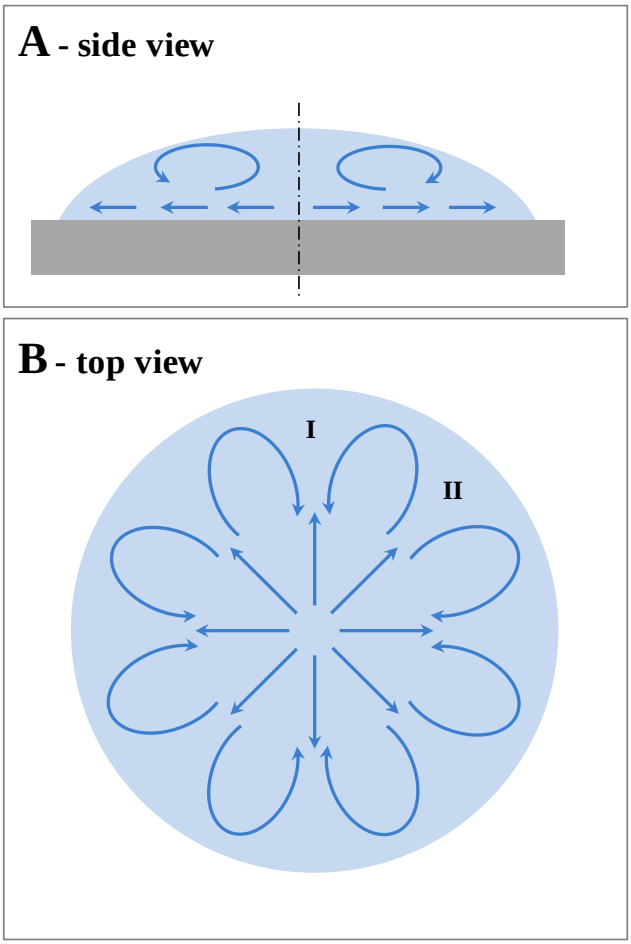

Figure 5.8 Schematic models illustrating capillary flow and Marangoni convectional flow formed inside an evaporating thin solution layer. (B) Side view, and (C) top view.

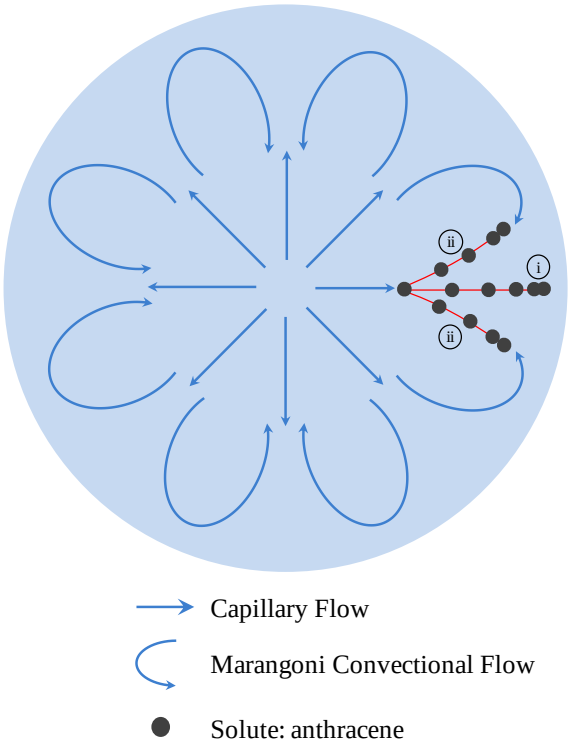

Figure 5.9 Growth routes of anthracene wires are determined by the competition between the capillary flow and the Marangoni convectional flow. If the capillary flow is stronger than the Marangoni convectional flow, the anthracene aggregation occurs along Route I and hence straight wires are grown; otherwise, it takes place along Route II and yields the curved wires.

The capillary flow in the thin solution layer largely depends on how fast the solvent is evaporated. The faster the solvent evaporation is, the stronger the capillary flow would be. The growth of anthracene wires was then conducted at 20 ℃. A weak capillary flow is expected at 20 ℃ as the solvent evaporation is slow at this temperature. The as-grown anthracene wires are displayed in Figure 5.10. It shows that the anthracene wires were self-assembled into concentric ring arrays, similar to that at 30 ℃. Close-up view disclosed that the anthracene wires grown at 20 ℃ are slightly curved (Figure 5.10B), different from the straight wires grown at 30 ℃. It suggests that the Marangoni convectional flow in the thin

solution layer was stronger than the capillary flow. The anthracene aggregates were forced to along Route I and eventually developed into the curved wires. The growth of anthracene wires was also carried out in higher-concentration solution layer.

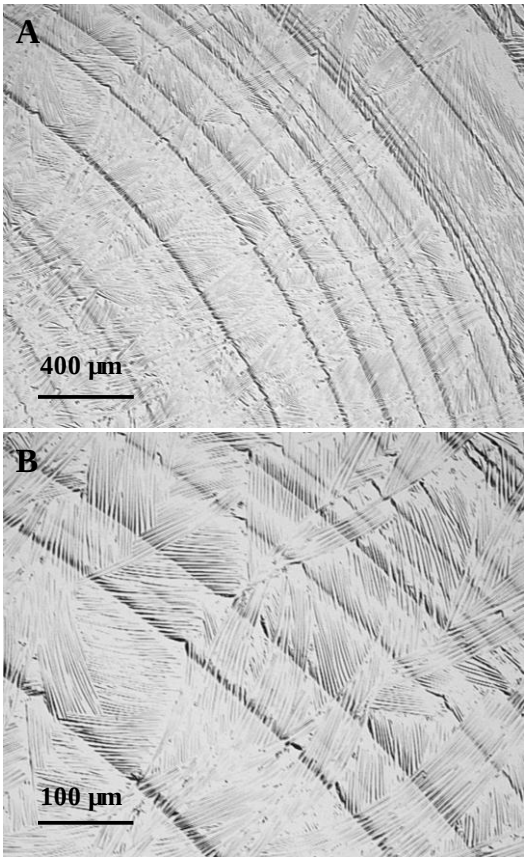

Figure 5.10 Optical micrograph images showing the macroscopic concentric ring arrays of curved anthracene wires grown on Si at 20 ℃, from a 1 mM thin solution layer. (B) is the close-up view of (A).

Figure 5.11 shows the concentric ring arrays grown from 4 mM thin solution layer, similar to that grown from the 1 mM thin solution layer. However, close-up view revealed that the anthracene wires in this case were curved. Since the solutal Marangoni effect is induced by the concentration gradient, a stronger Marangoni convectional flow is expectable in the higher-concentration solution layer. We

assume that the strong Marangoni flow forced the anthracene aggregates to along Rout II and yielded the curved wires.

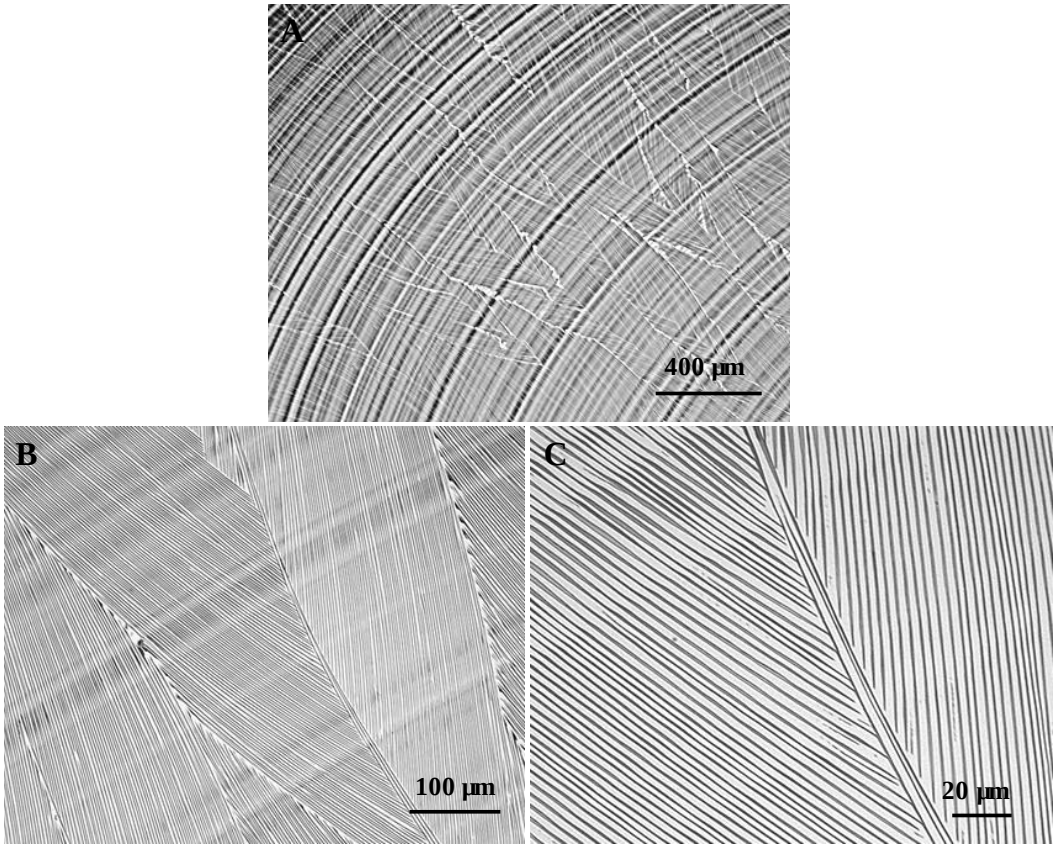

Figure 5.11 Optical micrograph images showing the macroscopic concentric ring arrays of curved anthracene wires grown on Si at 30 ℃, from a 4 mM thin solution layer. (B-C) are the close-up views of (A).

It was reported that the growth of ring-like patterns can take place from a wide range of drying liquid layers, independent on the chemical natures of dispersed materials (solute), liquid carriers (solvent), and substrates [32, 38]. Besides the Si substrate, we have conducted similar experiments on mica. The Si surface treated with piranha solution is relatively rough; whereas the single crystalline mica has atomic flat surface. Figure 5.12A shows that the concentric ring arrays grown on mica are similar to that on Si. The characteristic XRD pattern is shown in Figure

5.12B. Besides the diffraction peaks from the single crystalline mica substrate, it also exhibits 5 peaks that can be assigned to the anthracene (00l) (l = 1, 2, 3, 4, and 5) diffractions. It suggests that the anthracene wires grown on mica have a similar monoclinic crystal structure and adopt a similar edge-on orientation on the mica substrate. The results so far suggest that the growth of 1D anthracene wires and their self-assembly into concentric ring arrays are substrate-independent.

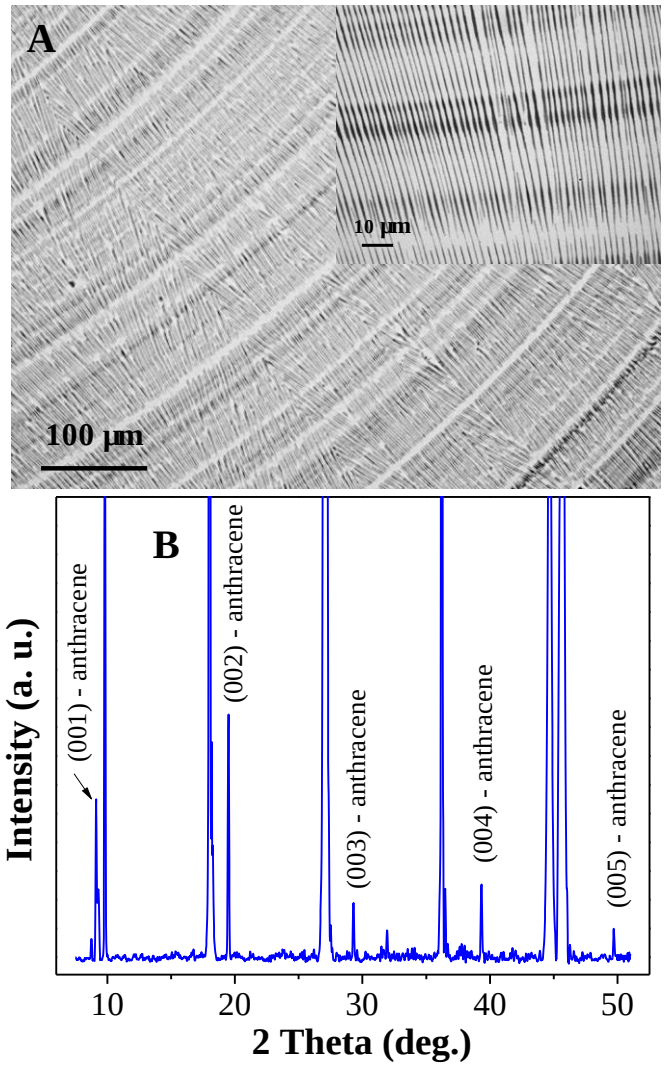

Figure 5.12 (A) Optical micrograph image showing the macroscopic concentric ring arrays of radially-oriented anthracene wires grown on the atomic flat mica surface. The inset is the close-up view. (B) Characteristic XRD pattern of the anthracene wires grown on mica. The unlabeled diffraction peaks are from the single crystalline mica substrate.

Figure 13A shows the randomly oriented anthracene short rods grown from a 10 mM anthracene/acetone thin solution layer. Compared to toluene, acetone has a lower b.p. of 56 ℃ and evaporates more rapidly under the same conditions. Instead of the steady evaporation with the repeating slipping-and-sticking motions of the contact line, the thin solution layer evaporated furiously and ruptured into smaller droplets. Alternatively, a slow evaporation of the anthracene/acetone thin solution layer was achieved by conducting the evaporation in acetone vapor atmosphere. The as-grown structures are displayed in Figure 13B. It shows that the anthracene wires are self-assembled into hierarchical patterns similar to that obtained from the anthracene/toluene solution layer.

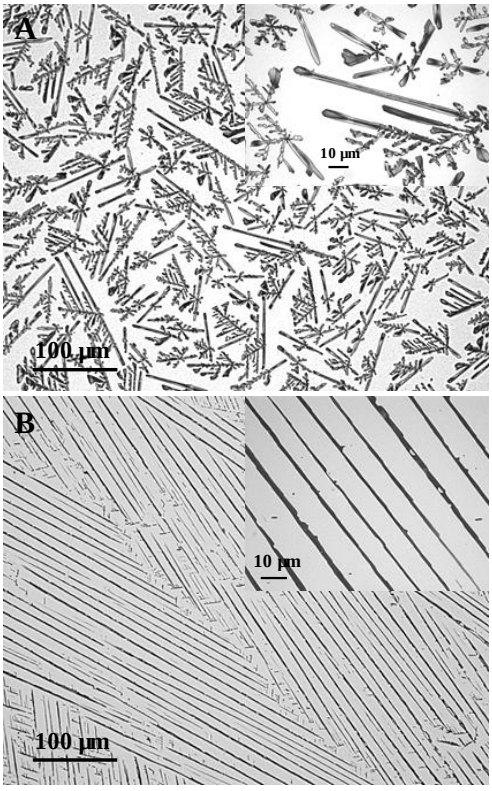

Figure 5.13 Optical micrograph images showing (A) randomly oriented anthracene short rods, when the acetone solvent was evaporated rapidly in the ambient atmosphere, and (B) macroscopic arrays of oriented anthracene wires, when the acetone solvent was evaporated slowly in the acetone vapor atmosphere.

5.4 Conclusion

The drying-assisted self-assembly of anthrancene molecules was investigated. Macroscopic concentric ring arrays of millions of radially-oriented anthracene wires were grown from fast-dried thin solution layer. The mechanisms involved in the pattern formation were discussed based on the irreversible liquid drying and molecular self-assembly. The formation of concentric ring arrays is possibly due to the repeating slipping-and-sticking motions of the contact line. The growth of single crystalline anthracene wires can be attributed to both the fingering instability and the π-π interaction between anthracene molecules. The radial orientation of anthracene wires is driven by the outward capillary flow. The morphology of anthracene wires, either curved or straight, was determined by the competition between the capillary flow and the Marangoni convectional flow. The self-assembled anthracene wires exhibited intense multiple fluorescence emissions, implying a promising candidate for OLED development.

References

1. Mooney, J. F.; Hunt, A. J.; McIntosh, J. R.; Liberko, C. A.; Walba, D. M.; Rogers, C. T. *Proc. Natl. Acad. Sci.* **1996**, *93*, 12287.

2. Öner, D.; McCarthy, T. J. *Langmuir* **2000,** *16,* 7777.

3. Xiang, C.; Yang, Y.; Penner, R. M. *Chem. Commun.* **2009**, 859.

4. Demers L. M.; Ginger, D. S.; Park S. -J.; Li, Z.; Chung, S.-W.; Mirkin, C. A. *Science* **2002**, *296*, 1836.

5. Lee, K. -B.; Park, S. -J.; Mirkin, C. A.; Smith, J. C.; Mrksich, M. *Science* **2002**, *295*, 1702.

6. Ginger, D. S.; Zhang, H.; Mirkin, C. A. *Angew. Chem. Int. Ed.* **2004**, *43*, 30.

7. Son, J. Y.; Shin, Y. H.; Ryu, S.; Kim, H.; Jang, H. M. *J. Am. Chem. Soc.* **2009**, *131*, 14676.

8. Xia, Y.; Whitesides, G. M. *Angew. Chem. Int. Ed.* **1998**, *37*, 550.

9. Aizenberg, J.; Black**,** A. J.; Whitesides, G. M. *Nature* **1999**, *398*, 495.

10. Shallcross, R. C.; Chawla, G. S.; Marikkar, F. S.; Tolbert, S.; Pyun, J.; Armstrong, N. R. *ACS NANO* **2009**, *3*, 3629.

11. Feyter, S. D.; Schryver, F. C. *Chem. Soc. Rev.* **2003**, *32*, 139.

12. Du, Y.; Han, S.; Jin, W.; Zhou, C.; Levi, A. F. *Appl. Phys. Lett.* **2003**, *83*, 996.

13. Xia Y. *Adv. Mater.* **2001**, *13*, 369.

14. Zhang, H-M.; Xie, Z-X.; Mao, B-W.; Xu, X. *Chem. Eur. J.* **2004**, *10*, 1415.

15. Feyter, S. D.; Miura, A.; Yao, S.; Chen, Z.; Würthner, F.; Jonkheijm, P.; Schenning, A. P. H. J. E.; Meijer, W.; Schryver, F. C. D. *Nano Lett.*, **2005**, *5*, 77.

16. Kim, K.; Plass, K. E.; Matzger, A. J. *J. Am. Chem. Soc.* **2005**, *127*, 4879.

17. Plass, K. E.; Engle, K. M.; Matzger, A. J. *J. Am. Chem. Soc.* **2007**, *129*, 15211.

18. Feyter, S. D.; Schryver, F. C. D. *J. Phys. Chem. B* **2005**, *109*, 4290.

19. van Hameren, R.; Schön, P.; van Buul, A. M.; Nolte, R. J. M. *Science* **2006**, *314*, 1433.

20. Yabu, H.; Shimomura, M. *Adv. Func. Mater.* **2005**, *15*, 575.

21. Karthaus, O.; Gråsjö, L.; Maruyama, N.; Shimomura, M. *Chaos* **1999**, *9*, 308.

22. Hong, S. W.; Xu, J.; Xia, J.; Lin, Z.; Qiu, F.; Yang, Y. *Chem. Mater.* **2005**, *17*, 6223.

23. Hong, S. W.; Xu, J.; Lin, Z. *Nano Lett.* **2006**, *6*, 2949.

24. Clar, E. *polycyclic hydrocarbons*; Academic Press: London, **1964**.

25. Clar, E. *The Aromatic Sextet*; Wiley: London, **1972**.

26. Briseno, A. L.; Aizenberg, J.; Han, Y. -J.; Penkala, R. A.; Moon, H.; Lovinger, A. J.; Kloc, C.; Bao Z. *J. Am. Chem. Soc.*, **2005**, *127*, 12164.

27. Jiang, L.; Gao, J.; Wang, E.; Li, H.; Wang, Z.; Hu, W.; Jiang, L. *Adv. Mater.* **2008**, *20*, 2735.

28. Klauk, H.; Zschieschang, U.; Weitz, R. T.; Meng, H.; Sun, F.; Nunes, G.; Keys, D. E.; Fincher, C. R.; Xiang, Z. *Adv. Mater.* **2007**, *19*, 3882.

29. Pope, M.; Swenberg, C. *Electronic Processes in Organic Crystals*, Clarendon Press, **1982**.

30. Meyer, Y. H.; Astier, R.; Leclercq, J. M. *J. Chem. Phys.* **1972**, *56*, 801.

31. Johnson, R.; Dettre, R. in Contact Angle, *Wettability and Adhesion*, edited by F. M. Fowkes, *Advances in Chemistry Series* Vol. 43, American Chemical Society, Washington, DC, **1964**, 112.

32. Deegan R. D. *Phys. Rev. E* **2000**, *61*, 475.

33. Troian, S. M.; Wu, X. L.; Safran, S. A. *Phy. Rev. Lett.* **1989**, *62*, 1496.

34. Melo, F.; Joanny, J. F.; Fauve, S. *Phys. Rev. Lett.* **1989**, *63*, 1958.

35. Vuilleumier, R.; Ego, V.; Neltner, L.; Cazabat, A. M. *Langmuir* **1995**, *11*, 4117.

36. Fanton, X.; Cazabat, A. M. *Langmuir* **1998**, *14*, 2554.

37. Polarizer: the primary polarizing device which changes the natural incident light into linearly polarized light. Analyzer: the secondary polarizing device placed in the orthogonal position to the polarizer.

38. Deegan, R. D.; Bakajin, O.; Dupont, T. F.; Huber, G.; Nagel, S. R.; Witten, T. A. *Nature* **1997**, *389*, 827.

Chapter 6

Macroscopic Surface Architectures of Self-Assembled (3-Aminopropyl)triethoxysilane (APTES) and Non-equilibrium Crystalline Patterns of APTES Oligomers

6.1 Introduction

Pattern formation and selection are of growing interest and have great implications in a wide range of fields, including the fundamental understanding of the organization behaviors at molecular level (self- and/or imposed molecular organization), the surface functionality, and the building of high-density electronic device arrays at specific locations in a predesigned manner. Various approaches have been developed for surface patterning. [1-10] It is still challenging to achieve one-step periodic surface patterning over large scales. Self-assembled patterning is of practical significance and has been extensively studied [11 and references therein] because of its low cost and versatility. The molecular self-assembly driven by the short-range intermolecular interactions, usually results in patterns with limited spatial scales [12-17]. The molecules usually adopt the unique high-density packing to form complete self-assembled monolayers (SAMs). The spatial scales and pattern selectivity can be largely enhanced, providing that the self-assembly is coupled with other processes such as the irreversible liquid drying [18-22].

Hydroxylated surfaces of SiO_2, metal oxides, ceramics, and mica that modified with physically robust silane coupling agents (SCAs) are of interest with respect to

applications in electronics [23, 24] and biosensors [25, 26]. (3-aminopropyl)triethoxysilane (APTES, Figure 6.1A), $H_2N(CH_2)_3Si(OC_2H_5)_3$, is one of the most investigated SCAs. The reactive amino heads of APTES can be further linked to biomacromolecules [27-29], liquid crystals [30], polymers [31, 32], and nanoparticles [33]. APTES self-assembled molecular layers on various surfaces were well documented in literature [34-38]. Previous studies indicated that the APTES self-assembly is highly sensitive to water [38, 39]. It was believed that the presence of water is necessary for the hydrolysis of the ethoxy groups before the APTES molecules are covalently attached to the hydroxylated surfaces. On the other hand, the hydrolyzed APTES exists mainly in the form of low-molecular-weight oligomers in aqueous solution [40, 41]. The oligomers condense partially into larger-sized clusters. APTES monomers can only be detected in very dilute aqueous solution [41]. Undesired bumps were formed due to the adsorption of oligomer clusters onto the hydroxylated surfaces [31, 34, 42]. Much effort was devoted to obtain homogeneous SAMs, including the adsorption from vapor phase [38, 43], the post-adsorption annealing [35], and the employment of anhydrate solvent [44]. However, the self-assembly of SCAs from aqueous solution is highly desirable for the surface modification in practice. It is therefore worth further investigation of the APTES self-assembly from aqueous solution. On the other hand, it is of fundamental importance to understand the self-assembly mechanism. Compare to the analytical techniques that give the average information over a large area, such as Infrared spectroscopy (IR), ellipsometry, and X-ray

photoelectron spectroscopy (XPS), atomic force microscopy (AFM) excels in presenting the local structure of SAMs and thus appropriate to study the self-assembly mechanism at microscopic level. Previous AFM studies indicated that the self-assembly of octadecyltrichlorosilane (OTS) started from the building of discrete islands, which gradually grew into densely-compacted, complete monolayers [45, 46]. Although three-dimensional (3D) islands were reported previously in the self-assembly of APTES [31, 34, 42], to the best of our knowledge, such kind of "3D island" growth mechanism has yet to be proposed for the self-assembly of APTES.

Herein we describe the self-assembly of APTES on mica from thin aqueous solution layers through a simple fast-drying method. The mica substrate, $KAl_2(Si_3AlO_{10})(OH)_2$, was employed because it is one of the well-known hydroxylated surfaces and has been widely used in the immobilization of biological micromolecules [47-49]. The APTES self-assembled molecular layers were patterned with macroscopic concentric ring arrays, attributed to the repeating slipping-and-sticking of the contact line under fast-drying conditions. The molecular form of APTES in the aqueous solution, either monomeric or oligomeric, was found to be crucial for the self-assembly of APTES and for the structures of APTES self-assembled molecular layers. In dilute aqueous solution ($\leq$ 0.125% v/v) where APTES molecules were mainly in the monomeric form, self-assembled submonolayers and/or monolayers were grown on mica. In higher-concentration aqueous solution ($\geq$ 0.25% v/v), APTES molecules exist mainly in the form of

low-molecular-weight oligomers and/or oligomer clusters. APTES oligomers and/or oligomer clusters were directly adsorbed on mica, forming irregular discrete islands. These discrete islands gradually coalesced with each other and eventually grew into densely-compacted complete self-assembled multilayers. We have also studied the crystallization behaviors of APTES oligomers under non-equilibrium conditions from thin aqueous solution layers through a similar fast-drying method. It was found that the non-equilibrium pattern formation is sensitive to the driving force and supersaturation. Various crystalline patterns, including zigzag fractal crystals, parallel aggregations and tree-like dendritic aggregations, were obtained under different driving forces and supersaturations. The mechanisms involved in the pattern evolution were discussed based on the crystallization theories of self-epitaxial nucleation (SEN) and diffusion-limited aggregation (DLA).

6.2 Experimental Section

APTES (clear, transparent liquid, >98%) was purchased from Fluka and used as received without further purification. APTES aqueous solutions with concentrations in the range of 0.1-1% v/v (volumetric concentration) were prepared by mixing the pure APTES liquid with Milli-Q water (Millipore, ≥18 MΩ.cm^{-1}). The mica substrates were purchased from Mateck-GmbH. Clean mica surface was prepared by cleavage in the ambient air just prior to each sample preparation.

The macroscopic surface architectures of self-assembled APTES were grown on mica through two different methods as following:

Method I: As schematically illustrated in Figure 6.1B, a solution droplet (~ 20 μL) was pipetted onto the freshly cleaved mica surface and then quickly removed by N_2 flow. Such a process resulted in the formation of a thin solution layer on the mica surface, which was subjected to rapid evaporation in N_2 atmosphere for ~10 sec. After the N_2 flow was stopped, the mica slice was transferred into a desiccator and incubated for 1~3 hrs.

Method II: A solution droplet (~1 μL, 0.1% v/v) was pippeted onto the freshely cleaved mica surface. The solution droplet spread out to form a thin solution layer on the mica surface, which was then subjected to fast evaporation in N_2 atmosphere for 1~3 min (Figure 6.1B).

The non-equilibrium crystalline patterns of APTES oligomers were prepared by a modified Method I, namely **Method III**. As illustrated in Figure 6.1B, a hump was placed at the downstream of N_2 flow to block the solution droplet from leaving the mica surface. As a result, a thin solution layer with uneven thickness was formed on the mica surface. The solution layer was thick at the end close to the hump but thin at the other. The solution layer was dried in N_2 atmosphere for ~5 sec. After the N_2 flow was stopped, the mica slice was transferred into a desiccator and incubated for 1~3 hrs.

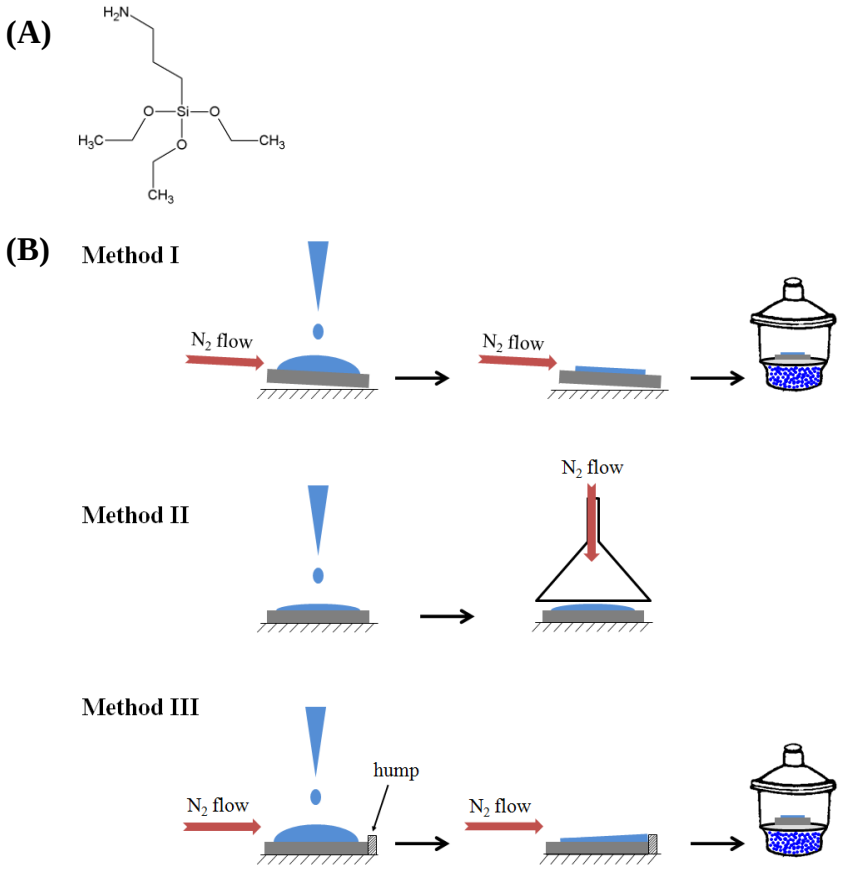

Figure 6.1 (A) Molecular structure of APTES. (B) Experimental setup for self-assembly of APTES (Method I and II) and for non-equilibrium crystallization of APTES oligomers (Method III). For details, see the text.

All experiments were carried out at room temperature (RT). The macroscopic surface architectures of self-assembled APTES were prepared under dry conditions with an ambient humidity of approximate 40%. The non-equilibrium crystallization of APTES oligomers was performed under wet conditions with an ambient humidity of 75~80%. The ambient humidity was controlled with dehumidifiers and recorded with a portable digital hygrothermometer with ± 5% accuracy. The as-prepared structures were characterized using tapping-mode atomic force microscopy (TM-AFM, Nanoscope IIIa, Veeco) operated with "J" scanner and silicon cantilever (force constant: 42 N/m, Nanoworld).

6.3 Results and Discussion

6.3.1 Self-Assembled Molecular Layers Decorated with Macroscopic Concentric Arrays

Figure 6.2 shows typical AFM images of the concentric ring arrays grown from a fast-dried thin solution layer with a concentration of 0.1% v/v. Close-up view (Figure 6.2B) revealed that the concentric arrays consist of many circular, alternate high- and low-coverage regions. The narrow high-coverage regions are covered with polygon networks (Figure 6.2C); whereas the low-coverage regions are wide and covered with irregular discrete clusters (Figure 6.2D). The drying of thin liquid layer on solid surfaces is usually accompanied with the repeating slipping-and-sticking motions of the contact line [18-22]. As schematically illustrated in Figure 6.2E, during evaporation (I→II), the slipping contact line is stuck several times. While the contact line is slipping, it just allows a low surface loading and hence discrete clusters are deposited on the mica surface. In contrast, during the sticking of contact line, a higher surface loading can be achieved within the same time period. The high surface loading in turn leads to the coalescence of the discrete clusters into interconnected polygon networks. The repeating slipping-and-sticking motions of the contact line yield a bundle of alternate high- and low-coverage regions on the mica surface.

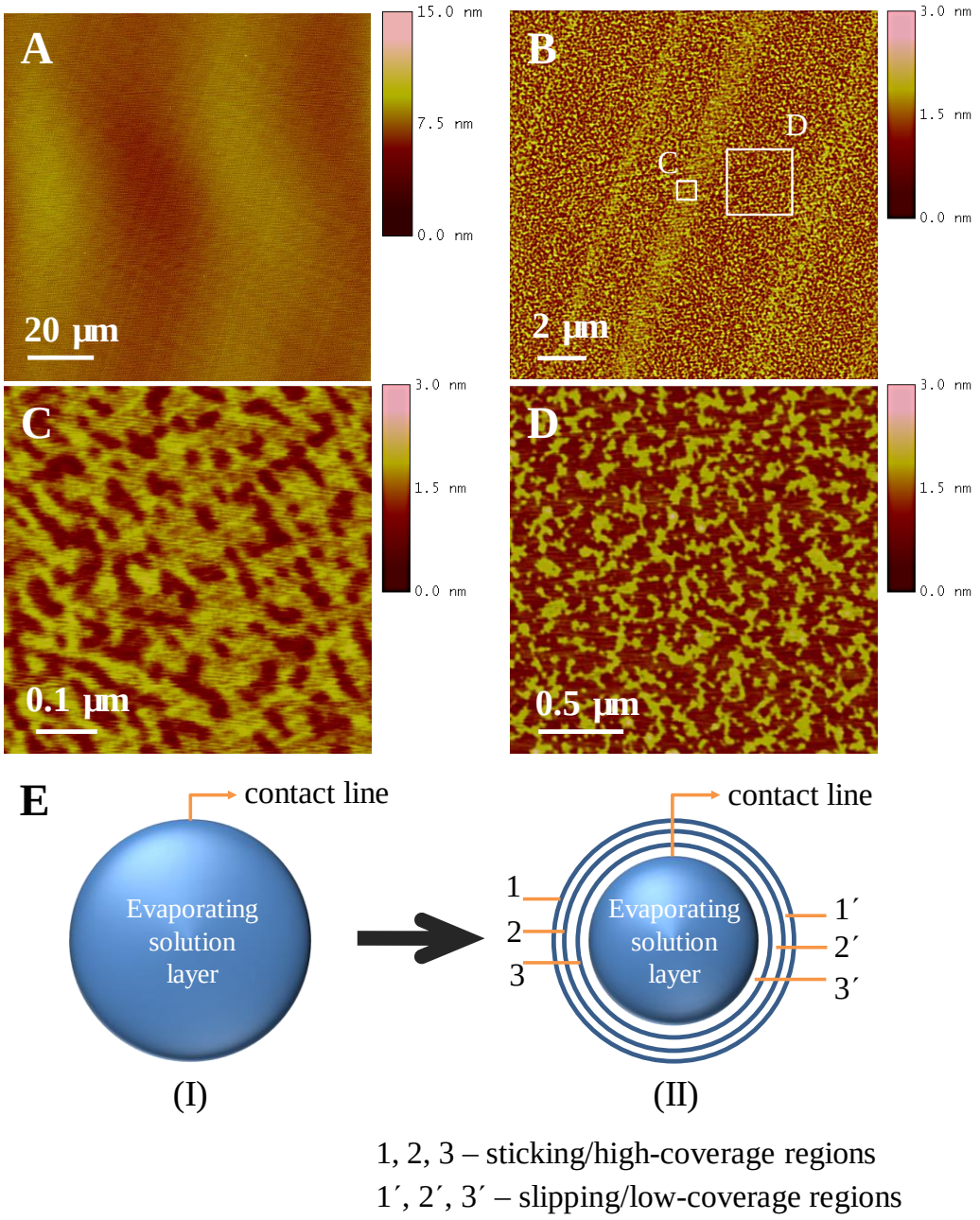

Figure 6.2 (A) APTES self-assembled submonolayers decorated with concentric arrays, grown from a 0.1% v/v thin aqueous solution layer. (B) Close-up view of (A). (C) Polygon networks in the high-coverage regions. (D) Irregular discrete clusters in the low-coverage regions. (E) Mechanism responsible for the formation of concentric arrays. During the evaporation of thin solution layer (I→II), the slipping contact line is stuck several times. Each sticking of the contact line yields one circular high-coverage region. In contrast, each slipping of the contact line generates one low-coverage region. The repeating slipping-and-sticking motions of the contact line leaded to the formation of concentric arrays.

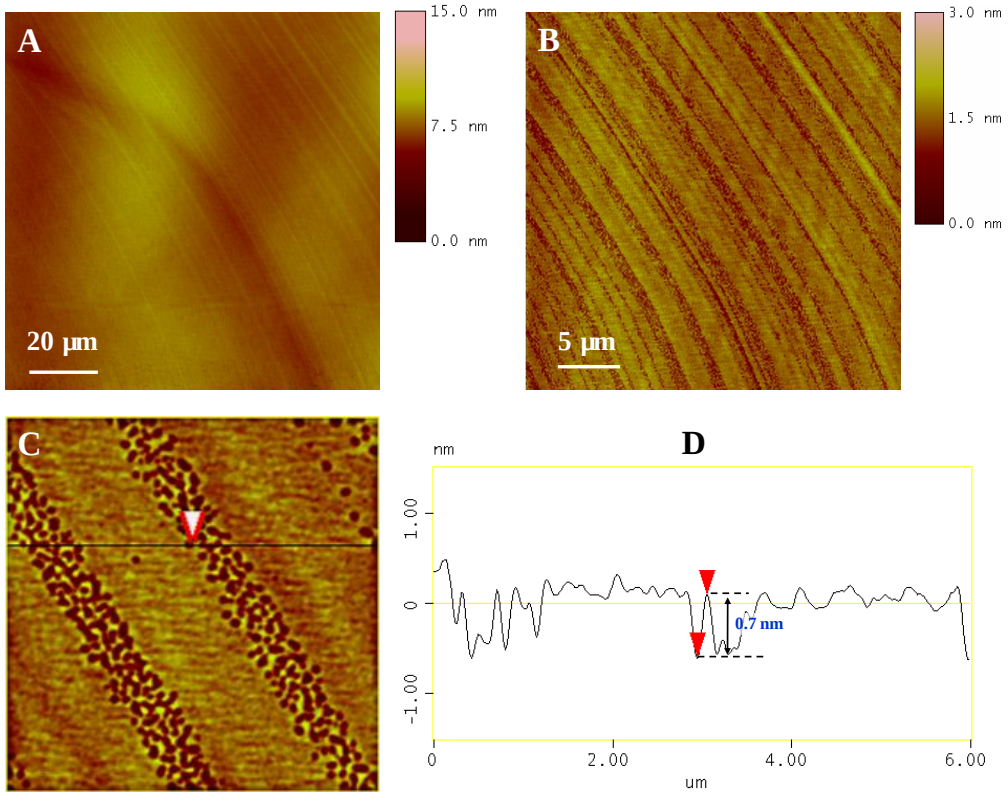

Figure 6.3 APTES SAMs decorated with concentric pinhole arrays, grown from a 0.125% v/v thin aqueous solution layer. (B) Close-up view of (A). (C) Close-up view of (B), and (D) cross section profile of the pinholes.

Figure 6.3 shows the self-assembled APTES structures prepared from a 0.125% v/v thin solution layer. It is clear that similar concentric arrays were established on the mica surface. Close-up view revealed that the concentric arrays are also comprised of many circular, alternate low- and high-coverage regions (Figure 6.3B). In this case, the high-coverage regions are wide and covered with complete self-assembled molecular layers; whereas in the narrow low-coverage regions, there are many regularly oriented pinholes. The pinholes organized into concentric ring arrays and had a mean depth of 0.7 ± 0.2 nm (Figure 6.3C-D). The fully extended APTES molecules are of 10 Å in length [50]. The APTES SAMs were

reported to have an approximate thickness of 5-9 Å [34, 38, 51]. It suggests that the complete self-assembled molecular layers in the high coverage regions are indeed the APTES self-assembled monolayers (SAMs).

At the concentration of 0.25% v/v, diversified self-assembled structures were obtained. As shown in Figure 6.4A, the mica surface was covered with numerous worm-like islands. Underneath the worm-like islands, the first SAM decorated with concentric pinhole arrays is clearly visible. The worm-like islands have a maximum height of approximate 2.4 nm (Figure 6.4B-C), equivalent to 4-5 monolayers. According to the reported monomer-oligomer transition at around 0.15 wt% [41], the APTES oligomers and the oligomer clusters are predictable in this 0.25% v/v aqueous solution. We assume that the multilayered islands are attributed to the direct adsorption of the oligomer clusters on the mica surface [31, 34, 42]. AFM characterization also suggests that in high-coverage region (right-up corner of Figure 6.4A), these discrete islands gradually coalescence with each other and eventually grew into densely-compacted full layers. The cross-section profile of the magnified view (Figure 6.4D-E) enclosed that the full layer has a thickness of 1.3 ± 0.1 nm, corresponding to a molecular bilayer. Figure 6.5 shows a kind of polygon networks grown from the same 0.25% v/v thin solution layer. The polygon networks have a thickness equal to the molecular bilayers (Figure 6.5C). We assume that the polygon network is the intermediate structure between the discrete multilayered islands and the complete bilayers.

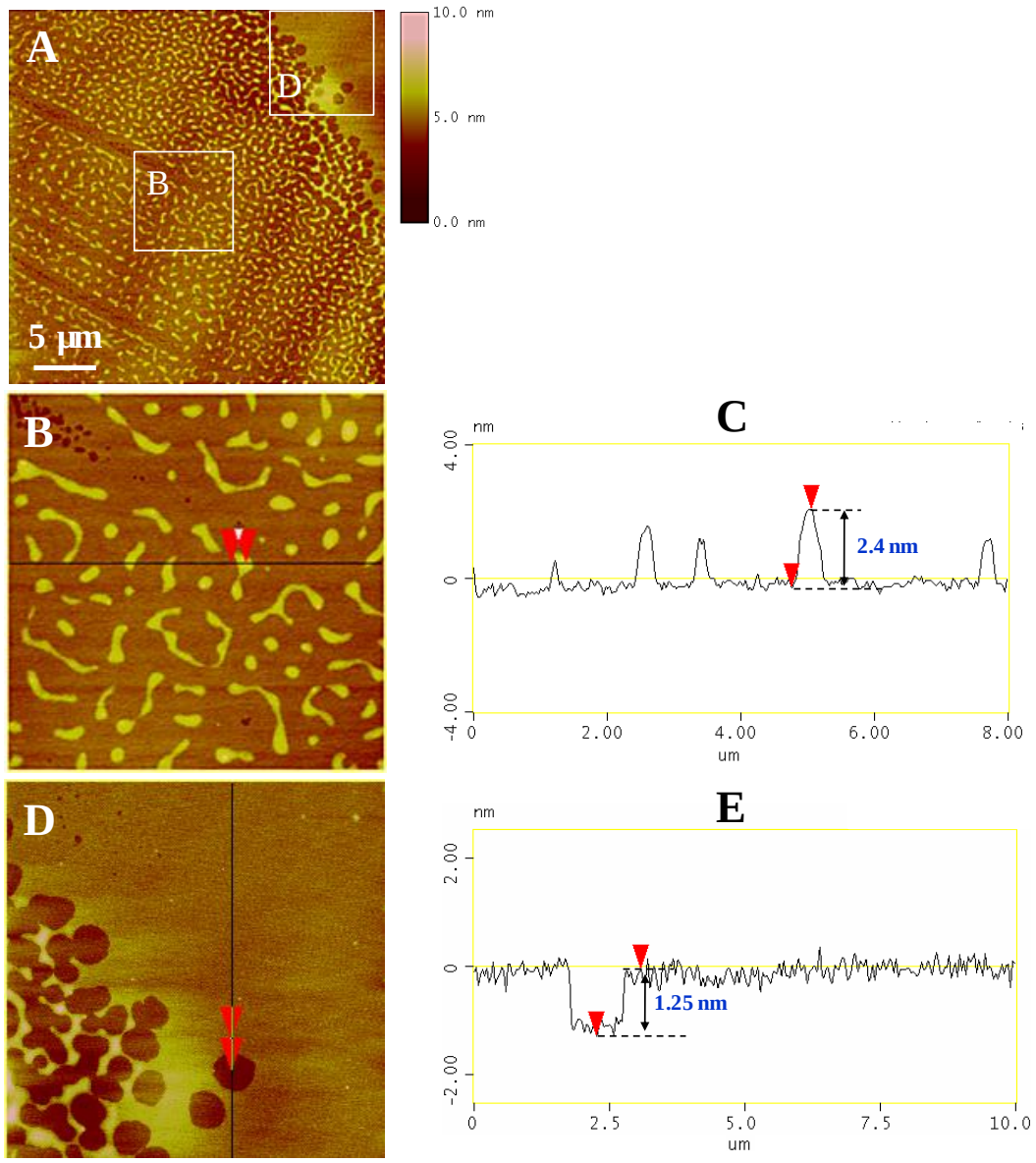

Figure 6.4 (A) Worm-like islands deposited on top of the first SAMs, from a 0.25% v/v thin aqueous solution layer. (B) Close-up view of the discrete worm-like islands at low-coverage region; and (C) cross section profile of the discrete islands. (D) Close-up views of the complete bilayer at high-coverage region; and (E) cross section profile of the complete bilayer.

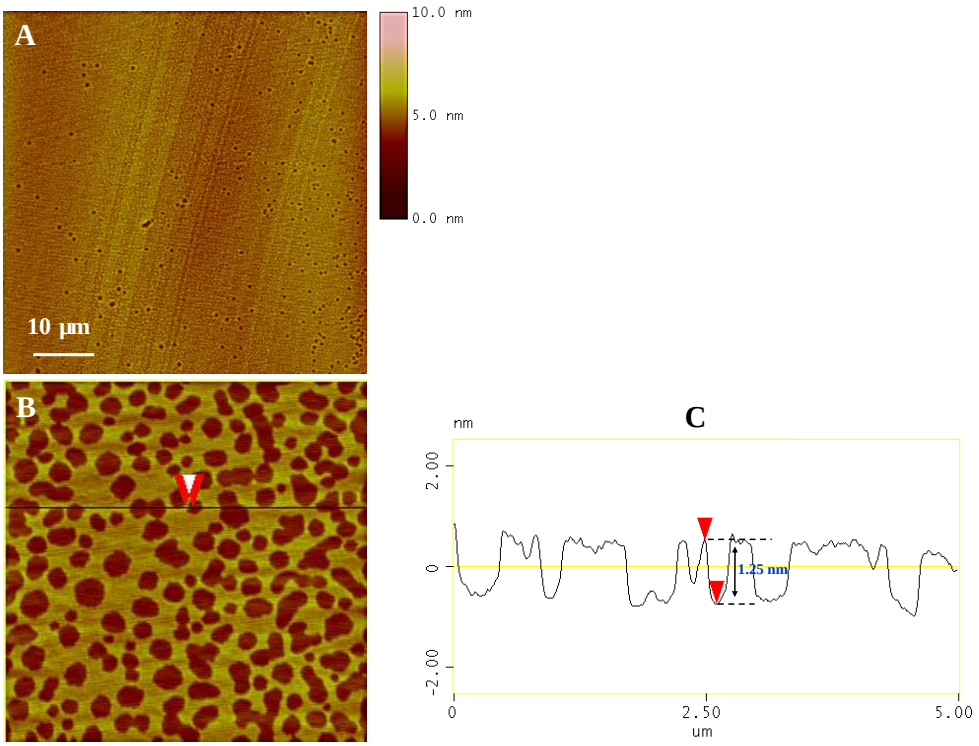

Figure 6.5 APTES bilayered polygon networks, self-assembled from a 0.25% v/v thin aqueous solution layer. (B) Close-up view of (A), and (C) cross section profile of the bilayered polygon networks.

Further increasing the APTES concentration resulted in the formation of smooth self-assembled multilayers with occasional holes, as shown in Figures 6.6-6.7. The thickness of self-assembled multilayers depended on the APTES concentration. The self-assembled multilayer from a 0.5% v/v thin solution layer had an approximate thickness of 5.4 nm (Figure 6.6), corresponding to approximate 10 molecular layers. At the concentration of 0.75% v/v, the thickness was almost doubled to a value of ~9.8 nm (Figure 6.7). APTES molecules exist mainly in the oligomer form in the 0.5% and 0. 75% v/v aqueous solution. The formation of larger-sized oligomer clusters could be greatly enhanced as the concentration increased from 0.5% to 0. 75% v/v. The abruptly increased thickness of the

self-assembled multilayer could possibly be attributed to the direct absorption of larger-sized oligomer clusters on the mica surface.

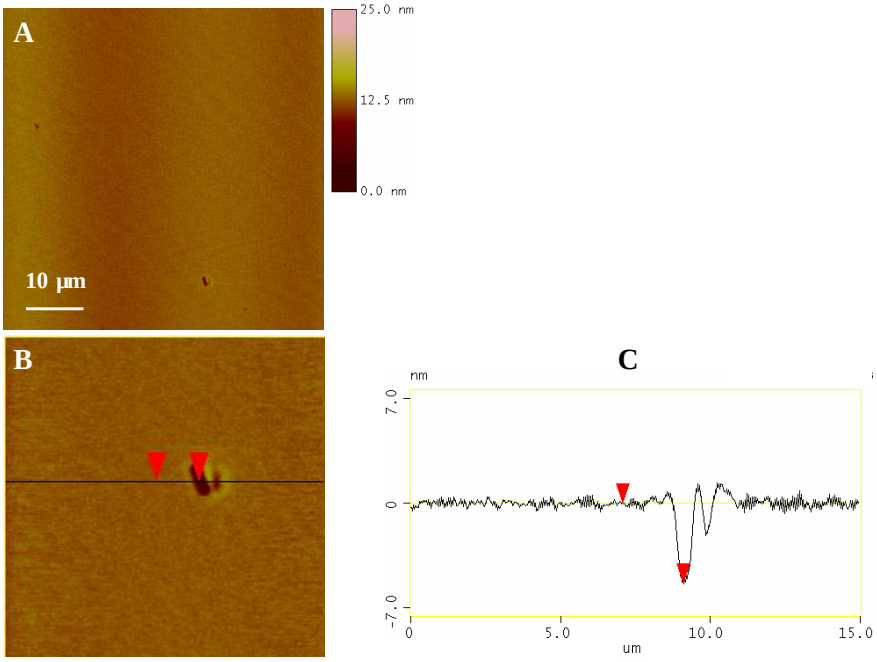

Figure 6.6 APTES self-assembled multilayer, grown from a 0.5% v/v thin aqueous solution layer.

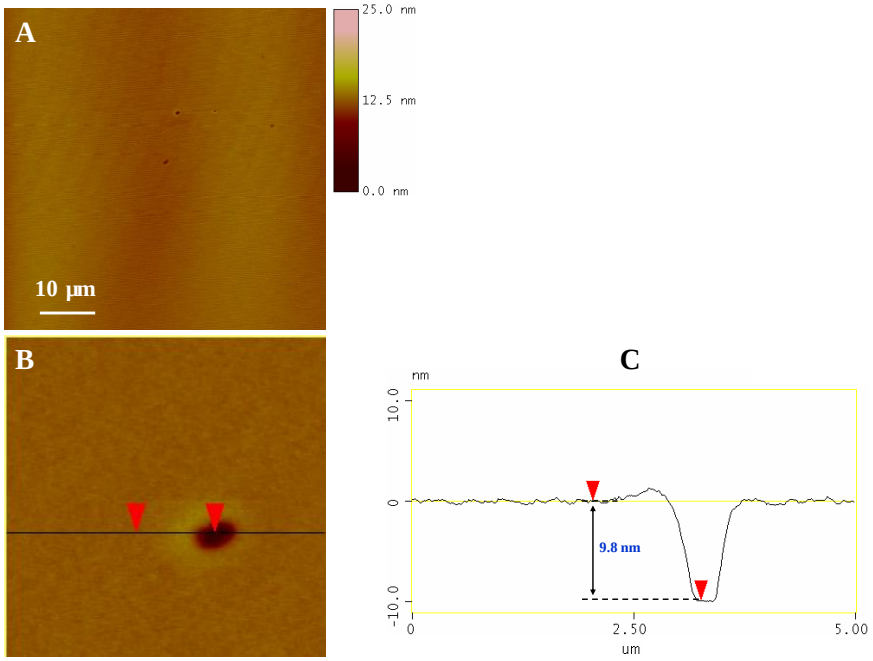

Figure 6.7 APTES self-assembled multilayer, grown from a 0. 75% v/v thin aqueous solution layer.

Note that besides the subtile vibration noise, the thick self-assembled multilayers are perfectly smooth (Figure 6.6-6.7). The characteristic concentric arrays built in the thin self-assembled molecular layers (≤ 3 MLs) disappeared. This could possibly be due to both the high viscosity of the concentrated APTES aqueous solution and the relatively slow evaporation rate in the desiccators. Note that the thin solution layer on the mica surface was dried in two stages. First, it was rapidly dried in N_2 atmosphere. After the N_2 flow was stopped, the remaining solvent was dried slowly in the desiccator. When the evaporating solution layer is highly viscous, the slow drying process in the desiccator may not be strong enough to induce the repeating slipping-and-sticking motions of the contact line and hence smooth self-assembled multilayers were obtained. For comparison, we increased the evaporation rate by adopting Method II. The dilute solution (0.1 % v/v) was employed to make sure a low viscosity of the APTES aqueous solution. As shown in Figure 6.8, macroscopic concentric arrays are clearly visible in the self-assembled multilayers (Figure 6.8). Cross section profile (Figure 6.8 C) shows that the concentric arrays have a mean period of 2.5 μm and amplitude less than 5 nm.

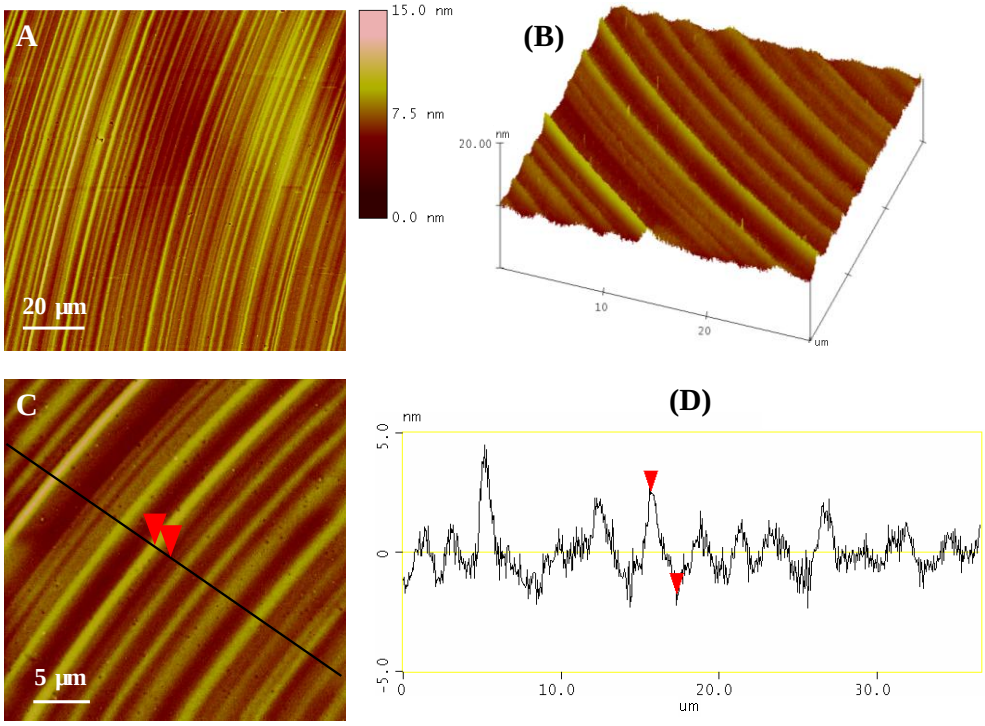

Figure 6.8 (A) Macroscopic concentric arrays built in the APTES self-assembled multilayers, grown from a 0.1% v/v thin aqueous solution layer. (B-C) Close-up views of (A): (B) 3D surface plot view, and (C) 2D top view. (D) Cross section profile of the macroscopic concentric arrays.

6.3.2 Non-equilibrium Crystalline Pattern of APTES Oligomers

Crystallization involves two major steps: primary nucleation and subsequent crystal growth. In general, the phenomena concerned the formation of a ‘new’ phase within a homogeneous ‘old’ phase are characterized by nucleation, such as the emergence of gaseous bubbles, glassy and/or crystalline regimes in a liquid phase (solutions or melts), and the formation of liquid droplets in a vapor phase. Although the studies on crystallization can be traced back to hundreds of years ago, major program on understanding of the non-equilibrium crystallization phenomena was made only in recent 20-30 years [52-58]. In this work, we focused on

discussing the non-equilibrium crystalline patterns of APTES oligomers grown from fast-dried thin aqueous solution layers.

The thin aqueous solution layer prepared by Method III is not evenly distributed in terms of the thickness. The total amount of solute molecules in solution is proportional to the thickness of solution layer. As illustrated in Figure 6.9, the thin aqueous solution layer is roughly divided into three regions. Region I has a lowest amount of solute molecules and supersaturation during crystallization; whereas Region III has the highest ones. Upon drying, different non-equilibrium patterns have been developed in these three regions. Detailed analysis and discussion is given below.

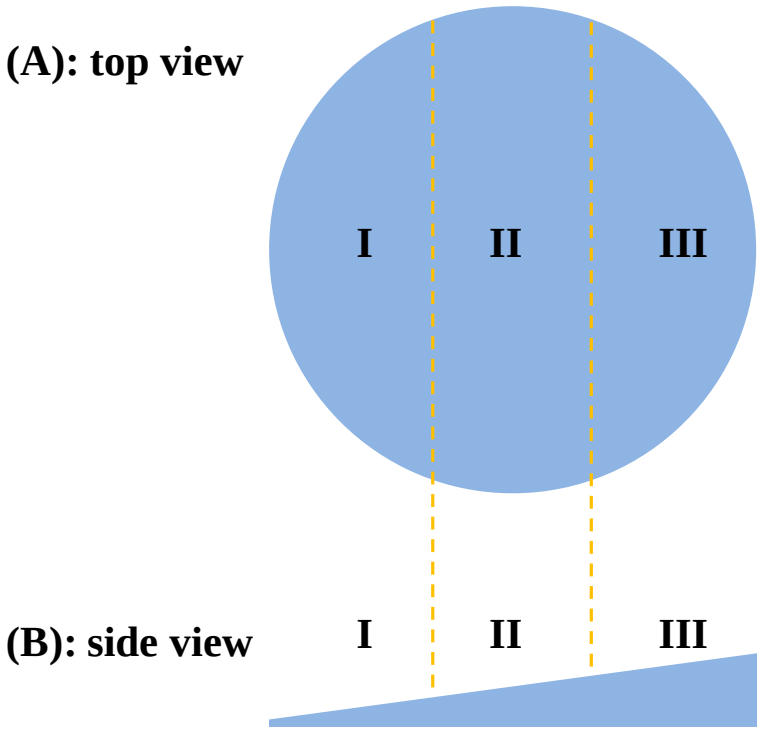

Figure 6.9 Schematic models illustrating the thin aqueous solution layer with uneven thickness, prepared by Method III. (A) top view, and (B) side view. Region I has the lowest amount of solute molecules and supersaturation during crystallization; whereas Region III has the highest ones.

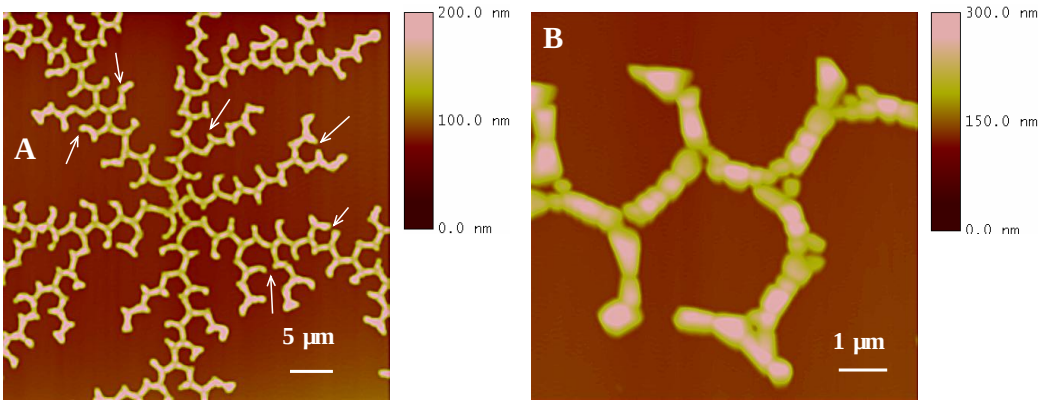

Figure 6.10 Zigzag fractal patterns observed in Region I, grown from a 1% v/v thin aqueous solution layer. (B) Close-up view of (A).

Shown in Figure 6.10 are the zigzag fractal patterns observed in Region I, after a 1 % v/v thin aqueous solution layer was dried at room temperature (RT). The zigzag fractal pattern developed from a central seed and grew outward in a radial fashion. Although the whole zigzag pattern seems to be randomly structured, it exhibits certain periodic symmetry. Each zigzag branch consists of many short "rods" which are almost in the same length and oriented at ~120 º from their neighbors. Close-up view revealed that each short "rod" comprises of 3-6 small crystallites (Figure 6.10B). The short "rods" stop growing or turn ~ 120 ºwhenever two "rods" run close to each other (denoted by the arrows, Figure 6.10A), indicating a possible screening effect during the crystal growth. No closed hexagonal rings are evident in the whole zigzag pattern possibly due to the screening effect.

The zigzag fractal growth is rarely reported in literature. The most investigated example is the zigzag patterns of NH_4Cl aggregated from agarose gel sandwiched

between two glass slides [59-62]. The micro-X-ray diffraction analysis confirmed that the growth of zigzag NH_4Cl aggregates is based on a self-epitaxy mechanism under non-equilibrium condition with low driving force and supersaturation [63]. The other reported zigzag fractal patterns include CsCl [64] and NaCl [65]. Zhao and co-workers [66] proposed that the zigzag fractal patterns are predictable in all the crystal systems with point groups of m3m, 432, m3. Nevertheless, to the best of our knowledge, the reported zigzag fractal crystals seem to be limited within the aforementioned inorganic minerals. APTES is a sort of transparent liquid at RT. One may wonder how a liquid can crystallize into solidified patterns at the same RT. We assume that the crystallization phenomenon could be due to the formation of low-molecular-weight oligomers in the 1% v/v aqueous solution [40, 41]. The basic structural units involved in crystallization could be the APTES oligomers instead of the monomeric APTES molecules. Ishida and co-workers [41] proposed that the APTES oligomers have a six-membered-ring configuration in aqueous solution. Each APTES oligomer may be modeled as a rigid ball. Based on this rigid-ball model, the crystallization behaviors of APTES oligomers are expected to be similar to the cubic crystals. The occasionally appeared cubic islands, as shown in Figure 6.11, further implied the validity of the rigid-ball model. It is known that crystal growth involves two major steps: (1) bulk diffusion: transportation of basic structural units from bulk solution to the growing crystal surfaces; (2) surface kinetics: surface diffusion of the adsorbed structural units and subsequent incorporation of them into the surface lattice. The self-epitaxial nucleation (SEN)

of zigzag fractal patterns requires that the nucleation events take place exclusively at the specific growing crystal surfaces. Any nucleation events beyond the growing crystal surfaces, for example on the mica surface, must be forbidden. To eliminate the nucleation events beyond the growing crystal surfaces, the bulk concentration must be lower than the critical supersaturation. To achieve the SEN, the concentration at the growing crystal surfaces must be higher than the surface supersaturation value. However, the concentration at the growing crystal surface is normally low because the incoming structural units are quickly consumed by the crystal growth. Such a self-epitaxial zigzag growth is only possible when the bulk diffusion is much faster than the surface kinetics. Besides, it becomes possible also because of the following factors: (1) the concentration and supersaturation is much higher at the corners or edges of the growing crystal surfaces [68, 69]; (2) the barrier for the two-dimensional (2D) SEN on the growing crystal surface is low [68].

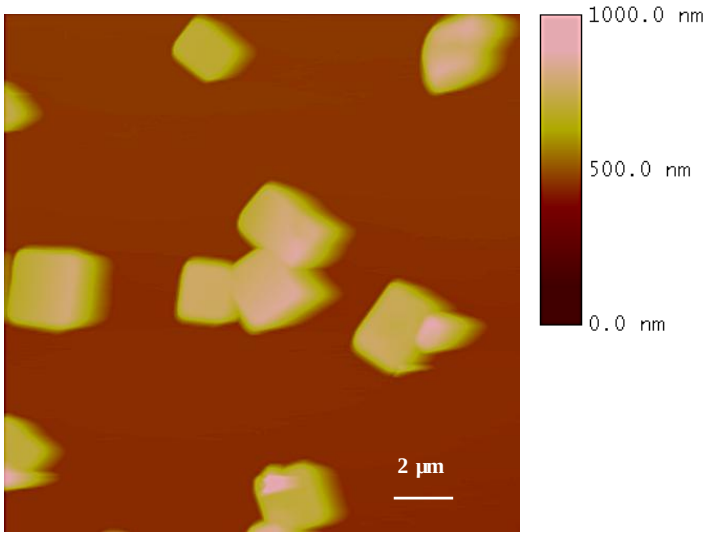

Figure 6.11 Occasionally appeared cubic islands of APTES oligomers.

In region II, two kinds of parallel aggregations are frequently observed. Figure 6.12 shows the cross-shaped 4-arm aggregates together with one or two 6-arm structures. When two or more arms run close to one another, the arms stopped growing or bent accordingly, indicating possible screening effect in the crystal growth. On each arm, there are many epitaxially grown side branches. All the side branches on the same main arm have the same crystallographic orientation and are parallel with each other. Some side branches have their own side branches too. The other similar and coexistent parallel aggregation is shown in Figure 6.13. The main arms in this structure are parallel to each other. On each main arm, there are many epitaxially grown side arms. The screening effect during crystal growth is still obvious in this case (Figure 6.13B). The growth of parallel aggregations suggests a simultaneous occurrence of the self-epitaxial nucleation at the growing crystal surfaces and the parallel heterogeneous nucleation on the mica surface under a medium-high driving force and supersaturation.

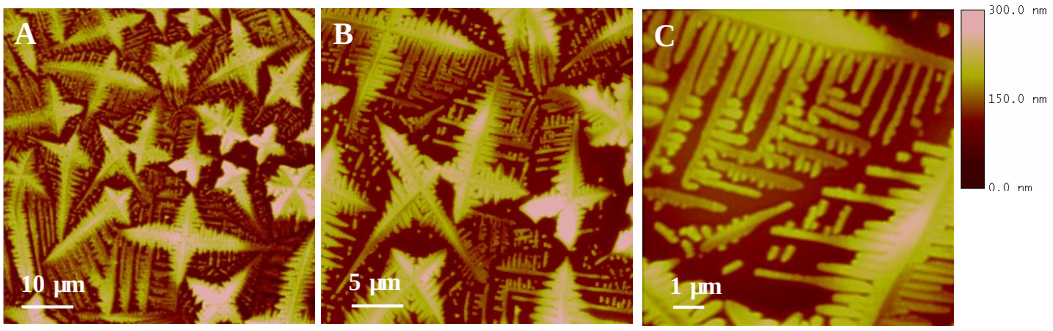

Figure 6.12 Cross-shaped 4-arm parallel aggregates frequently observed in Region II, grown from a 1% v/v thin aqueous solution layer. (B-C) Close-up views of (A).

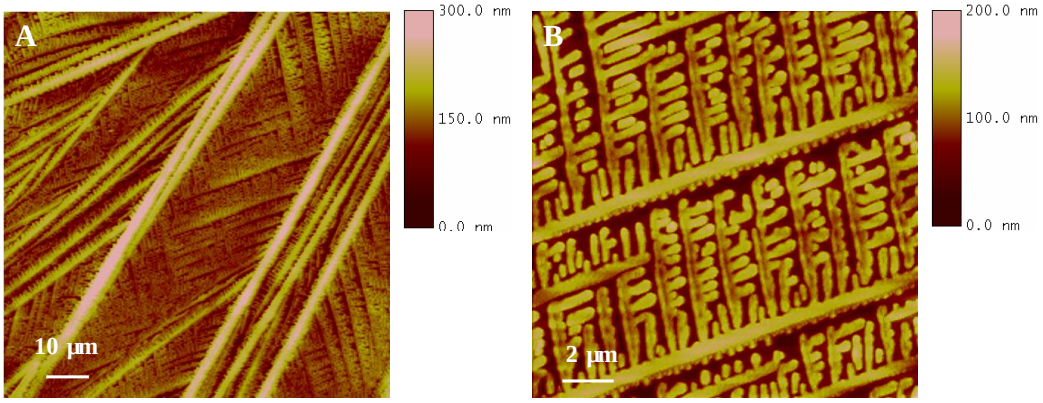

Figure 6.13 Parallel aggregates frequently observed in Region II, grown from a 1% v/v thin aqueous solution layer. (B) Close-up view of (A).

In Region III, the diffusion-limited aggregation (DLA) became evident (Figure 6.14). In the standard DLA model [52], an immobile seed is placed on a lattice. Then a mobile particle is generated at any random position far away from the seed. The particle undergoes a random diffusion due to Brownian motion. When the diffusing particle runs into the immobile seed, it is immobilized instantly and becomes a part of the growing crystal. By repeating this process, a highly dendritic pattern is formed. In our case, close-up view revealed that the dendritic aggregations consist of millions of small particles. According to the DLA model, these small particles serve as the randomly diffusing particles which are successively attached to the growing crystals in a random fashion and thus yield the highly dendritic patterns.

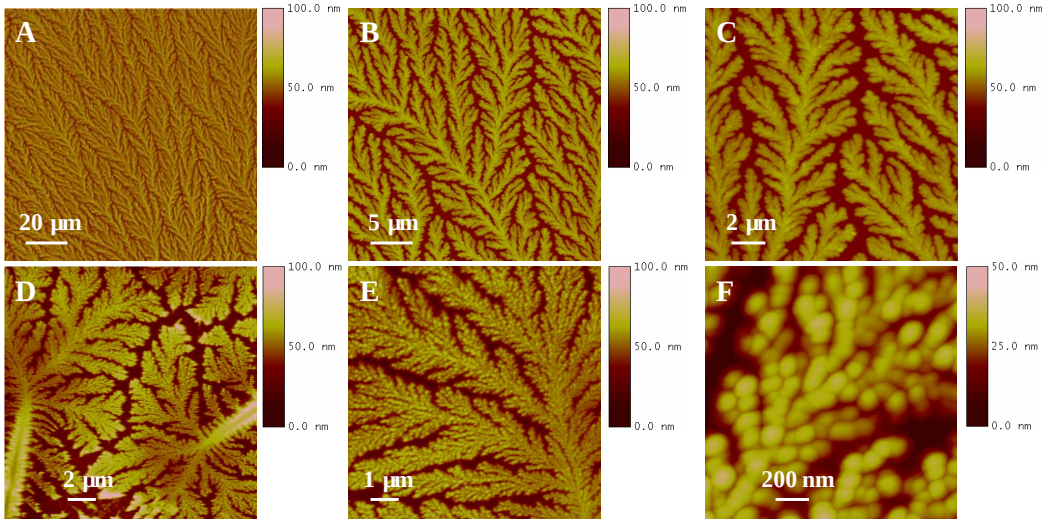

Figure 6.14 Typical dendritic aggregates composed of millions of small particles observed in Region III, grown from a 1% v/v thin aqueous solution layer.

6.4 Conclusions

In conclusion, we presented the self-assembly of APTES on mica from fast-dried thin aqueous thin solution layer. The self-assembled APTES forms macroscopic concentric arrays on mica, attributable to the repeating slipping-and-sticking of the contact line. The growth of APTES self-assembled molecular layers was found to follow a combined “3D islands” and “layer-by-layer” growth mechanism: upon the completion of first monolayer, the further molecular deposition results in the formation of 3D islands. The non-equilibrium crystalline patterns of APTES oligomers change from zigzag fractal, parallel to dendritic aggregates with the increase in driving forces and supersatutions. The growth of zigzag fractal patterns was governed by a self-assembled nucleation (SEN) mechanism. The dendritic aggregates were resulted from a diffusion-limited aggregation (DLA). The parallel aggregates were a consequence of the SEN

together with the parallel heterogeneous nucleation.

References

1. Mooney, J. F.; Hunt, A. J.; McIntosh, J. R.; Liberko, C. A.; Walba, D. M.; Rogers, C. T. *Proc. Natl. Acad. Sci.* **1996**, *93*, 12287.

2. Öner, D.; McCarthy, T. J. *Langmuir* **2000,** *16*, 7777.

3. Xiang, C.; Yang, Y.; Penner, R. M. *Chem. Commun.* **2009**, 859.

4. Demers L. M.; Ginger, D. S.; Park S. -J.; Li, Z.; Chung, S.-W.; Mirkin, C. A. *Science* **2002**, *296*, 1836.

5. Lee, K. -B.; Park, S. -J.; Mirkin, C. A.; Smith, J. C.; Mrksich, M. *Science* **2002**, *295*, 1702.

6. Ginger, D. S.; Zhang, H.; Mirkin, C. A. *Angew. Chem. Int. Ed.* **2004**, *43*, 30.

7. Son, J. Y.; Shin, Y. H.; Ryu, S.; Kim, H.; Jang, H. M. *J. Am. Chem. Soc.* **2009**, *131*, 14676.

8. Xia, Y.; Whitesides, G. M. *Angew. Chem. Int. Ed.* **1998**, *37*, 550.

9. Aizenberg, J.; Black**,** A. J.; Whitesides, G. M. *Nature* **1999**, *398*, 495.

10. Shallcross, R. C.; Chawla, G. S.; Marikkar, F. S.; Tolbert, S.; Pyun, J.; Armstrong, N. R. *ACS NANO* **2009**, *3*, 3629.

11. Feyter, S. D.; Schryver, F. C. *Chem. Soc. Rev.* **2003**, *32*, 139.

12. Lopes, W. A.; Jaeger, H. M. *Nature* **2001**, *414*, 735.

13. Yin, Y.; Lu, Y.; Gates, B.; Xia, Y. *J. Am. Chem. Soc.* **2001**, *123*, 8718.

14. Yang, G.; Woodhouse, K. A.; Yip, C. M. *J. Am. Chem. Soc.* **2002**, *124*, 10648.

15. Arima, V.; Fabiano, E.; Blyth, R. I. R.; Sala, F. D.; Matino, F.; Thompson, J.; Cingolani, R.; Rinaldi, R. *J. Am. Chem. Soc.* **2004**, *126*, 16951.

16. Liu, Y.; Ke, Y.; Yan, H. *J. Am. Chem. Soc.* **2005**, *127*, 17140.

17. Whang, D.; Jin, S.; Wu, Y.; Lieber, C. M. *Nano Lett.* **2003**, *3*, 1255.

18. Karthaus, O.; Gråsjö, L.; Maruyama, N.; Shimomura, M. *Chaos* **1999**, *9*, 308.

19. Yabu, H.; Shimomura, M. *Adv. Func. Mater.* **2005**, *15*, 575.

20. Hong, S. W.; Xu, J.; Xia, J.; Lin, Z.; Qiu, F.; Yang, Y. *Chem. Mater.* **2005**, *17*, 6223.

21. van Hameren, R.; Schön, P.; van Buul, A. M.; Nolte, R. J. M. *Science* **2006**, *314*, 1433.

22. Hong, S. W.; Xu, J.; Lin, Z. *Nano Lett.* **2006**, *6*, 2949.

23. Lehn, J.-M. *Angew. Chem. Int. Ed. Engl.* **1990**, *29*, 1304.

24. Haddon, R. C.; Lamola, A. A. *Proc. Natl. Acad. Sci. USA* **1985**, *82*, 1874.

25. Endo, T.; Kerman, K.; Nagatani, N.; Takamura, Y.; Tamiya, E. *Anal. Chem.* **2005**, *77*, 6976.

26. Perrin, A.; Lanet, V.; Theretz, A. *Langmuir* **1997**, *13*, 2557.

27. Hu, J.; Wang, M.; Weier, H.-U. G.; Frantz, P.; Kolbe, W.; Ogletree, D. F.; Salmeron, M. *Langmuir* **1996,** *12*, 1697.

28. Doh, J.; Irvine, D. J. *Proc. Natl. Acad. Sci.* **2006**, *103*, 5700.

29. Shin, M.; Kwon, C.; Kim, S. -K.; Kim, H. -J.; Roh, Y.; Hong, B.; Park, J. B.; Lee. H. *Nano Lett.* **2006**, *6*, 1334.

30. Heiney, P. A.; Grüneberg, K.; Fang, J.; Dulcey, C.; Shashidhar, R. *Langmuir*

2000, *16,* 2651.

31. Tsukruk, V. V.; Bliznyuk, V. N.; Visser, D.; Campbell, A. L.; Bunning, T. J.; Adams, W. W. *Macromolecules* **1997**, *30,* 6615.

32. Chang, Y.-C.; Frank, C. W. *Langmuir* **1998**, *14*, 326.

33. Zheng, J. W.; Zhu, Z. H.; Chen, H. F.; Liu, Z. F. *Langmuir* **2000**, *16*, 4409.

34. Tsukruk, V. V.; Bliznyuk, V. N. *Langmuir* **1998**, *14*, 446.

35. Pasternack, R. M.; Amy, S. R.; Chabal, Y. J. *Langmuir* **2008,** *24,* 12963.

36. Moon, J. H.; Shin, J. W.; Kim, S. Y.; Park, J. W. *Langmuir* **1996,** *12*, 45621.

37. Chang, Y.-C.; Frank, C. W. *Langmuir* **1996,** *12*, 5824.

38. Kurth, D. G.; Bein, T. *Langmuir* **1995**, *11*, 3061.

39. Etienne, M.; Walcarius, A. *Talanta* **2003**, *59*, 1173.

40. Boerio, F. J.; Armogan, L.; Cheng, S. Y. *J. Colloid Interface Sci.* **1980,** *73***,** 416**.**

41. Ishida, H.**;** Naviroj, S.; Tripathy, S. T.; Fitzgerald, J. J.; Koenig, J. L. *J. Polym. Sci., Polym. Phys. Ed.* **1982,** *20*, 701.

42. Bascom, W. D. *Macromolecules* **1972**, *5*, 792.

43. Haller, I. *J. Am. Chem. Soc.* **1978**, *100*, 8050.

44. Kallury, K. M. R.; Macdonald, P. M.; Thompson, M. *Langmuir* **1994,** *10,* 492.

45. Biebaum, K.; Grunze, M.; Baski, A. A.; Chi, L. F.; Schrepp, W.; Fuchs, H. *Langmuir* **1995**, *11*, 2143.

46. Vallant, T.; Brummer, H.; Mayer, U.; Hoffmann, H.; Leitner, T.; Resch, R.; Friedbacher, G. *J. Phys. Chem. B* **1998**, *102*, 7190.

47. Lvov, Y.; Ariga, K.; Ichinose, I.; Kunitake, T. *J. Am. Chem. Soc.* **1995**, *117*,

6117.

48. Li, H.; Park, S. H.; Reif, J. H.; LaBean, T. H.; Yan, H. *J. Am. Chem. Soc.* **2004**, *126*, 418.

49. Cohen, J. D.; Sadowski, J. P.; Dervan, P. B. *J. Am. Chem. Soc.* **2008**, *130*, 402.

50. Ulman, A. *Introduction to Ultrathin Organic Films: from Langmuir-Blodgett to self-assembly*; Academic Press: San Diego, CA, **1991**.

51. Kurth, D. G.; Bein, T. *Langmuir* **1993**, *9*, 2965.

52. Witten, T. A.; Sander, L. M. *Phys. Rev. Lett.* **1981**, *47*, 1400.

53. Vicsek, T. *Phys. Rev. Lett.* **1984**, *53*, 2281.

54. Banavar, I. R.; Kohmoto, M.; Roberts, I. *Phys. Rev. A* **1986**, *33*, 2065.

55. Liang, S. *Phys. Rev. A* **1986**, *33*, 2663.

56. Meakin, P.; Family, F.; Vicsek, T. *J. Colloid Interface Sci.* **1987**, *117*, 394.

57. Xiao, R. F.; Alexander, J. I. D.; Rosenberger, F. *Phys. Rev. A* **1988**, *38*, 2447.

58. Kaufman, H.; Vespignani, A.; Mandelbrot, B. B.; Wong, L. *Phys. Rev. E* **1995**, *52*, 5602.

59. Wang, M.; Liu, X.-Y.; Strom, C. S. Bennema, P.; van Enckevort, W.; Ming, N. B. *Phys. Rev. Lett.* **1998**, *80*, 3089.

60. Liu, X.-Y.; Strom, C. S. *J. Chem. Phys.* **2000**, *113*, 4408.

61. Liu, X.-Y.; Wang, M.; Li, D. W.; Strom, C. S.; Bennema, P.; Ming, N. B. *J. Cryst. Growth* **2000**, *208*, 687.

62. Liu, X. -Y. *J. Cryst. Growth* **2002**, *237-239*, 106.

63. Li, D. W.; Wang, M.; Liu, P.; Peng, R. W.; Ming, N. B. *J. Phys. Chem. B* **2003**,

107, 96.

64. Pan W.; Mao, Y. W.; Shu, D. J. Ma, G. B.; Wang M.; Peng, R. W.; Hao, X. P.; Ming, N. -B. *J. Cryst. Growth* **2007**, *307*, 171.

65. Zhao, S. R.; Qiu Z. H.; Yang, M. L.; Meng, J.; Fang M. *Phys. A.* **2008**, *387*, 5355.

66. Zhao, S. R.; Wang, Q. Y.; Liu, R.; Lu, L. *J. Appl. Crystallogr.* **2007**, *40*, 277.

67. Chernov, A. A. *Modern Crystallography III–Crystal Growth*, Springer, Berlin, **1984**.

68. Berg, W. F. *Proc. Roy. Soc., A* **1937**, *164*, 79.

Chapter 7

Summary and Future Works

We have developed simple, yet efficient method for fabrication of patterned nanostructures in large scales on various solid surfaces. This method has been applied to the surface patterning of four different materials, ranging from inorganic salts (i.e., NaCl and $Zn(NO_3)_2.6H_2O$) to organic compounds (i.e., organosilane and anthracene). Emphases were focused on the exploration of the mechanisms involved in the surface patterning, including heterogeneous epitaxial crystallization, self-epitaxial nucleation (SEN), diffusion-limited aggregation (DLA), and water-adsorption induced morphology transition, self-assembly, fingering instability, repeating slipping-and-sticking motions of the contact line during irreversible drying of thin solution layer, etc. The patterned nanostructures were characterized in detail using a wide range of analytical techniques. In this chapter, main conclusions drawn out from the results of this thesis were summarized and some of the possible future works are proposed.

7.1 Summary

(I) Oriented NaCl nanocrystals have been epitaxially grown on mica, from thin solution layers under a wide variety of ambient humidity. Although the lattice mismatch between NaCl and mica is as large as -23%, the condition span for the NaCl-on-mica epitaxial growth was founded to be rather wide. At low ambient

humidity (dry conditions), the epitaxial NaCl nanocrystals have well-defined triangle-pyramidal shape. At high ambient humidity (wet conditions), the epitaxial triangular pyramids gradually developed into cubic islands, and eventually into long nanowires with length on the order of millimeters. The morphology transition of the NaCl epitaxial nanocrystals can be attributed to water adsorption at the surface of the growing NaCl nanocrystals. The oriented NaCl nanocrystals can spontaneously organize into highly ordered arrays with exceptionally large spatial scales (up to ~10 mm^2). The self-assembly of the oriented NaCl nanocrystals may possibly be guided by the directional high-concentration zones formed in the evaporating thin solution layers. The NaCl nanocrystal arrays were further employed as templates for patterning thin gold films. The excellent morphology match between the patterned gold films and the original NaCl templates suggests high pattern fidelity, making it comparable to the photolithographic technique.

(II) We have investigated the one-step synthesis of highly oriented, interconnected $Zn(NO_3)_2.6H_2O$ nanotubes on mica and subsequent solid-phase thermal decomposition into porous ZnO architectures. The $Zn(NO_3)_2.6H_2O$ nanotubes with rectangular cross-section were prepared from a thin solution layer and governed by an epitaxial growth mechanism. These epitaxial nanotubes were oriented in directions at ~60 ° to each other and self-assembled into macroscopic interconnected hexagonal networks. It was found that fast evaporation of the solvent was crucial for the growth of high-quality $Zn(NO_3)_2.6H_2O$ rectangular nanotubes. While the overall geometrical configuration of the network-like

assemblies was largely retained in the thermal decomposition of $Zn(NO_3)_2.6H_2O$ nanotubes, the resulting porosity could be tailored by varying the annealing temperature and time. The photoluminescence (PL) spectra at room temperature (RT) exhibited a strong dependence on the annealing temperatures, implying that various types of defects were evolved in the porous ZnO architectures prepared at different temperatures. The electrical measurements demonstrated that the porous ZnO interconnected networks were electrically interconnected as a single integrated unit and exhibited a symmetric, linear current-voltage (*I*-*V*) characteristic.

(III) Macroscopic concentric ring arrays of radially-oriented anthracene wires have been successfully grown on various solid surfaces on the basis of drying-assisted self-assembly. The formation of concentric ring arrays is possibly due to the repeating slipping-and-sticking motions of the contact line. The growth of one-dimensional (1D) anthracene wires can be attributed to both π-π interaction between anthracene molecules and fingering instability during the irreversible drying of the thin solution layer. The radial orientation of anthracene wires was directly driven by the outward capillary flow evolved in the evaporating thin solution layer. The competition between the capillary flow and the Marangoni convectional flow determines either straight or curved anthracene wires to be grown. A stronger capillary flow over the Marangoni convectional flow would result in the growth of straight anthracene wires; otherwise, curved anthracene wires were yielded. The self-assembled anthracene wire arrays were found to

exhibit intense red, green, and blue fluorescence emissions, suggesting possible applications for OLED development.

(IV) APTES self-assembled molecular layers decorated with macroscopic concentric ring arrays have been grown on mica, from thin aqueous solution layers through a simple fast-drying method. The formation of concentric ring arrays in the self-assembled molecular layers can be attributed to the repeating slipping-and-sticking motions of the contact line under fast-drying conditions. The molecular form of APTES in the aqueous solution was found to be crucial for the self-assembly behaviors of APTES and the structures of self-assembled molecular layers. In dilute solutions where APTES molecules were mainly in the monomeric form, submonolayers and/or monolayers were obtained. In higher concentrated aqueous solution, APTES molecules exist mainly in the form of low-molecular-weight oligomers and/or oligomer clusters. AFM characterizations suggest that APTES oligomers and/or oligomer clusters were directly adsorbed on mica, forming irregular discrete islands. These discrete islands gradually merged with each other, and eventually developed into densely-compacted complete self-assembled multilayers. The higher the APTES concentration was, the larger the initial discrete clusters and hence the thicker the APTES self-assembled multilayers would be. APTES self-assembled multilayers with an approximate thickness up to 10 nm have been successfully achieved through this growth mechanism.

We have also studied the crystallization behaviors of APTES oligomers under non-equilibrium conditions from a thin aqueous solution layer through a similar

fast-drying method. The non-equilibrium pattern formation was found to be sensitive to the experimental conditions. Various crystalline patterns, including zigzag fractal crystals, parallel aggregations and tree-like dendritic aggregations, were obtained under different driving forces and supersaturations. The mechanisms involved in the non-equilibrium pattern formation were discussed based on the crystallization theories of self-epitaxial nucleation (SEN) and diffusion-limited aggregation (DLA).

7.2 Future Works

As shown in Table 7.1, there are 20 members in the alkali halide group. Under ambient conditions, alkali halides present an internal crystalline structure of centered cubic, most of them with the NaCl structure (face centered cubic, FCC) and few (CsCl, CsBr, and CsI) with the CsCl structure [1]. It is known that epitaxial crystallizations are usually confined to systems with definite limits of lattice mismatches between the deposits and the substrates. Table 7.2 lists the NaCl-type alkali halides and their lattice mismatches to mica. The epitaxial growth of alkali halides on mica is appealing since it presents robust lattice mismatches through a choice of different alkali halides. Lamelas *et al.* [2] reported that a larger lattice mismatch between alkali halide and mica leaded to a lower nucleation density and a narrower condition span for the epitaxial growth. It was also reported that a larger lattice mismatch increase the energy barrier for the nucleation [3].

Table 7.1 Alkali halides

		Alkali Metals				
		Lithium	**Sodium**	**Potassium**	**Rubidium**	**Caesium**
Halogens	**Fluorine**	LiF	NaF	KF	RbF	CsF
	Chlorine	LiCl	NaCl	KCl	RbCl	CsCl
	Bromine	LiBr	NaBr	KBr	RbBr	CsBr
	Iodine	LiI	NaI	KI	RbI	CsI

Table 7.2 Lattice mismatches between NaCl-type alkali halides and mica

Alkali Halides	a0 (Å)	Lattic Mismatch to Mica (%)
LiF	4.02	-45
NaF	4.62	-37
LiCl	5.13	-30
KF	5.34	-27
LiBr	5.49	-25
NaCl	5.63	-23
RbF	5.64	-23
NaBr	5.96	-19
LiI	6	-18
CsF	6	-18
KCl	6.28	-14
NaI	6.46	-12
RbCl	6.54	-11
KBr	6.59	-10
RbBr	6.85	-7
CsCl	6.94	-6
KI	7.05	-4
CsBr	7.23	-1
RbI	7.33	0

In the studies of NaCl-on-mica epitaxial growth, it has been shown that the affinity of NaCl to the ambient humidity can exert significant impact on the morphology evolution of the epitaxial NaCl nanocrystals. In general, all the alkali halides exhibit strong affinity to the ambient humidity. To the best of our knowledge, there is no systematic study and comparison of the hygroscopic properties of different alkali halides [4]. The limited information indicates that some lithium salts are extremely hygroscopic [5]. It would be interesting to explore the epitaxial growth of different alkali halides at different experimental conditions. Comparing the crystallization behaviors of alkali halides with greatly dissimilar lattice mismatches to the mica substrate and possible difference in the hygroscopic properties, one can explore the critical factors for the control of crystal morphology and patterning. It may also result in some new and interesting structures.

There are a large number of ionic salts with low thermal decomposition temperatures, such as nitrates, carbonates, phosphates, acetates, etc. Some of these ionic salts are highly soluble in aqueous solution. Therefore, a strategy similar to the growth of oriented $Zn(NO_3)_2.6H_2O$ nanotubes can also be applied to these water-soluble salts. In additions, their thermal decomposition renders a convenient yet promising method to prepare porous metal oxide nanostructures. Our study of the oriented $Zn(NO_3)_2.6H_2O$ nanotubes has shown that the epitaxial growth of the one-diemensional (1D) nanotubes were largely contributed by the orthorhombic crystal structure of $Zn(NO_3)_2.6H_2O$ and the anisotropic lattice mismatches between $Zn(NO_3)_2.6H_2O$ and the mica substrate in two perpendicular directions. Different

ionic salts have different crystal structures with different lattice parameters. It would be particularly interesting to explore the nanostructure growth of other ionic salts and their thermal decomposition into metallic nanostructures.

Our studies indicated that in the growth of macroscopic concentric arrays of anthracene nanowires, the electron rich π-surfaces and rigid linear planar structures of anthracene molecules are particularly important for the molecular stacking with maximum overlap of the π-surfaces. In addition, it is the good solubility of anthracene in most of organic solvents that makes our solution-based crystal growth possible. In past two decades, numerous conjugated organic compounds were designed, synthesized, and charaterized [6-8]. These conjugated organic compounds are promising candidates in a wide range of practical applications, such as dye-sensitized solar cells [9, 10], organic light emitting diodes [11, 12], etc. However, all the organic compounds exhibiting excellent π-electron conjugation may not show good solubility in organic solvents and/or perfectly rigid linear planar molecular structures. In fact, to improve the solubility of the π-conjugated compounds, a widely employed strategy is to introduce soluble and flexible side branches into the molecular structures. Theoretically, these flexible side branches are not favored for ordered molecular stacking. It is highly desirable to carry out more investigations on the solution-based self-assembly of these molecules and to establish some generally applicable self-assembly strategies without strict requirement on the molecular structures.

References

1. Sirdeshmukh, D. B.; Sirdeshmukh, L.; Subhadra, K. G., *Alkali Halides: A Handbook of Physical Properties*; Springer-Verlag: Berlin, **2001**.

2. Meyer, Y. H.; Astier, R.; Leclercq, J. M. *J. Chem. Phys.* **1972**, *56*, 801.

3. Lamelas, F. J.; Seader, S.; Zunic, M. *Phys. Rev. B* **2003**, *67*, 045414.

4. Newkirk, J. B.; Turnbull, D. *J. Appl. Phys.* **1955**, *26*, 579-583.

5. Hygroscopy is the ability of a substance to attract water molecules from the surrounding environment through either absorption or adsorption.

6. Ulrich Wietelmann, Richard J. Bauer "Lithium and Lithium Compounds" in Ullmann's Encyclopedia of Industrial Chemistry **2005**, Wiley-VCH: Weinheim.

7. Nakazono, K.; Takashima, T.; Arai, T.; Koyama, Y, Takata, T. *Macromol.* **2010**, *43*, 691.

8. Chen, C. H.; Hsieh, C. H.; Dubosc, M.; Cheng, Y. J.; Su, C. S. Macromol. **2010**, *43*, 697. Scherf, U. List, E. J. W. *Adv. Mater.* **2002**, *14*, 477.

9. Chen, T. A.; Wu, X. M.; Rieke, R. D. *J. Am. Chem. Soc.* **1995**, *117*, 233.

10. Sayama, K.; Sugihara, H.; Arakawa, H. *Chem. Mater.* **1998**, *10*, 3825.

11. Nogueira, A. F.; Longo, C.; De Paoli, M. A. *Coordination Chem. Rev.* **2004**, *248*, 1455.

12. Mizoshita, N.; Goto, Y.; Tani, T.; Inagaki, S. *Adv. Mater.* **2009**, *21*, 4798.

13. Wang, L.; Jiang, Y.; Luo, J.; Zhou, Y.; Zhou, J. H.; Wang, J.; Pei, J.; Cao, Y. *Adv. Mater.* **2009**, *47*, 4854.

GROWTH AND PATTERNING OF NANOSTRUCTURES THROUGH IRREVERSIBLE LIQUID DRYING, SELF-ASSEMBLY, AND CRYSTALLIZATION

WU JI HONG 2010